

AD-A258 972



AFIT/DS/ENP/92-3

①

DTIC
ELECTE
JAN 6 1993
S c D

COLLISIONAL DETACHMENT OF ANIONS USING
FOURIER TRANSFORM MASS SPECTROMETRY

DISSERTATION

Kevin B. Riehl
Captain, USAF

AFIT/DS/ENP/92-3

93-00160

Approved for public release; distribution unlimited

93 1 04 029

AFIT/DS/ENP/92-3

COLLISIONAL DETACHMENT OF ANIONS USING
FOURIER TRANSFORM MASS SPECTROMETRY

DISSERTATION

Presented to the Faculty of the School of Engineering
of the Air Force Institute of Technology

Air University

In Partial Fulfillment of the
Requirements for the Degree of
Doctor of Philosophy

Kevin B. Riehl, B.S., M.S.

Captain, USAF

December, 1992

Approved for public release; distribution unlimited

DTIC QUALITY INSPECTED 6

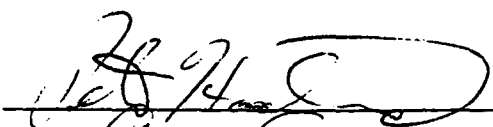
Accession For	
NTIS GRA&I	<input checked="checked" type="checkbox"/>
DTIC TAB	<input type="checkbox"/>
Unannounced	<input type="checkbox"/>
Justification	
By	
Distribution/	
Availability Codes	
Dist	Avail and/or Special
A-1	

COLLISIONAL DETACHMENT OF ANIONS
USING FOURIER TRANSFORM MASS SPECTROMETRY

Kevin B. Riehl, B.S., M.S.

Captain, USAF

Approved:

	7 Dec 92
Alan Carscadden	7 Dec '92
John F. Paulson	7 Dec 92
Ryan Miller	8 Dec 92



Robert A. Calico, Jr

Senior Dean

Acknowledgements

As I complete the most intense and rewarding period of research of my life, I realize my task was made easier by the many individuals who helped me complete this dissertation.

Thanks to the Aerospace Power Division of Wright Laboratory for their sponsorship of this work by permitting me to use their facilities, particularly the Fourier Transform Mass Spectrometer. Personnel who provided advice and timely support included Doug Abner, Bob Knight, Michael Ray and Bill Krein. Thanks also to Alan Garscadden, Peter Bletzinger, Bish Ganguly and Charlie DeJoseph for loans of equipment.

Many AFIT students are afraid to seek advice from other faculty and students. I'm glad I wasn't, and recognize the useful conversations with Capt D. Elsaesser, Dr K. Mathews, Maj D. Beller and Dr W. Bailey. Special recognition goes to classmates Todd Steiner, Dave Elsaesser, Dave Melton and summer hire Lior Pachter for keeping life at AFIT lively and interesting.

It is with some regret that I realize this document is probably the termination of my 'formal' education. As the final opportunity to recognize their efforts, let me applaud the following teachers who played a special role in my education: Mr C. Prudence, Mrs L. Attridge and Mr J. Carey of Livonia Public Schools; Dr J. Bostick and Dr E. Hafen of MIT; Dr W. Bailey and Capt P. Haaland of AFIT.

Of course the ultimate 'teachers' during the course of two years of research were my advisor and committee members. When I formed the committee, my goal was to obtain members who would play an active role and not be 'silent partners'. I was successful, and the input from Capt Byron Welsh (AFIT/ENG) and Dr Alan Garscadden (WL/POOC-3) was invaluable. My advisor, Capt Peter Haaland, is the most dynamic and informed young researcher I've ever met. I feel most fortunate to have linked up with him on a research project. Thanks also to Dr John Paulson (PL/GPID) for his timely support as the Dean's committee representative.

On a lighter note, I acknowledge the indirect support of Ernie Harwell and Paul Carey. It always seemed like my grades rose in the summer, probably because I'd find an excuse to study in the evening so I could tune into the game. If they'd been around in 1992, this dissertation would have been completed faster. I also recognize Mr RT Paullin, my college employer, who taught me that every scientist should also know how to change a trailer hitch ball.

This dissertation is dedicated to the family I love: Dianne, Brian, Jessica, Mom and Dad—their motto of “Do Your Best” was applied throughout—and Dan.

Kevin B. Riehl

Table of Contents

	Page
Acknowledgements	iii
Table of Contents	v
List of Figures	ix
List of Tables	xii
Abstract	xiii
 I. Introduction	 1
Scientific Objectives	1
Why Care About Negative Ions?	2
Experimental Tool	3
Source of Negative Ions	3
Organization	4
 II. Simulating Ion Motion and Induced Currents	 6
Motivation	6
Background	6
Previous Work	6
Summary	9
Simulation Algorithm	9
Equation of Motion	9
Computation of the Electric Field	10
Numerical Integration	12
Algorithm Validation Using Resonant Sinusoidal Excitation	13

	Page
Excitation Amplitude	13
Initial Position	14
New Insight	17
No Absolute Excitation Scale Parameter?	17
Oversampling the Excitation	18
Use of Harmonics to Determine the Ion Radius	19
Effects of Space Charge	22
Trap Potential Well and Ion Evaporation	23
Dangers of SWIFT Excitation	25
Ion Kinetic Energy Distribution	26
Conclusions	34
III. Ion Production from Electron Impact on Trifluoromethyl Iodide	35
Purpose	35
Why Trifluoromethyl Iodide?	35
Background	36
Photon Studies	36
Collisional Studies	39
Summary	44
Experimental Background	44
Ionization Measurements	46
Negative Ion Production Measurements	53
Experimental Details	53
Data Analysis	53
Discussion	55
Electron Impact Detachment	57
Implications of Ion Production Data	60
Summary	60

	Page
IV. Ion Kinetics in Trifluoromethyl Iodide	62
Purpose	62
Previous Work	62
Experimental Details	65
Positive Ion Kinetics	66
Negative Ion Kinetics	76
Conclusions	76
V. Collisional Detachment	79
Overview	79
Experimental Approach	79
Determination of the Collision Rate Constant	81
Elastic Scattering	89
Estimate of Collisional Dephasing	91
Results and Discussion	92
$I^- + Xe$	93
$I^- + Ne$	95
$I^- + CF_3I$	96
Lack of Theoretical Predictions	96
Scaling With Target Size and Polarization	98
Detachment Thresholds	98
Three-body Attachment	98
Conclusions	99
VI. Summary and Implications	100
Appendix A. Experiment Details	103
Reagent Gas Flow	103
Vacuum Pumps	103

	Page
Gas Manifolds	106
Valves	106
Pressure Gauges	108
Trapping Ions	110
Superconducting Solenoid	110
Ion Cell	110
Ion Formation	110
Electron Gun	110
Electron Transport	113
Ion Excitation	115
Function Generator	115
R.F. Amplifiers	117
Digital-to-Analog Convertor	117
Ion Detection	118
Differential Preamplifier	119
Signal Acquisition	120
Computer	122
Bus Communication	122
Data Processing	123
Excitation Waveform Generation	123
Summary	124
Appendix B. Software Algorithms	126
SWIFT Excitation Algorithm	126
Ion Trajectory Simulation	130
Image Current Simulation	136
Bibliography	139
Vita	148

List of Figures

Figure	Page
1. Number of Terms Required to Achieve Electric Field Convergence	11
2. Coupling of the Excitation Field to the Detect Field	12
3. Final Ion Radius vs Excitation Amplitude for Sinusoidal Excitation	14
4. Image Current Intensity vs Excitation Amplitude for Sinusoidal Excitation	15
5. Image Current vs Initial z-Position	16
6. Sinusoids from Different Sampling Rates	19
7. Final Radius vs Oversampling of the Excitation	20
8. Magnitudes of Image Current Spectral Content vs Excitation Amplitude .	21
9. Ion Trajectory Due to Space Charge Prior to RF Excitation	23
10. Ion Evaporation vs Axial Position	25
11. Ion Radius Profile from SWIFT Excitation	27
12. Ion Kinetic Energy vs Excitation Amplitude	28
13. Ion Kinetic Energy vs Initial Position	29
14. Spatial Distribution of Ions along B in a 1 V Trap	30
15. Spatial Distribution Function Orthogonal to B	31
16. Ion Kinetic Energy Distribution Assuming No Thermal Motion	32
17. Ion Kinetic Energy Distribution Quality	33
18. Photoelectron Spectroscopy of CF_3I	37
19. Dissociative Attachment Cross Section for Production of I^- in CF_3I	42
20. Dissociative Attachment Channels in CF_3I	43
21. Ar and CF_3I Peak Intensities vs Electron Energy	47
22. Partial Ionization Cross Sections for $e^- + CF_3I \rightarrow CF_3I^+$ from Different RF Excitations	48
23. Partial Ionization Cross Sections for $e^- + CF_3I$	50
24. Total Ionization Cross Section for $e^- + CF_3I$	51

Figure	Page
25. Ionization Cross Sections for Fragment Ions, Expanded Scale	52
26. Typical Ion Time Domain Signal	53
27. Typical Ion Magnitude Spectrum	54
28. Electron Impact Cross Section for Production of I^- from CF_3I	56
29. Relative Production of I^- in a CF_3I -Ar Gas Mixture	58
30. I^- Peak Magnitude vs Electron Beam Output	59
31. Rate Constants for Ionization and Attachment in CF_3I	61
32. CF_3I Ion Kinetics Using ICR Mass Spectrometry	64
33. Ion Peak Magnitudes vs Delay Time, Experiment (e)	67
34. Normalized Ion Peak Magnitudes vs Delay Time, Experiment (e)	68
35. Ion Peak Magnitudes vs Delay Time	70
36. Histograms of Fitting Parameters from Monte Carlo Runs	71
37. Normalized Abundances vs Delay Time for Experiments (a)-(d)	73
38. Comparison of the Best Fit of System 2 and 3 Applied to Experiment (e) .	74
39. I^- Signal vs Delay Time Showing the Unreactive Negative Ion Kinetics . .	77
40. Typical Time Domain Spectra Showing ICR Signal Decay	83
41. Typical Peak Magnitude from Sliding FFT	84
42. Evolution of Signal Decay With Excitation Amplitude	85
43. Decay Time vs Excitation Amplitude and Ion Kinetic Energy	86
44. Total Collisional Rate Constants	87
45. Average Total Collisional Decay Rate Constants	88
46. Mobility Measurements of Halogen Anions in Argon	90
47. Lower Bound for Collisional Detachment	92
48. Elastic Scattering Efficiency Below the Electron Affinity	93
49. Collisional Detachment Summary for $I^- + Xe$	94
50. Collisional Detachment Summary for $I^- + Ne$	95
51. Collisional Detachment Summary for $I^- + CF_3I$	97

Figure	Page
52. Collisional Detachment Cross Sections Compared to Previous Work	101
53. FTMS Block Diagram	104
54. Vacuum Pump Schematic	105
55. FTMS, Top View	107
56. Pressure Calibration Using the Spinning Rotor Gauge	109
57. FTMS Ion Cell	111
58. Typical Electron Gun Output	112
59. Electron Gun Output Versus Energy	113
60. Schematic of Excitation Electronics	116
61. RF Amplifier Gain Profile	118
62. Detection Electronics Schematic	119
63. Preamplifier Gain Profile	121

List of Tables

Table	Page
1. Theoretical Evidence $V_{pk}T$ is not an Absolute Scale Parameter for Excitation	17
2. Ionization Potentials of CF_3I and Associated Fragments	38
3. Appearance Potentials Associated with CF_3I	38
4. Bond Energies Associated with CF_3I	39
5. Electron Affinities of CF_3I -Related Negative Ions	40
6. Measured Upper Bound of Potential Anions at 15 eV, Referenced to I^- . .	55
7. Ion Molecule Reactions in CF_3I (from Hsieh et al.)	63
8. Ion Molecule Reactions in CF_3I (from Berman et al.)	63
9. Ion Molecule Reactions in CF_3I (from Morris et al.)	65
10. Experimental Parameters for Positive Ion Kinetics Measurements	66
11. Ions Detected in Ion Kinetics Experiments	69
12. Total Decay Rate Constants Determined Using FTMS	72
13. Proposed Kinetic Systems	72
14. Summary of Primary Rate Constants in CF_3I Kinetics	75
15. Summary of Pressures in Detachment Measurements	81
16. Possible Reactions Involving a Negative Ion	89
17. Electron Transport Through Ion Trap	114
18. Hardware and Typical Parameters, Part 1	124
19. Hardware and Typical Parameters, Part 2	125

Abstract

Fourier Transform Mass Spectrometry (FTMS) is used to make energy resolved ion-neutral reaction measurements at translational energies up to several hundred eV. The technique is demonstrated for collisional detachment of anions, and should be easily applied to other inelastic reactions.

Collisional detachment cross sections of iodine anions (I^-) on gas phase targets of neon, xenon, and trifluoromethyl iodide (CF_3I) are measured from 1–300 eV in the laboratory frame. Peak detachment cross sections are roughly 2, 8.5, and 7 Å², respectively. Resolution of the detachment thresholds is complicated by the competition between elastic and inelastic scattering.

Ion kinetic measurements show the iodine anion is unreactive in CF_3I at thermal energies. Positive ion chemistry is consistent with previous results from well established techniques. However, the influence of internal energy is quantified for the first time by varying the electron energy of ion formation. Changes in the observed reactions of I^+ and CF_3I^+ are attributed to ion formation in excited states.

Ionization and attachment cross sections for electron impact on CF_3I are reported for the first time in the energy range of 10–50 eV. The ionization threshold is less than 10.9 eV and the total ionization cross section has a peak magnitude no lower than 4.5 Å². The ion motion in the FTMS ion trap is modelled and the relationship between the ion trajectory and the ion image current is quantified. The ion motion simulations provide insight on FTMS performance.

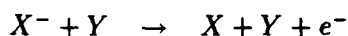
COLLISIONAL DETACHMENT OF ANIONS USING FOURIER TRANSFORM MASS SPECTROMETRY

I. Introduction

Scientific Objectives

The purpose of this research was to examine the dominant inelastic process, collisional detachment, experienced by negative ions with translational energies of a few eV to several hundred eV. The foremost goal was to assess if Fourier Transform Mass Spectrometry (FTMS) could make that class of inelastic measurements.

Detachment is the removal of a single bound electron from a negative ion:



The binding energy of the electron, the electron affinity, ranges from nearly zero to around 5 eV. In contrast, ionization potentials range from less than 10 eV to over 20 eV.

The detachment probability is characterized by a threshold and an energy-dependent magnitude. Previous work (for example, [19, 55, 138]) has reported the onset of detachment at collision energies (center of mass frame) two to three times the electron affinity, a surprising result from a simple thermodynamics point of view. This work sought to resolve threshold energies and measure the detachment magnitude.

FTMS employs a cubic ion trap. Ions are sensed through the fields radiated by their motion in a strong magnetic field. One of the advantages of FTMS—real time monitoring of the negative ion collisional decay—generated several prerequisites to the detachment measurements. Ions are not collected, so it became necessary to model the ion motion in the trap. The objective was to predict the ion trajectories and observed image current for arbitrary experimental conditions. There have been no previous reports on energy-resolved measurements using FTMS. The mathematical description of the ion physics was validated

experimentally by making ionization measurements. Prior to examining the reaction rate at high translational energies, the stability of the anions at thermal temperatures was verified. The ability to form negative ions by electron impact was established.

Why Care About Negative Ions?

Negative ions play roles in a variety of plasma processes. Associative detachment of negative hydrogen may be an important source of interstellar hydrogen gas ($H^- + H \rightarrow H_2 + e^-$) [11]. The opacity of solar optical emission is controlled largely by electromagnetic radiation interacting with negative hydrogen ions in the sun's photosphere [121]. Most of the negative charge in the earth's night-time ionosphere D- and E-layers is carried by negative ions, which are formed via electron attachment after sunset and undergo photodetachment shortly after sunrise. The change in ionospheric conductivity is observed by its effect on radiowave propagation: night-time reception of the AM radio band is generally much better than during the day.

Negative ions also play a role in man-made systems. Tandem Van de Graaf accelerators operate by electrostatically accelerating negative ions up the grid, removing at least two electrons in a stripper and accelerating the new positive ions back down the grid. The final kinetic energy is twice that of a single-stage Van de Graaf. Similarly, neutral particle beams (NPB's) are created from radio frequency (rf) acceleration of negative ions, which are then passed through a stripper to form a neutral beam. Attachment of electrons to form negative ions greatly reduces the plasma conductivity, so plasma switching may be accomplished by adding an attaching medium such as SF_6 . If ions are the primary negative charge carrier (instead of electrons), the change in mobility can create very different electromagnetic propagation characteristics, with implications for communications with, and radar cross sections of, reentry vehicles such as the Space Shuttle or ballistic missiles.

Destruction mechanisms of negative ions have an obvious impact on the performance of the systems cited above. A recent preionization study of a rare gas-halide excimer laser [105] showed that variations in the detachment threshold and magnitude had a dramatic effect on the computed detachment rates. By assuming a factor of two increase in the detachment threshold for F^- (from 3.4 eV to 7.5 eV), the detachment rate decreased by

over five orders of magnitude and resulted in the contradiction of earlier work (which had assumed the detachment threshold was the electron affinity) that claimed collisional detachment played the key role in the preionization of the laser [105].

Experimental Tool

Fourier Transform Mass Spectrometry (FTMS) was first introduced in the mid-1970's [25, 26]. FTMS is a variation on ion cyclotron resonance (ICR) techniques; many refer to it as FT-ICR mass spectrometry. In addition to the technique, the acronym FTMS is interchangeably used here and by other authors to specify the spectrometer itself. Some of the advantages of FTMS include its ion storage capability, tremendous mass resolution (as high as 1 part in 10^8 [87:218A]), a large mass range (programmable; 16–1000 amu, for example), a simple mechanical design [22] and the Fellgett (multichannel) advantage [87:215A]—all ion mass types are measured simultaneously. FTMS systems comprise much less than 1% of all the mass spectrometers in the world, yet they accounted for about 10% of the papers at a recent American Society for Mass Spectrometry conference [136:234]. A variety of reviews on FTMS exist (for example, [15, 22, 42, 68, 69, 87]).

The Advanced Plasma Research Section (WL/POOC-3) of Wright Laboratory's Aerospace Power Division provided use of their upgraded FTMS-1000 mass spectrometer for this research. A detailed description of the upgrade and experimental configuration are in Appendix A.

Source of Negative Ions

Negative ions were produced by electron impact on trifluoromethyl iodide (CF_3I). It has a large dissociative attachment cross section for production of atomic negative iodine ($e^- + CF_3I \rightarrow I^- + CF_3$). The detachment experiments were performed with I^- onto rare gas targets (neon and xenon) and CF_3I .

Organization

This thesis is organized as follows. The detailed description of the experimental apparatus is located in Appendix A. Readers unfamiliar with FTMS may find it useful to read the experimental details before reading Chapters 2–6.

Chapter 2 presents the ion trajectory simulation work. The ion trap is employed as an rf accelerator for the detachment measurements. There is no experimental method available to measure the ion energy directly, so it was essential to model the ion motion in the trap. The ion motion is also the source of the only observable, the induced image current. A three dimensional simulation code was developed which solves the time-dependent boundary value problem and integrates the Lorentz force to determine the trajectory of a test charge. Knowing the trajectory permits computation of the image current. The simulation algorithm is validated through comparison with published results and experiment, and is then used to provide new insight into FTMS performance.

Chapters 3 and 4 link the simulation results in Chapter 2 to the detachment measurements presented in Chapter 5. These two chapters present ionization cross sections and ion kinetics in CF_3I . The results are important both in validating the mathematical formalism of the ion simulation work and in demonstrating that negative ions can be efficiently produced by electron impact. Positive and negative ion production cross sections are quantified for the first time over the energy range 10–50 eV, and the implications of adding CF_3I to a plasma discharge are predicted. A simple model is constructed to describe the cation kinetics and rate constants are quantified. The data should convince the reader that measurements using FTMS and the ion trap physics are well defined.

Chapter 5 presents collisional detachment measurements obtained using FTMS. Experiments with I^- and neon, xenon and CF_3I targets emphasize the important processes of elastic and inelastic collisions in plasma systems, such as an electronegative discharge. By measuring the ion signal decay at high (by FTMS standards) pressures and subtracting the contribution from elastic scattering, the detachment cross section is deduced. Although difficult to quantify because of the overwhelming elastic cross section at low energies, the

data indicates the detachment threshold may be lower than previously thought and may be as low as the electron affinity. Chapter 6 provides a summary and concluding remarks.

II. Simulating Ion Motion and Induced Currents

Motivation

It has been known for over a half century [78] that rf electric fields can be used to accelerate charged particles. FTMS employs this concept to excite ions into cyclotron orbits; the ion cell is essentially a small rf accelerator. Because of the finite geometry of the cube, the effect of the rf field on the ion is spatially dependent. To perform energy resolved detachment measurements, it is critical to be able to predict the ion kinetic energy based on the initial conditions for the ion and the time dependence of the rf excitation.

Ions are not collected in FTMS. The only observable is the ion image current, so the relationship between moving ions and their image current must be quantified to fully understand the nature of ion signals. To model the image current, the ion motion must first be determined. This requires analysis of the detailed relationship between the rf excitation and the ion trajectories.

The goal of this chapter is to predict the ion trajectory and image current from arbitrary initial positions and rf excitations. This goal is first motivated by a review of previous work, which confirms the capability to make such predictions has not been documented. A simulation algorithm is described which computes the electric field precisely at any point in the trap for any arbitrary boundary conditions (trap and excitation) and, assuming collisions and space charge are negligible, uses the field to solve the ion trajectory and predict the image current. The simulation is validated by comparing the trajectories and image current to published results and experimental data, and is then used to provide new insight into a variety of FTMS issues. The ion kinetic energy distribution is constructed and the ion cell is shown to be an efficient charged particle accelerator for energy resolved experiments.

Background

Previous Work. Published descriptions of models of excitation and detection have generally approximated the electric field so that the equations of motion may be solved analytically. The simplest assumption is that the excite plates are infinite and parallel.

Given sinusoidal excitation, the solution of the equation of motion is straightforward [136, 58:231–239] and the ion cyclotron radius has the simple form:

$$r = \frac{2V_{pk} T}{a^2 B} \quad (1)$$

where V_{pk} is the peak amplitude of the sinusoidal excitation, T is the excitation time, a is the trap length and B is the magnetic field strength. Note that the radius is independent of ion mass, a critical advantage to FTMS. The infinite parallel plate model has been applied to examine the effects of space charge [136], image current [23] and non-sinusoidal excitation waveforms [56]. Such models provide qualitative insight, but are quantitatively inaccurate, particularly at large cyclotron radii or away from the trap mid-point where stronger coupling with the trap potential occurs.

To account for the finite geometry of the actual ion trap, a quadrupolar expansion of the electric field is common because analytic solutions are still possible [43, 66, 131]. Field expansions of fourth order [131] and seventh order [116] have also been performed to analyze axial and radial ion motion, although an analytic solution from the approximate field requires an assumed form for the axial and cyclotron motion. In general, some abbreviated form of the electric field is used to permit numerical integration of the equation of motion. The ion motion can then be used to examine issues including phase synchronization of the ion packet [49, 50], excitation of z -oscillation along the magnetic field [130, 131] and comparison of the efficiency of different excitation waveforms [56].

The electric field has been computed to a high degree of accuracy over the entire ion trap in very few papers. Van de Guchte and Van de Hart [130] computed the electric field at 100 mesh points covering the the center 88% of the trap volume and, with the mesh as a “look up” table, used interpolation to compute the ion trajectories. Dunbar [36] used Green’s functions applied to Poisson’s law to compute the charge intensity induced on the detect plates for single and differential detection. Although insightful, his presentation on the ICR signal strength was incomplete, as discussed below. Grosshans and Marshall [43] expanded the potential at the trap mid-plane using a Fourier series in the azimuthal angle. Using power (energy) conservation arguments, the ion radius resulting from sinusoidal

excitation was shown to be well represented by a 5th order polynomial function of the infinite parallel plate radius (Eq (1)). This result showed that Eq (1) overestimates the true radius by 39% and that the radius does not increase linearly with the $V_{pk}T$ product.

The ion image current has rarely been discussed formally, although the physics of induced current from charged particles moving near a conductor has been well known for decades [115, 119]. Comisarow [23] developed a “rotating electric monopole” signal model, which showed the image current is linear in both ion radius and number of ions. For a dominantly capacitive circuit detector (*i.e.*, the preamplifier), the resulting signal voltage has the form [23:4099]:

$$V_s(t) = \frac{Nqr}{aC} \sin(\omega_c t - \frac{\pi}{2}) \quad (2)$$

where V_s is the signal voltage (with respect to preamplifier input impedance ground) from one detect plate, N is the number of ions, r is the ion cyclotron radius, a is the trap dimension, C is the input capacitance of the detector and ω_c is the ion cyclotron frequency. Equation (2) extends the feature of Eq (1): the signal voltage is also mass independent. But because Comisarow assumed infinite parallel detect plates, the rotating electric monopole signal model overestimates the true ion signal by about a factor of two.

Dunbar [36] performed a calculation of the spatial variation in ICR signal intensity by using Green’s function applied to Poisson’s equation to compute the charge induced on the detect plate(s). He created “signal strength” contours as a function of position, which provided very nice qualitative insight into the modulation of the image current caused by magnetron motion. But the image *current* is actually the time derivative of the induced charge, which necessitates inclusion of the ion velocity vector. Dunbar omitted this inclusion and, as a result, did not include the weak coupling associated with image fields in the excitation and trapping direction. Because of the finite trap geometry, an ion travelling parallel to the detect plate will induce an image current (which would not be true for the infinite parallel plate).

Rempel et al. [116] examined the effect of z-axis oscillation on the ion signal. The image field was expanded about the origin into a 7th order polynomial in (x,y,z) . An equation of motion which decoupled the cyclotron and axial motion was assumed and

inserted into the truncated form. This permitted computation of the image current, which was acknowledged to be accurate only in a relative sense. The image current was used to provide the first theoretical prediction of the increase of ion signal associated with ion compression (relaxation) to the center of the trap. Rempel et al. computed that the signal should increase about 34% from when excitation occurs immediately after ion formation to when it occurs after full compression; their experiments with benzene (a relatively unreactive molecule) verified the prediction to within a few percent.

Summary. Previous research on ion trap physics shows a good qualitative understanding of ion motion. However, given an arbitrary excitation waveform (sinusoid, chirp, etc) with N ions at the center of the trap, the ion energy and peak image current magnitude were subject to large uncertainties.

Simulation Algorithm

Equation of Motion. The classical equation of motion for an ion is given by the Lorentz force:

$$\vec{v}' = \frac{q}{m} (\vec{E} + \vec{v} \times \vec{B}) \quad (3)$$

where q is the ion charge, m is the ion mass, v is the ion velocity vector and v' is the ion acceleration. If the form of the vector electromagnetic fields ($\vec{E}(x, y, z, t)$ and $\vec{B}(x, y, z, t)$) are known, it is straightforward to numerically integrate Eq (3) to determine the ion motion. Since the ion trap lies on-axis within a superconducting solenoid, the magnetic field is reasonably taken (see Appendix A) to be homogeneous and constant: $\vec{B}(x, y, z, t) = B_o \hat{z}$. This results in a set of coupled differential equations:

$$\begin{aligned} v'_x &= \omega_c \left(\frac{E_x(x, y, z, t)}{B_o} + v_y \right) \\ v'_y &= \omega_c \left(\frac{E_y(x, y, z, t)}{B_o} - v_x \right) \\ v'_z &= \omega_c \left(\frac{E_z(x, y, z, t)}{B_o} \right) \end{aligned} \quad (4)$$

Computation of the Electric Field. The scalar potential for a cubic geometry is determined by solving the electrostatic boundary value problem using an adaptive multipolar expansion [64:68-71]:

$$\begin{aligned} \Phi(X, Y, Z) = & \sum_{m,n=1}^{\infty} \frac{4 V_T (1 - \cos \beta_m)(1 - \cos \alpha_n)}{m n \pi^2 \sinh \gamma_{mn}} \cos(\beta_m \frac{\Delta a}{a}) \cos(\alpha_n \frac{\Delta a}{a}) \sin(\alpha_n X) \\ & \times (\sin(\beta_m Y) [\sinh(\gamma_{mn} Z) + \sinh(\gamma_{mn}(1 - Z))] + \frac{V(t)}{V_T} \\ & \times \sin(\beta_m Z) [\sinh(\gamma_{mn} Y) - \sinh(\gamma_{mn}(1 - Y))]) \end{aligned} \quad (5)$$

where X, Y, Z are the ion coordinates normalized to the range 0-1 (so the trap center is at (0.5, 0.5, 0.5)), a is the trap length used to normalize the ion position, Δa is the end plate gap, V_T is the trap potential, $V(t)$ is the excitation voltage (which time dependent), $\alpha_n = n\pi$, $\beta_m = m\pi$, and $\gamma_{mn} = \pi\sqrt{m^2 + n^2}$. The electric field is computed through $\vec{E} = -\nabla\Phi$, which results in a lengthy, but straightforward, summation. Inspection of Eq (5) shows there is no contribution to the scalar potential or electric field for m, n even, as anticipated from the symmetry of the cubic geometry. The implications of this symmetry with respect to ion signal harmonics are discussed later.

Generally, previous work severely truncated the summation of Eq (5) by performing a series expansion near the origin and retaining only a few terms. To accurately model the ion motion over the entire trap volume, the proper number of summation terms had to be determined. Tests were performed to determine the effect on ion trajectories of truncation by varying the series termination point of Eq (5). Electric field convergence tolerances of $\frac{\Delta E}{E} = 10^{-3}, 10^{-4}, 10^{-5}$ all produced equivalent (final radii within 0.5% of each other) ion trajectories for a sinusoidal excitation with an amplitude of 7.8 V (V_{pk}) and a duration of 200 μs . Convergence tolerances of $\frac{\Delta E}{E} = 10^{-2}$ and greater began to show percentage deviations. Since the ion trap dimensions are known only to two or three significant figures [73], the $\frac{\Delta E}{E} = 10^{-4}$ convergence tolerance was selected as the best combination of computational speed and accuracy. Using the 10^{-4} convergence criteria, the number of summation terms required was mapped as a function of (X, Y, Z) . Figure 1 shows the number of terms versus X and Y at the trap mid-plane (where $E_z = 0$). As one would expect intuitively, many terms are required to achieve accuracy near the plates

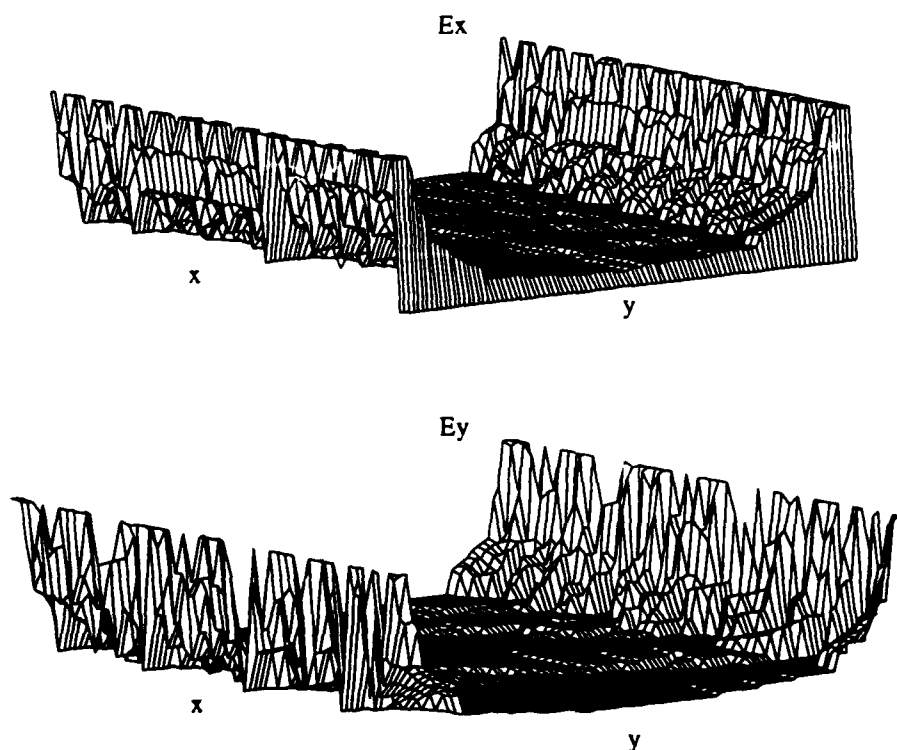


Figure 1. Number of Terms Required to Achieve Electric Field Convergence. The number of summation terms needed to achieve a 10^{-4} convergence tolerance, displayed vertically from 0 (the front edge of E_x plot) to 99 terms. The plateau region in the central region of both plots required 5-13 terms. The greatest number of terms are required near the non-zero boundaries at $y = 2.5$ cm and $y = -2.5$ cm (at the excite plates).

with non-zero potential. There is a broad region over the center of the trap where a small number (5-13) of terms are required. The figure was limited to $m = n = 99$ terms. The steep spatial variation near the boundaries forced implementation of an adaptive scheme which varied the number of terms based upon the ion position.

Accurate determination of the electric field components provided insight into the coupling between the excite plates and the trapping and detect plates. For the infinite parallel plate model, the electric field is spatially homogeneous. The finite geometry of the

cubic ion cell results in electric field lines shown in Figure 2, once again shown at the trap mid-plane.

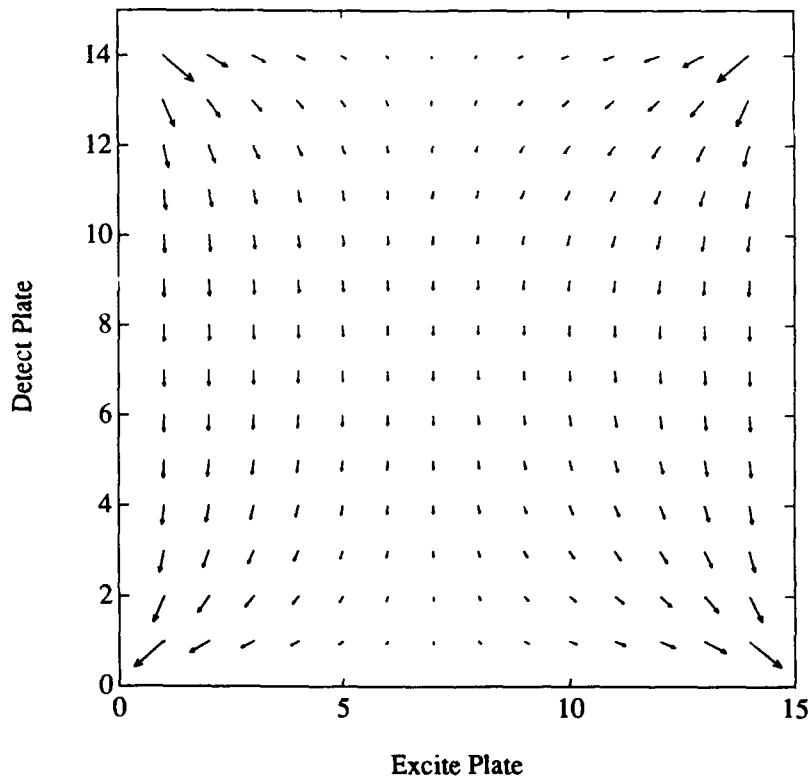


Figure 2. Coupling of the Excitation Field to the Detect Field at the Trap Mid-Plane ($z=0$ cm). The arrows represent the vector field for an instantaneous excitation of 5 V (+5 V on the top plate and -5 V on the bottom plate). The magnetic field vector points out of the page. The central region is fairly homogeneous, similar to that of an infinite parallel plate. The numbers along the axes refer to mesh points; 0 and 15 correspond to the plate locations.

Numerical Integration. With the ability to compute precise values of the electric field for arbitrary plate potentials and ion position, Eq (4) was numerically integrated to determine the trajectory using a Runge-Kutta fourth order algorithm [16:220-227]. The integrator time step was kept as large as possible for computational efficiency, but still

small enough to meet the Courant condition (for example, [113:626-627]) for integrator stability. The time step was generally in the range of 20-100 ns.

The simulation algorithm was developed to apply to any cubic ion trap. Required inputs were the ion mass, charge, initial position and velocity, the magnetic field strength, the trap length and end plate gap, the trap potential, excitation waveform, and the integrator time step. The algorithm computes the ion position, velocity, cyclotron radius (referenced to the initial ion position) and kinetic energy as a function of time.

Using the predicted ion trajectory, the image current [72, 115, 119] induced on the detect plates is computed by a second algorithm. The process is the converse of the excitation; the electric field generated at the plate by the ion is desired, rather than the electric field generated at the ion by the plate. The image current algorithm requires only the ion motion (position and velocity) as a function of time and the ion charge as inputs. It computes the image current generated on each detect plate and the total differential current.

The simulation algorithms were used to probe the characteristics of ion motion, image current and resulting FTMS performance relating to ion initial conditions, space charge and the role of digital versus analog excitation.

Algorithm Validation Using Resonant Sinusoidal Excitation

Sinusoidal excitation is commonly used in FTMS because it provides minimal off-resonant excitation of other mass-type ions. It has been the dominant excitation waveform studied in previous work. Several simulation studies were performed by varying specific FTMS parameters. The effect on the predicted image current was compared to published results and experimental data to validate the simulation algorithms.

Excitation Amplitude. Extant analytic models predict the cyclotron radius will be linearly or nearly linearly proportional to the excitation amplitude. Trajectories of an argon cation (Ar^+) following a resonant 200 μs sinusoidal excitation, with an initial position at the trap center and an initial velocity of zero, are shown in the form of ion radius in Figure 3. Comparison with the predicted radii from Grosshans and Marshall [43]

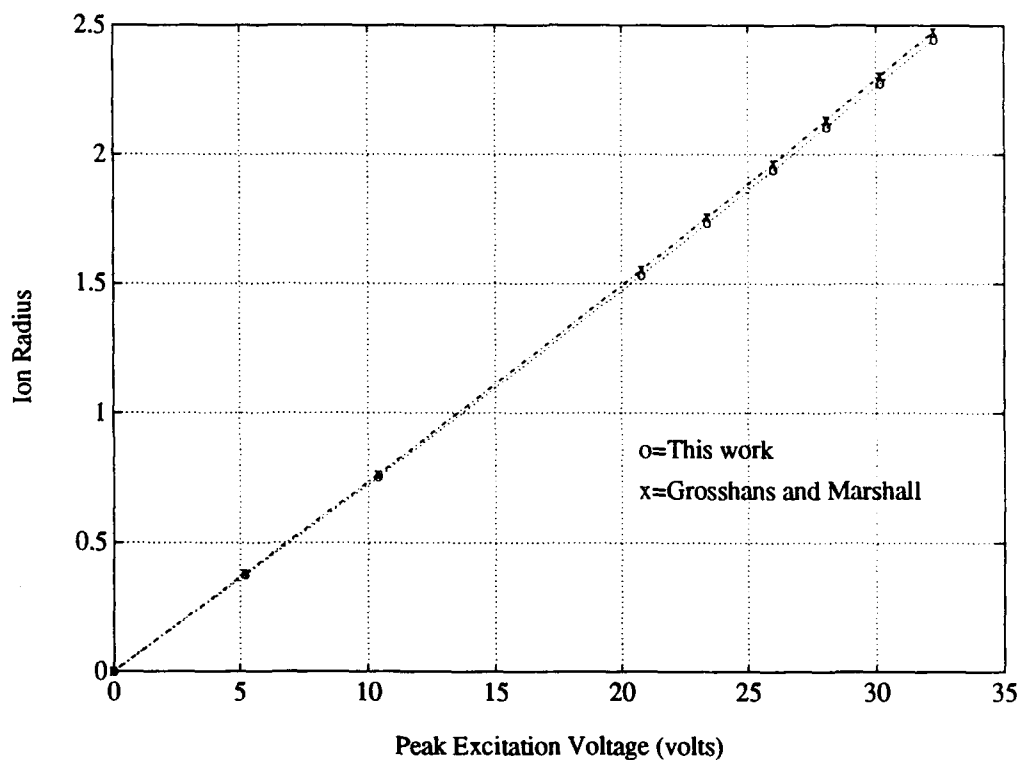


Figure 3. Final Ion Radius vs Excitation Amplitude for Sinusoidal Excitation

is in excellent agreement. Since the image current should be linearly proportional to the radius [23], the peak magnitude is also nearly linear with excitation amplitude.

The linearity of the image current with excitation intensity was confirmed experimentally, as shown in Figure 4. The experiment used argon with a $200 \mu\text{s}$ resonant sinusoidal excitation. The dashed line represents a linear fit to the four lowest excitations; the resulting regression coefficient indicates a probability higher than 0.999 that the data is linearly correlated. The intercept of the fit is zero (as expected) within error bars. At an AFG setting of 200 mV, the ion radius is about 60% of the ejection radius.

Initial Position. As the ion moves away from the trap center, it experiences a different excitation. If its initial position is moved toward the detect or trapping plates, the radial excitation is reduced (the ion “sees” the trap or detect potential more than the

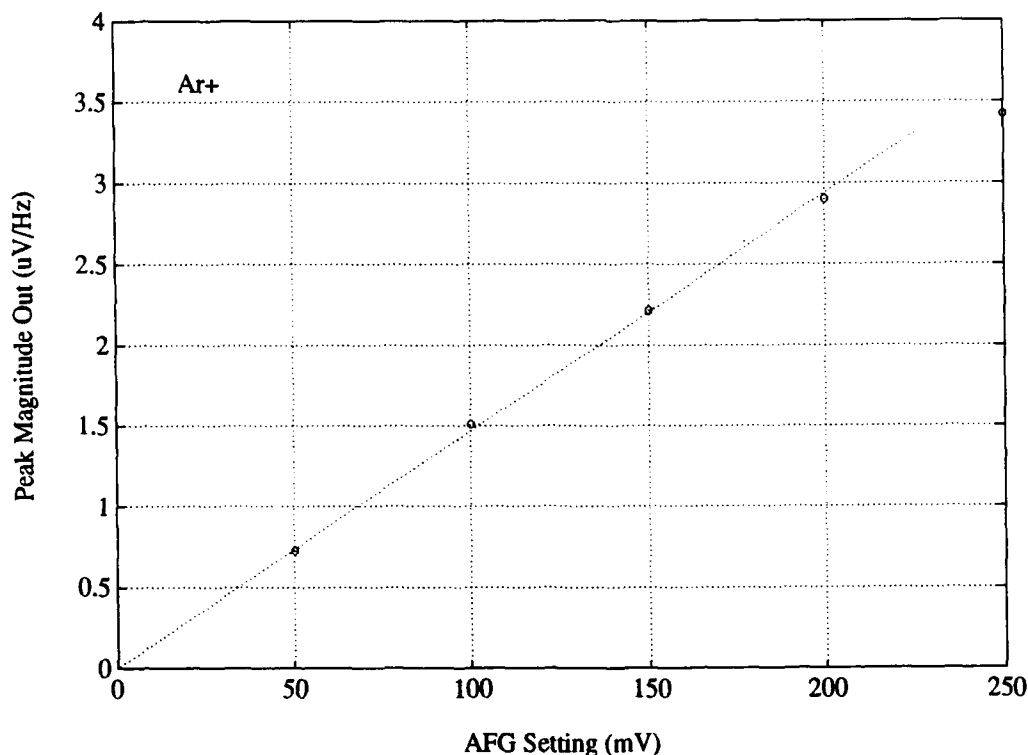


Figure 4. Image Current Intensity vs Excitation Amplitude for Sinusoidal Excitation. Experimental data obtained for Ar^+ from a $200 \mu\text{s}$ resonant excitation.

excite potential). If it moves toward the excite plate, the radial excitation is increased. The final radius is affected, as is the image current.

Since ions are formed with equal probability along the z-axis, but are constrained along x- and y- by the electron beam conductance limit (formed by the front and rear trap as discussed in Appendix A), it would be useful to know the relationship between initial axial position and the image current. A series of simulations were run for which the initial position of x and y were on-axis ($x = y = 0 \text{ cm}$) and the initial velocity was zero. The resonant sinusoidal excitation had a peak amplitude of 7.8 volts for a duration of $200 \mu\text{s}$. The trap potential was -1 volt . The ion was taken to be an iodine anion (I^-), which has a mass of 126.9045 atomic mass units (amu). The ion motion was modelled for 1.1 ms after

excitation termination, which was typical of experimental conditions. The image current was fast-Fourier transformed and the peak magnitude versus z_0 is shown in Figure 5.

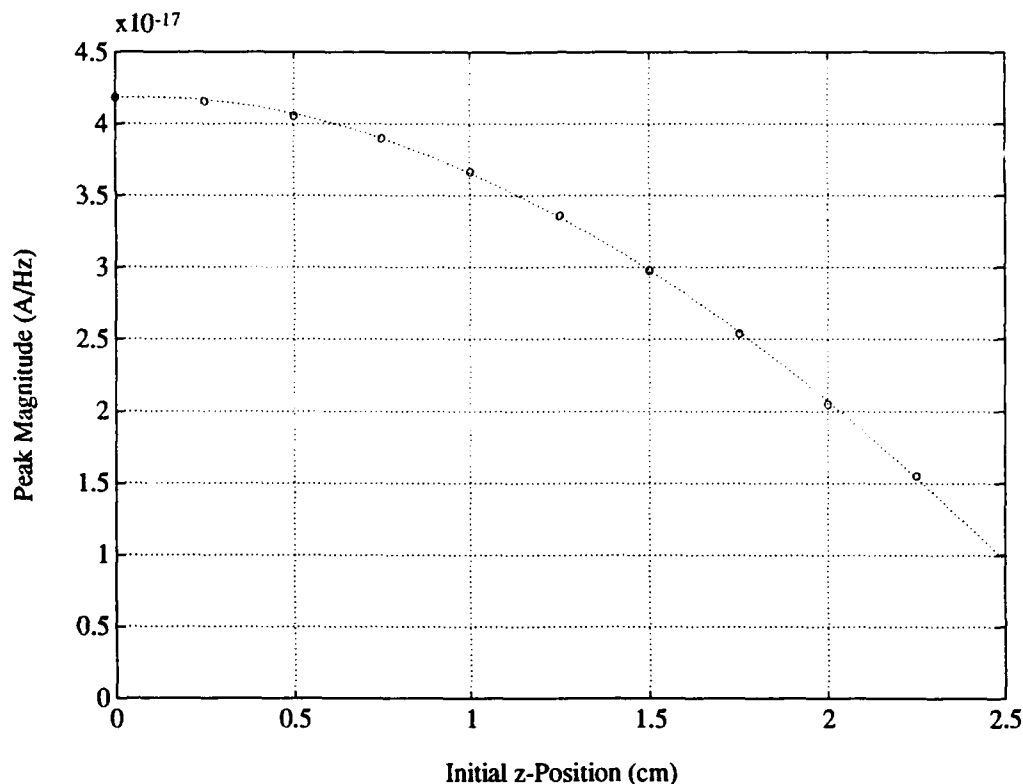


Figure 5. Image Current vs Initial z-Position. The ion has initial conditions of $x = y = 0$ and $v_x = v_y = v_z = 0$. Resonant sinusoidal excitation is employed.

The predicted image current peak magnitude (Figure 5) can be used to model ion relaxation. For N ions distributed equally along the magnetic field (z -axis), the peak magnitude would be $3.11 \times 10^{-17} N$ A/Hz. For a fully relaxed (delta function assumed at $z=0$ cm) ion distribution, the peak magnitude is $4.19 \times 10^{-17} N$ A/Hz. Therefore, the signal grows by 35% through axial relaxation, in excellent agreement with the Rempel et al. prediction of 34%. FTMS experimental data exhibiting relaxation can be seen in Figure 39 (Chapter 4), relating to the negative ion kinetics of I^- .

The effect of ion relaxation on cross section measurements is profound. The magnitude of the image current is seen to vary by up to 35%, yet there are no additional ions

in the trap. Since relaxation is occurring via elastic collisions which thermalize the ion ensemble, the characteristic time for relaxation will vary with reagent gas. It is essential that cross section measurements be performed at the lowest possible pressure (to minimize collisions) and the rf excitation should occur as soon after ion formation as possible.

Figure 5 can also be used to explain why an ion signal persists for excitation amplitudes well past the theoretical ejection point (for example [43]). The average peak magnitude (per ion) for ions distributed furthest from the mid-plane, say in the outer 20%, is about 2.1×10^{-17} A/Hz. The average magnitude for the inner 20% ($-0.5 \leq z \leq 0.5$ cm) is about 4.1×10^{-17} A/Hz, or approximately twice as large as the outer value. Since there is symmetry between the image field and the excitation field, it should take about twice the excitation amplitude to eject the outer ions as it would the inner ions. This is the same figure (a factor of 2) that was required to totally eliminate (complete ejection) the ion signal in the experimental radial ejection study performed by Grosshans and Marshall [43].

New Insight

No Absolute Excitation Scale Parameter? Equation (1) implies the $V_{pk}T$ product is an absolute scale parameter for sinusoidal excitation. That is to say, both the ion radius and image current are linearly proportional to $V_{pk}T$. As shown by Grosshans and Marshall [43] for a real-life geometry, the $V_{pk}T$ product is actually only a scale parameter to 1st order. When the ion is not at the trap midplane ($z=0$ cm), simulation shows that $V_{pk}T$ becomes even less accurate as a scale parameter. Table 1 compares two cases where

Table 1. Theoretical Evidence $V_{pk}T$ is not an Absolute Scale Parameter for Excitation

Initial Position (cm)	Radius (cm)		Difference
	$V_{pk} = 20.8V, T = 100\mu s$	$V_{pk} = 4.16V, T = 500\mu s$	
(0,0,0)	1.56 ± 0.006	1.54 ± 0.003	1.1%
(0,0,2.25)	0.980 ± 0.004	0.914 ± 0.001	7.2%

$V_{pk}T$ is kept constant, but the initial position is varied (the initial velocity is taken to be zero).

The final radii are seen to be different. The effect is accentuated away from the trap center, where the difference is over 7%. The physical reason for the difference is rooted in classical harmonic oscillator theory. The final radius represents the integral of the rf excitation efficiency over the ion path. The ion spends most of its time at the classical turning point in the trapping potential well, where the effect of the excitation is the weakest. Short excitation times permit only a few axial oscillations and will result in the ion spending slightly more time at the center of the trap (and receiving a slightly more effective excitation). Of course, a difference in radius translates to a difference in image current. Caution should be applied before assuming a given $V_{pk}T$ product will produce a given current output.

Oversampling the Excitation. It is well known that to determine the spectral content of a signal, one must sample it at least twice as often as the period of the highest frequency to be measured (the sampling theorem). Because the rf excitation originates with a digital device (the arbitrary function generator, or AFG; see Appendix A for details), it is pointed out the converse does not apply: the excitation must be oversampled by as many as 10–20 times the resonant frequency to achieve the maximum power transfer to the ion. This point is visualized in Figure 6, which shows a resonant rf excitation for iodine (239.64 kHz) with four different digital sampling rates. Clearly, the highest Nyquist frequency for excitation generates the best sinusoid.

A series of simulations were performed which varied only the Nyquist frequency of the excitation (controlled by the clock period set on the AFG). Analog smoothing by the rf amplifiers was taken to be negligible, due to their large bandwidth (see Appendix A). Figure 7 shows the final radius versus the ratio of the excitation Nyquist frequency to the ion cyclotron frequency. Convergence to within error bars doesn't occur until the oversampling rate is approximately 15 to 1.

The implications are important for wideband excitations such as chirp and stored waveform inverse Fourier transform (SWIFT) waveforms. Although SWIFT [88, 137] is designed to apply the same amount of excitation power to a desired mass range, it will not if a portion of the excitation is not oversampled by the excitation hardware. For example,

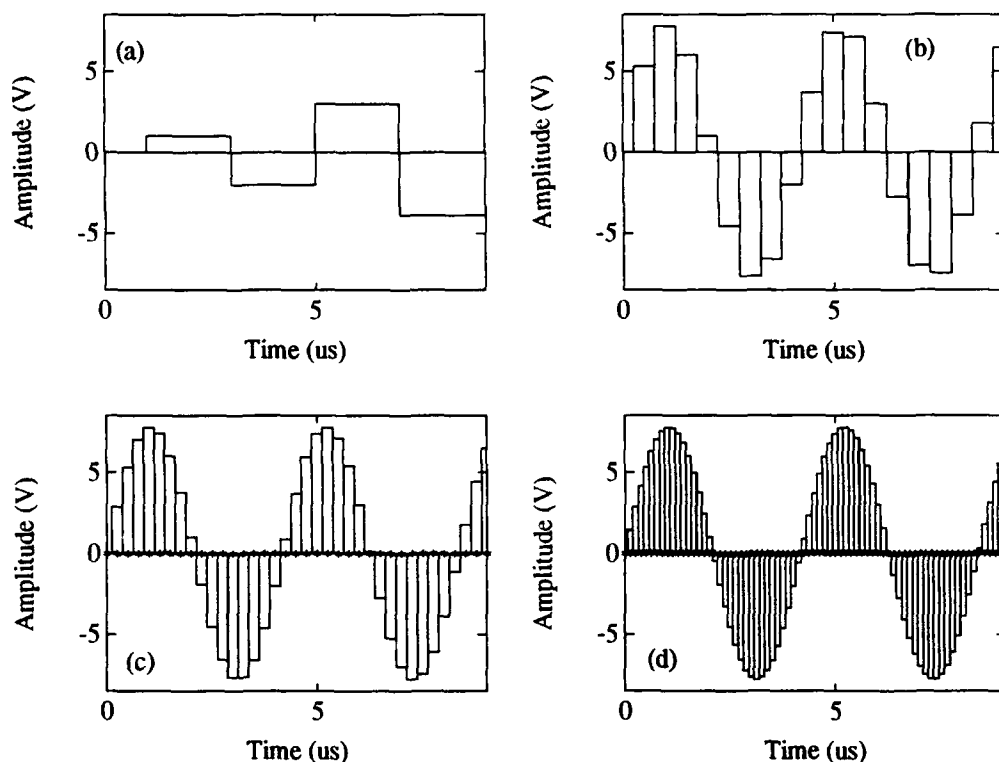


Figure 6. Sinusoids from Different Sampling Rates. A digital rf excitation of 239.64 kHz is output with the following Nyquist frequencies: a) 250 kHz, b) 1 MHz, c) 2 MHz, d) 4 MHz

the Nicolet FTMS-1000 rf amplifiers have a bandwidth of 8 MHz [56:306]. In a magnetic field of 3 tesla, a water cation (H_2O^+) has a cyclotron frequency of about 2.4 MHz. The resulting radius (and image current) will be roughly 10% lower than anticipated by power conservation arguments because the oversampling ratio is only about 3 to 1. For this reason, experiments reported here generally oversampled the excitation in the range of 10–65 times, so as to avoid significant corrections to the observed image current.

Use of Harmonics to Determine the Ion Radius. In the course of examining ion relaxation and compression, Rempel et al. [116] recognized that terms with frequencies of $3\omega_c$ contribute to the image current. It was already well known that harmonics ($2\omega_c$, $3\omega_c$, etc) could be observed experimentally. Grosshans et al. [44] quantified the relationship

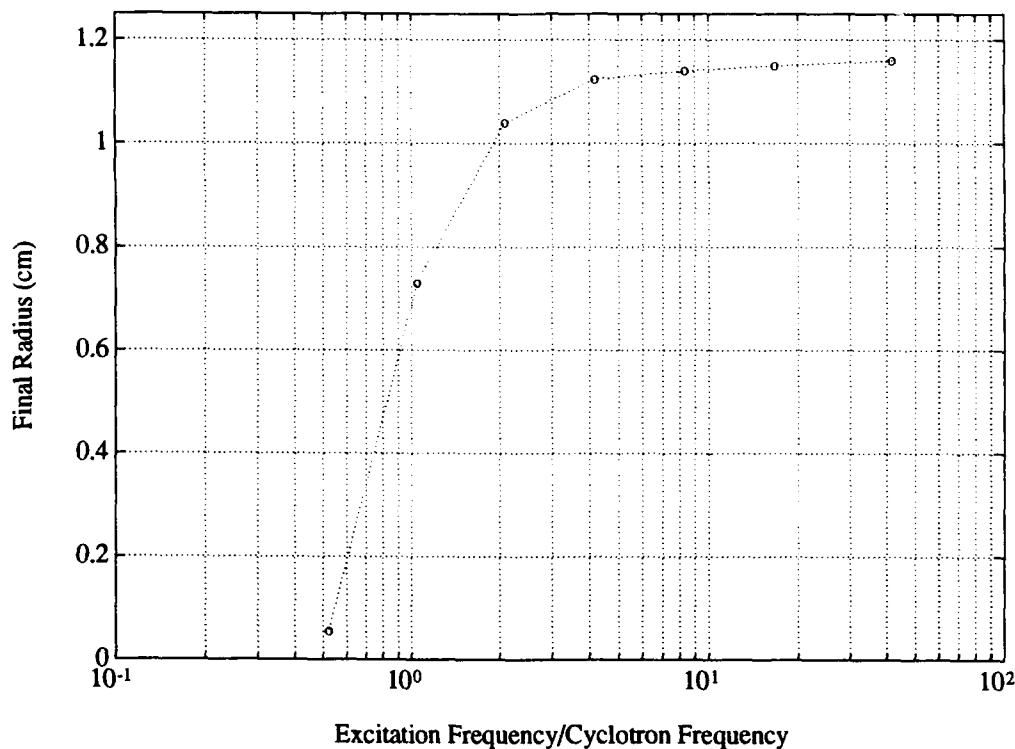


Figure 7. Final Radius vs Oversampling of the RF Excitation. The excitation waveform is a $200 \mu\text{s}$ sinusoid with a peak amplitude of 7.8 V. The Nyquist frequency (f_N) of the excitation is altered by changing the clock period of the AFG; the ratio f_N/f_{ω_c} is the independent variable. The excitation is undersampled for a ratio less than one.

of the third harmonic intensity with ion radius and found that it was roughly parabolic. Since the magnitude of the fundamental frequency is nearly linear with excitation radius (see Figure 3), they proposed that the ion radius could be experimentally determined by taking the observed ratio of the third harmonic to the fundamental. Near ejection, they predicted that ratio would be slightly less than 30%. If true, the technique would be handy for determining the approximate ion radius for arbitrary excitation waveforms.

To investigate the phenomena of harmonics, a series of simulations were run which used sinusoidal excitation with the ion initially at rest at the trap center. The variable was the excitation amplitude. The variation in harmonic magnitude as a function of excitation

amplitude is shown in Figure 8. The results are in qualitative agreement with Grosshans

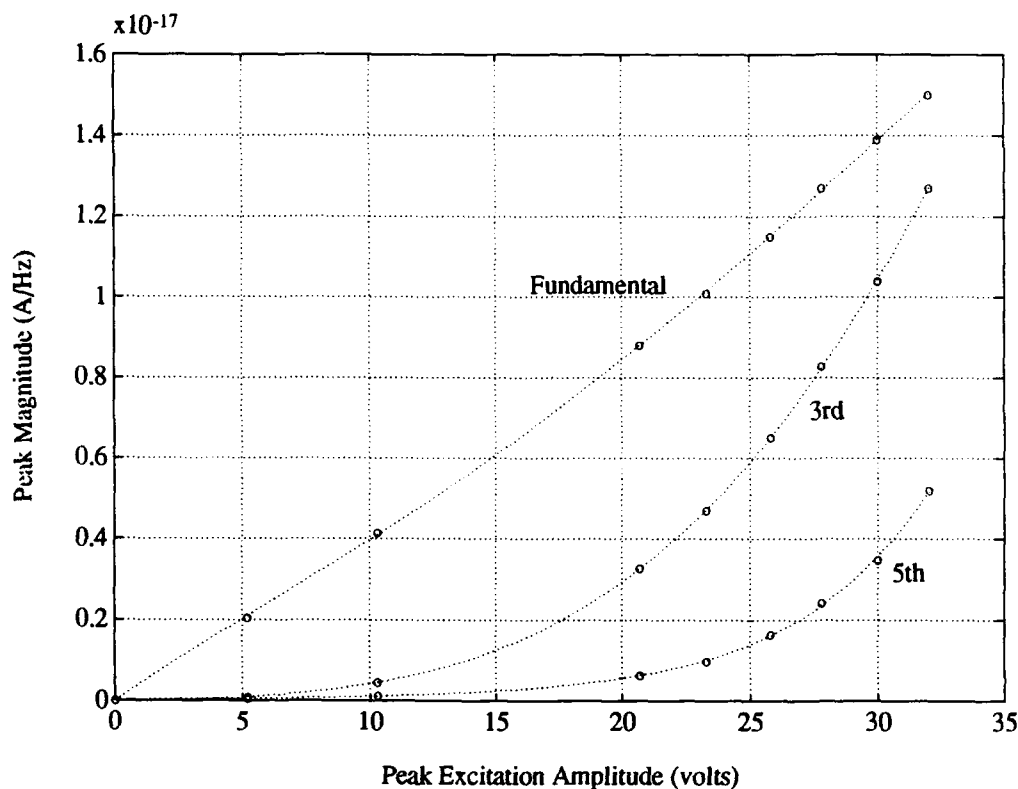


Figure 8. Magnitudes of Image Current Spectral Content vs Excitation Amplitude

et al.; the third harmonic is indeed nearly parabolic. But the predicted fundamental and harmonic magnitudes have a considerably larger ratio, especially near the ejection radius.

Actually, the large disparity is not a surprise. Grosshans et al. [44] used the image current for the third harmonic contribution derived from a seventh order polynomial expansion of the field (from [116]). It has already been shown (see Figure 1) that many more terms are required as the ion approaches ejection. In other words, higher order harmonics are necessary to accurately construct the image field.

There is another subtle point which has been previously overlooked. The cubic trap has always been idealized as a cube in which the sides touch, but are electrically isolated. The actual design has a small gap between the plates (depicted in Figure 57), of order

0.24 cm [73]. Inclusion of this gap shows up in Eq (5) as the two cosine factors which have $\frac{\Delta a}{a}$ in their argument. As $\Delta a \rightarrow 0$, these factors approach unity, the assumption universally applied. As Δa increases, the scalar potential (and electric field) is decreased in accordance with the mode coefficients α_n and β_m . Unless the precise geometry of the ion trap is known, use of harmonics for absolute determination of the ion radius will be system (ion cell) specific and require calibration for high accuracy.

Effects of Space Charge. The simulation algorithm is configured to handle a test charge in the absence of collisions and space charge. One way to examine the effect of space charge prior to excitation is to use the principle of superposition to add the radial field created by an imaginary cylinder of charge distributed along the z-axis to the electrostatic field created by the ion trap. The test charge is placed slightly off-axis in the radial direction so that far-field analysis may be applied. The cylinder of charge is then considered to be a line charge and the radial "space charge" field may be computed. The form of the field is given approximately by

$$E(R) \sim \frac{q N}{4\pi\epsilon_0 L R} \quad (6)$$

where q is the ion charge, N is the number of ions in the trap (in the cylinder), L is the length of the ion cell and R is the radial distance to the test ion. For $N = 10^6$, the space charge field is about $\frac{0.03}{R}$ V/cm, where R is in cm. Ions formed at the edge of the electron beam with 10^6 ions in the trap will experience space charge fields up to several volts per centimeter.

The strong magnetic field prevents radial ejection of the ions. Computed trajectories show that even with 10^7 ions in the trap, ejection from space charge effects was always axial (along the magnetic field). Four cases, with different numbers of ions (N), are shown in Figure 9 in the form of $y(t)$ versus $x(t)$. In each case the ion was initially at rest at the trap mid-plane ($z=0$). Although the ion gains kinetic energy, the magnetic field turns the ion against the static radial field and the ion returns to zero kinetic energy. The data shows that space charge does not cause a significant perturbation to the initial ion position until N approaches 10^6 ions. Ledford et al. [83] have shown experimentally that space charge effects, which cause a shift in the observed resonant frequency, are negligible

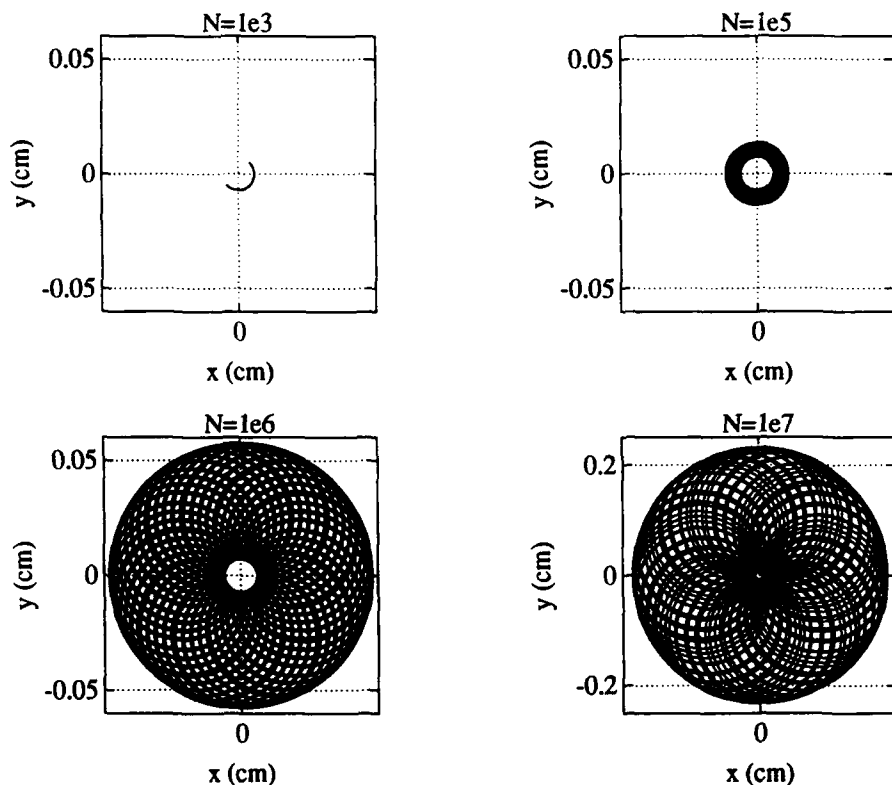


Figure 9. Ion Trajectory Due to Space Charge Prior to RF Excitation. For each plot, the ion initial condition is $x = y = 0.005$ cm, $z = 0$ cm and $v_x = v_y = v_z = 0$. Plot (a), for $N = 1000$ ions, shows only magnetron motion because the radial field is too weak to induce radial excitation. Plot (d), for $N = 10^7$ ions, shows the radial field is strong enough to excite the ion to 10% of the ejection radius.

for $N \leq 5 \times 10^4$ ions. The simulations showed the observed cyclotron frequency decreased significantly with increasing N and also decreased slightly with increasing trap potential. With this in mind, experiments conducted throughout this dissertation were careful to avoid space charge effects by keeping the number of ions below 10^5 .

Trap Potential Well and Ion Evaporation Applying a voltage to the trap plates results in an electrostatic potential well along of the magnetic field. The precise value of the on-axis potential ($x, y = 0$ cm) in the absence of an rf excitation ($V(t) = 0$ V) was computed using Eq (5). The shape of the trapping well is displayed in Figure 14.

The trapping well is parabolic to within 1.5%. Higher order polynomials provided a more accurate representation—a sixth order polynomial was accurate for all values of z to better than 0.1%:

$$\frac{\Phi(0, 0, z)}{V_T} = -2.957 \times 10^{-4} z^6 + 1.040 \times 10^{-3} z^4 + 0.1117 z^2 + 0.3332 \quad (7)$$

where z has units of cm, V_T is the trap plate potential (in volts) and Φ is the trapping potential (in volts) along the magnetic field.

Ions are formed with a distribution of energies. If the magnetic field-aligned velocity is large enough, an ion will overcome the trapping barrier and escape the ion cell axially. This phenomena has been termed 'ion evaporation' [116]. Ions formed by dissociative ionization can have significant kinetic energy; ion evaporation would impose substantial corrections on those cross section measurements due to the attenuated number of ions that remain in the trap.

The probability of ion loss can be quantified as a function of axial position and energy by employing Eq (7). Given a pitch angle γ (the angle between the ion velocity and the magnetic field vectors), the field-aligned energy is related to the kinetic energy (ϵ) by the factor $\cos^2 \gamma$. The criteria for ion loss becomes:

$$\cos \gamma > \sqrt{\frac{|V_T - \Phi(z)|}{\epsilon}} \quad (8)$$

Equation (8) shows mathematically that when the ion's kinetic energy (ϵ) is small enough, the ion cannot escape. Assuming angular isotropy (all angles of γ are equally probable at ion formation), the fraction of ions lost is $(1 - \cos \gamma_{th})$, where γ_{th} is the angular threshold for meeting the criteria in Eq (8). Taking $V_T = 1$ V, the fraction of ions lost as a function of axial position is shown in Figure 10 for several ion energies. The figure shows that ions with low energy ($\epsilon < 0.1$ eV) have a high probability of evaporation only for initial positions very close to the trap plates. Energetic ions (for example, $\epsilon = 4$ eV) have a surprisingly high probability of retention ($> 40\%$) near the center of the trap, although a single elastic scatter will result in a new pitch angle and an increased probability of evaporation. If the

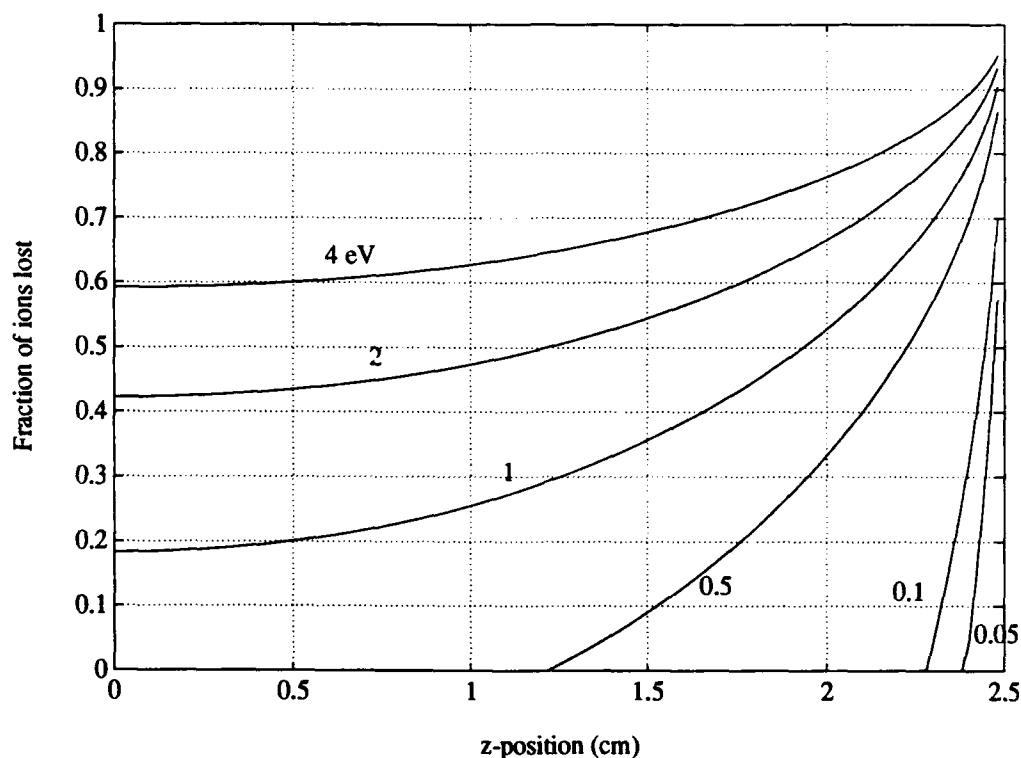


Figure 10. Ion Evaporation vs Axial Position. The fraction of ions lost (1 = 100%) is shown as a function axial position. The ion velocity is assumed to be isotropic. The numerical labels on the parametric curves refer the ion kinetic energy in eV. The trap center is at $z = 0$ cm and one trapping plate is at $z = 2.5$ cm (symmetry about $z = 0$ is assumed)

distribution of ion energies and positions are known, which is rarely true, it is possible to estimate the required corrections to the observed cross sections.

Dangers of SWIFT Excitation. SWIFT is an attractive form of rf excitation because it is designed to excite a user-specified mass range to the same radii [45, 56, 88]. Examination of a SWIFT wideband excitation by simulation verified that a wide range of masses did achieve the same final radii, within error bars.

It is well known that SWIFT excitation can increase the axial ejection rate [130, 131]. The simulations showed two reasons for this effect. The first was the well documented

[130, 131] coupling of the trapping frequency into the excitation frequency which provides an excitation parallel to the magnetic field. Just as the image current has harmonics, fractional harmonics of the excitation field can transfer power to the ion. The second is related to the excitation amplitude. Because SWIFT generally sweeps through a wide range of frequencies in a short period of time (for example, 2 MHz in 800 μ s), the amplitude of the excitation must be increased. Whereas a typical sinusoidal excitation has a peak amplitude of 5-10 volts, a typical SWIFT waveform has a peak amplitude of 50-100 volts. As can be seen at the bottom corners of Figure 2, there are portions of the ion trap where the electric field favors increased axial motion at large radii. A larger excitation amplitude has a larger coupling to the trapping field, so SWIFT causes "on-resonance" axial ejection.

Another drawback to SWIFT is off-resonant radial excitation. As seen in Figure 11, the ion radius vs excitation time has an interesting profile. There is a sharp increase in radius as the resonant frequency is struck. Then there is a period of oscillation (analogous to ringing) which dies out and a stable cyclotron orbit is reached. For this example, the final radius was selected to be about 0.95 cm. Had a large radius been selected, of order 2 cm, the large overshoot near the resonant frequency could have caused radial ejection. Since the ion kinetic measurements (Chapter 4) used SWIFT waveforms, the excitation amplitude was minimized so that the ion radius was always well below ejection. A radius of 0.8-1 cm was the typical goal.

Ion Kinetic Energy Distribution. The primary motivation for constructing the simulation algorithm was to be able to predict an ion's kinetic energy for an arbitrary excitation. FTMS is not configured to collect ions; considering the size of the ion trap it would not be feasible to attempt to place a detector (for example, a surface barrier detector) to calibrate the ion energy; the kinetic energy distribution must be constructed by computer simulation.

The collisional detachment experiments (Chapter 5) used a 200 μ s resonant sinusoid to excite iodine anions (I^-). The sinusoidal output of the rf amplifiers was digitized and stored by a LeCroy 9410 oscilloscope. The recorded waveform became an accurate time-dependent input for the rf excitation within the trajectory computations. Taking

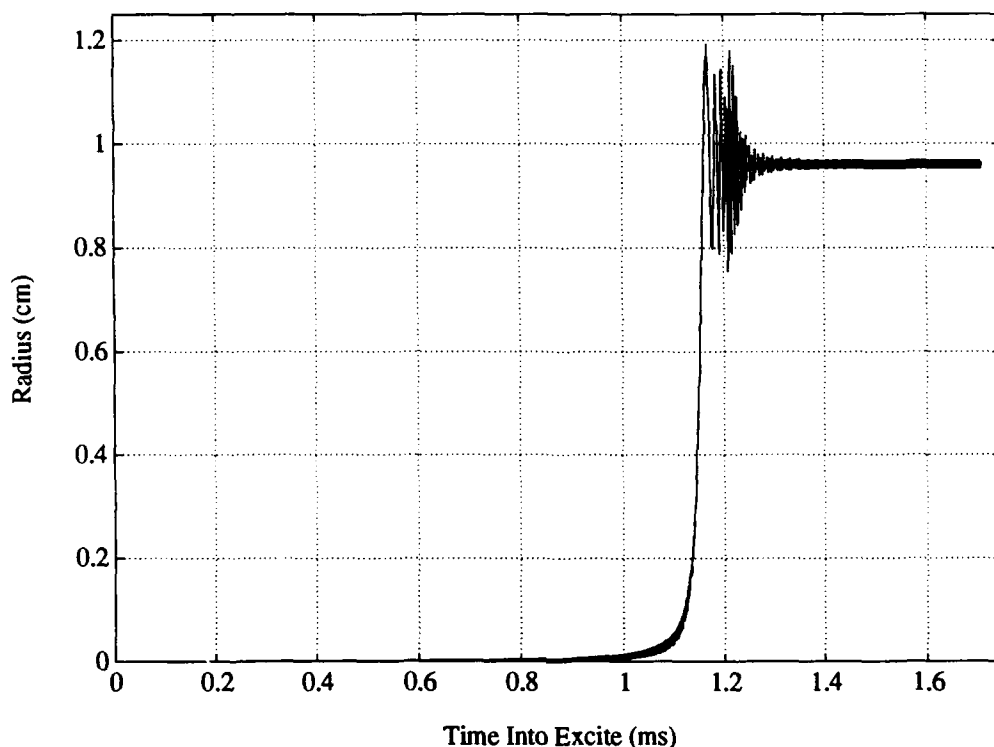


Figure 11. Ion Radius Profile from SWIFT Excitation

the ion initially at rest at the trap center, the excitation amplitude was varied (similar to Figure 3 for argon, Ar^+). The ion kinetic energy was determined as a function of the AFG amplitude, as shown in Figure 12. For I^- , the kinetic energy at radial ejection was computed to be 925 ± 7 eV.

Due to the symmetry of the electron beam and ion trap, and the kinetic energy distribution of the ions after formation, the values shown in Figure 12 will represent the most probable energy of the energy distribution. Ions will actually have an ensemble of initial positions and velocities, with an average position at the center of the trap and an average velocity of zero. As a first pass in constructing the kinetic energy distribution function, a series of simulations were run in which the variable was initial position. The ion temperature was taken to be 0 K (no thermal motion), and the excitation peak amplitude of the sinusoid was fixed at 7.8 volts (an AFG setting of 75 mV) with an excitation time

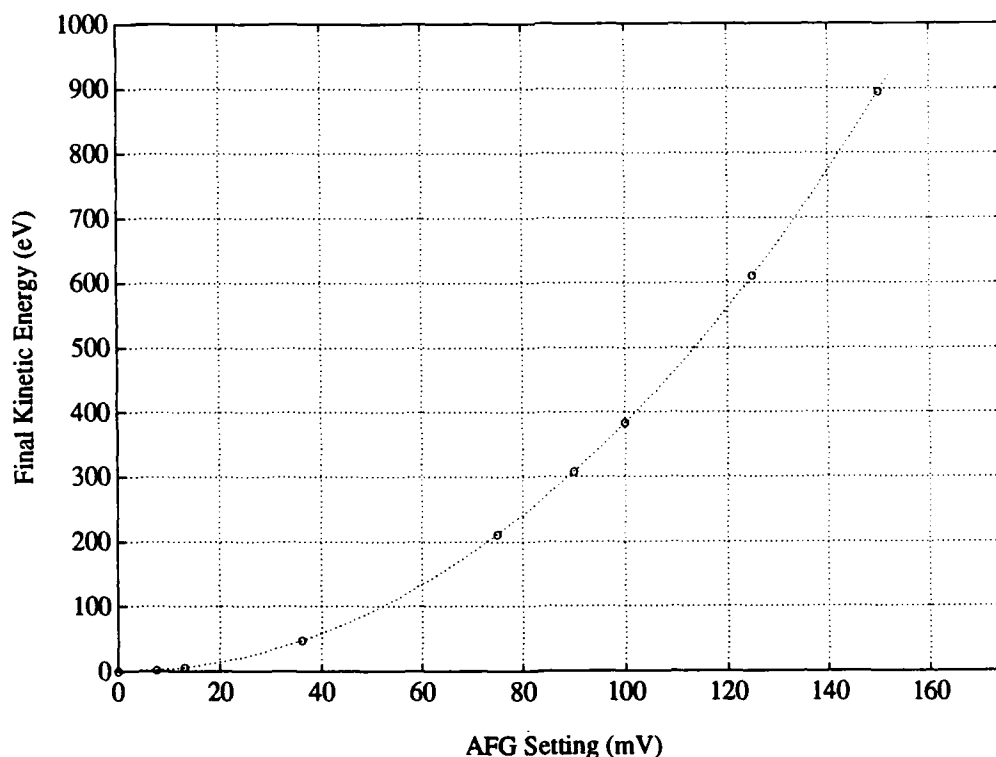


Figure 12. Ion Kinetic Energy vs Excitation Amplitude. The ion's initial position was taken to be the trap center, with no initial velocity. The excitation amplitude was varied by changing the amplitude out of the AFG, which is amplified by the wideband rf amplifiers onto the excite plates. The excitation duration was $200 \mu\text{s}$.

of $200 \mu\text{s}$. The trap potential was -1 V and the ion was taken to have unit charge of -1 . For an ion at the trap center, these conditions resulted in a radius of $1.158 \pm 0.008 \text{ cm}$ and an energy of $199.6 \pm 0.05 \text{ eV}$ (the quoted error bars represent the computational error and not the error obtained by propagating the uncertainties of the inputs—magnetic field, trap geometry, etc). The simulation series was performed by varying the initial position along one axis while maintaining the initial position along the other two at 0 cm . After the excitation was complete, the ion settled into a stable cyclotron orbit (space charge and collisions ignored), with axial motion (when $z_0 \neq 0 \text{ cm}$) and magnetron motion (when x_0 or $y_0 \neq 0 \text{ cm}$) superposed.

The I^- kinetic energy is shown as a function of initial position in Figure 13. For $|x_0| \geq 1.5$ cm and $|y_0| \geq 1.0$ cm the ion was radially ejected. Figure 13 shows quantitatively

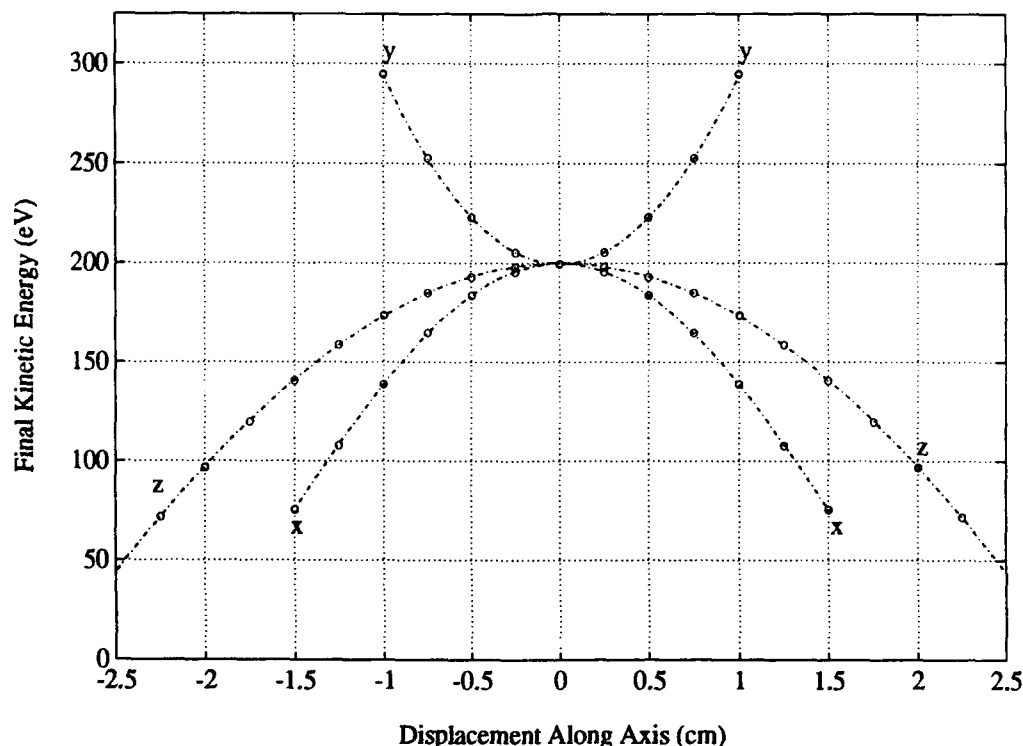


Figure 13. Ion Kinetic Energy vs Initial Position. The three curves represent a series of simulations in which the initial velocity is zero and the initial position is varied along one coordinate while the other two coordinates have an initial value of 0 cm. The excitation is less efficient when the ion starts off-axis in the x - or z -direction, but more efficient when it starts off nearer the excite plates (the y -direction).

that the ion kinetic energy is nearly monoenergetic for small displacements away from the trap center.

To construct the probability distribution for kinetic energy, the spatial distribution of the ions must be postulated. In the detachment experiments reported in Chapter 5, there is a long delay between ion formation and ion excitation to allow the ions to thermalize and relax to the bottom of the trapping well. For an ensemble of ions at thermodynamic

equilibrium in a potential field, the spatial distribution is defined by the Boltzmann distribution: $n(z) = n_0 e^{-V(z)/kT}$. For a temperature of 298 K in a 1 V trap, the distribution has the form shown in Figure 14. The dashed line indicates the magnitude of trapping

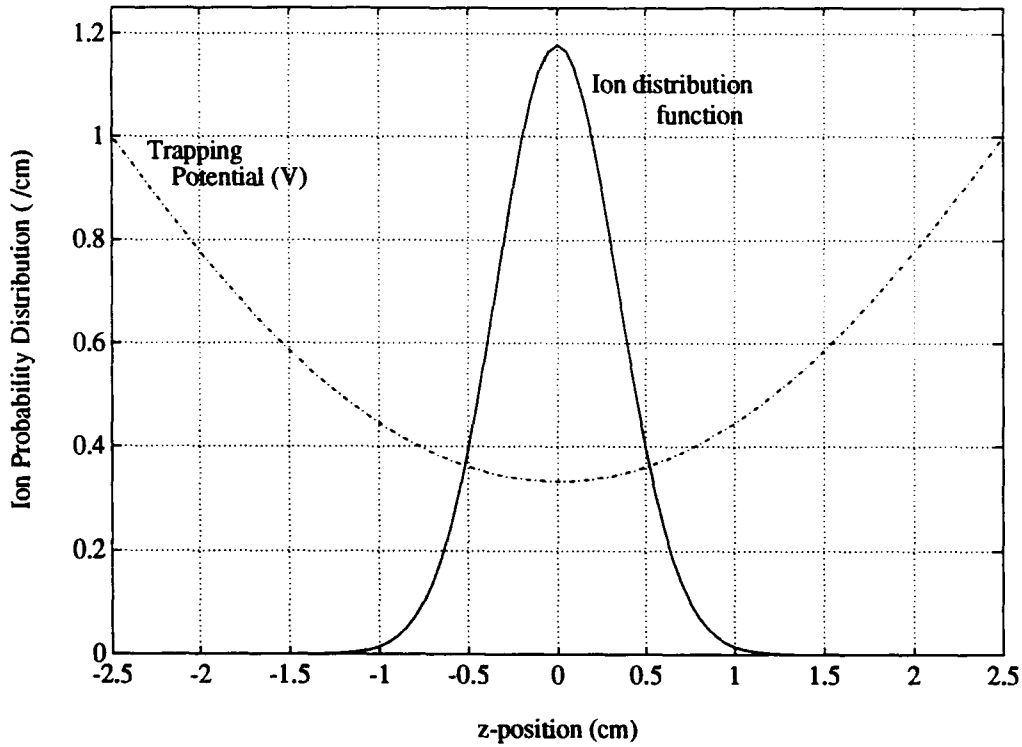


Figure 14. Spatial Distribution of Ions along **B** in a 1 V Trap. Ions are taken to be in thermodynamic equilibrium at 298 K, with spatial initial conditions as discussed in the text. The ion probability distribution, or spatial distribution function, is normalized to unity.

potential (in volts) and the solid line shows the ion probability distribution along z . The $1/e$ folding occurs at $|z| \simeq 0.47$ cm; at thermodynamic equilibrium over 70% of the ions are positioned along the center 20% of the trap.

The ion distribution along x and y is created by the electron beam profile, which is rated to be gaussian [74]. This distribution is assumed to be of the form

$$N(x, y) = \frac{N_0}{\sigma_w \sqrt{\pi}} e^{-(x^2 + y^2)/\sigma_w^2} \quad (9)$$

where N_0 is the total number of ions and σ_w is the electron beam waist. The conductance limit for σ_w is 0.1 cm, but the true dimension is probably of order 0.01 cm. For the calculations here, σ_w is taken to be 0.1 cm, so as to provide an upper bound on the width of the ion energy distribution. The assumed spatial profile is shown in Figure 15 and is of the same general form as the one-dimensional spatial distribution along the z-axis (Figure 14).

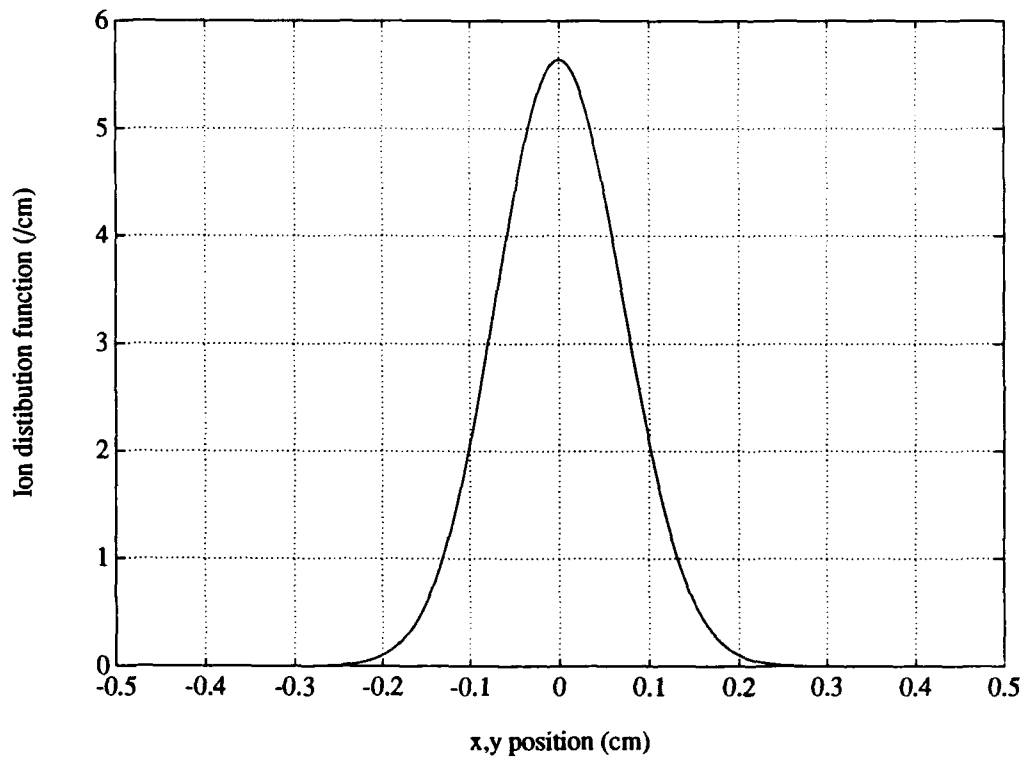


Figure 15. Spatial Distribution Function Orthogonal to **B**. Initial conditions are discussed in the text. The plot represents a worst-case assumption.

Given the spatial distribution in each coordinate and the kinetic energy as a function of initial position (Figure 13), the ion kinetic energy distribution is constructed. It has the very narrow distribution indicated in Figure 16. For this idealized case of no thermal motion, thermodynamic equilibrium along z , and a gaussian distribution along x and y , the full-width half-maximum (FWHM) is 2 eV. The most probable energy, which indeed

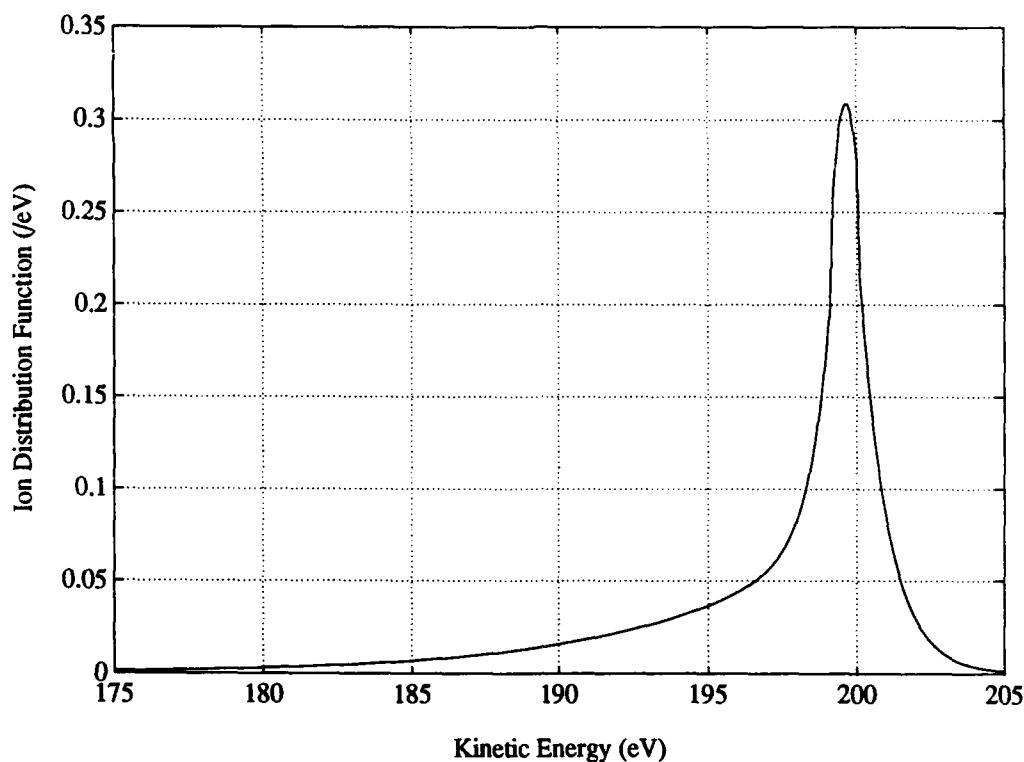


Figure 16. Ion Kinetic Energy Distribution Assuming No Thermal Motion

corresponds to an ion initially at the trap center, is 200 eV. Increasing the trap potential will compress the ions and decrease the low energy tail associated with the z -distribution. Decreasing the electron beam diameter, which was taken as the worst case (the conductance limit), will also improve the energy resolution of the distribution.

Addition of thermal motion expands the simulation parameter space; the kinetic energy distribution becomes a function of the initial velocity components as well as the initial position. The approach was to recognize the mean velocity ($v_x, v_y, v_z = 0$) results in the most probable kinetic energy and the velocity of $\pm kT$ will represent one standard deviation in the kinetic energy distribution. By running the simulation with the initial velocity permutations of $\pm kT$ and displacements along x_0 , y_0 and z_0 , the broadening of the distribution function associated with thermal motion could be estimated. Using the

same input parameters (excitation amplitude, trap potential, etc) as in Figure 16, the FWHM of the distribution function increased from 2 eV to 4 eV.

Extending this work to a variety of excitation amplitudes (AFG settings) resulted in estimation of the quality of the ion "beam" at a variety of energies. Thermodynamic equilibrium was assumed at a temperature of 298 K. The electron beam waist was taken to be the conductance limit, so the FWHM estimates are an upper limit (worst case). The energy resolution is displayed in Figure 17 as the ratio of the distribution FWHM to the

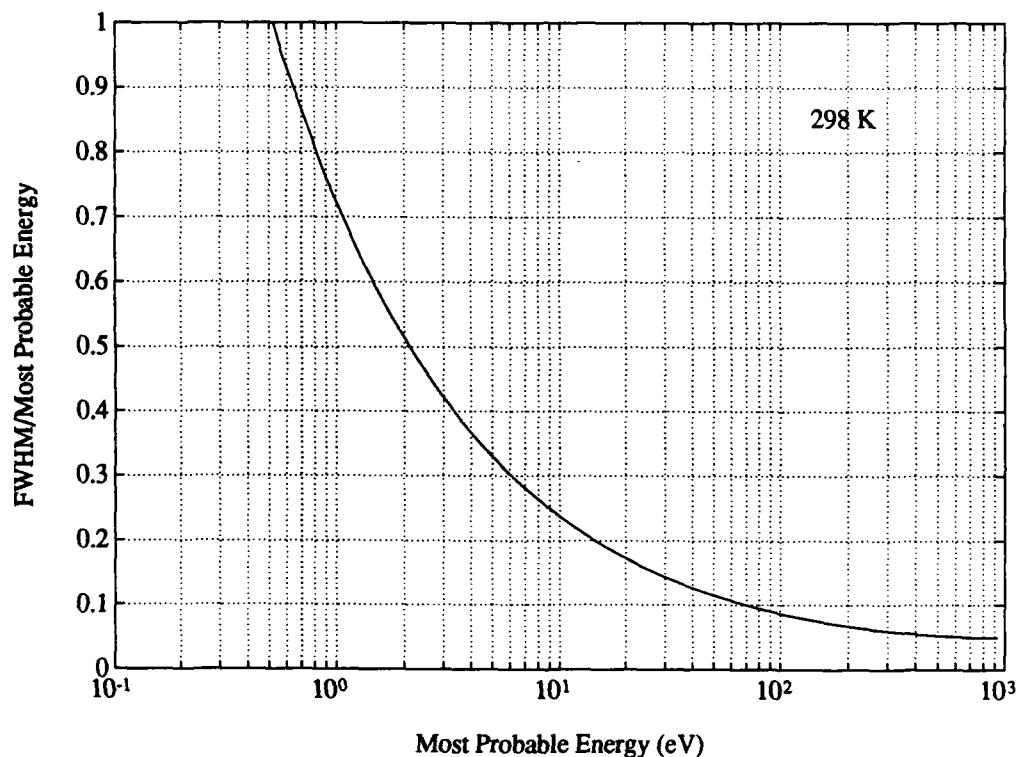


Figure 17. Ion Kinetic Energy Distribution Quality, Including Thermal Motion. The full-width half-maximum (FWHM) of the ion distribution is normalized by the most probable energy and shown as a function of the most probable energy. The gas temperature was taken to be 298 K.

most probable energy versus the most probable energy (which is a well-defined function of AFG setting). These results show that the kinetic energy distribution of I^- is reasonably narrow at all but the lowest energies.

Conclusions

Analytic representations of the time varying electric fields in a cubic ion trap have been used to quantify the excitation and detection of ions in FTMS. Ion trajectories and image currents for sinusoidal and SWIFT excitations have been computed for arbitrary trapping potentials.

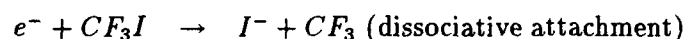
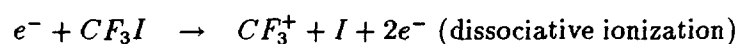
Single ion simulations, which ignore collisions, clarify sources of uncertainty in establishing the number and energy of ions based on the observed image current. These sources include excitation oversampling, excitation waveform, initial ion positions, trapping potentials, harmonic distortion, and space charge.

The FTMS ion cell is an efficient particle accelerator, permitting formation of a coherent ion packet. For iodine anions, excitation to a most probable energy of 200 eV results in a kinetic energy distribution with a full-width half-maximum of 4 eV.

III. Ion Production from Electron Impact on Trifluoromethyl Iodide

Purpose

The previous chapter linked the excitation, ion trajectory and observable image current in the FTMS experiment. This chapter tests the simulations through measurement of electron impact collisions, with reactions like:



Initially, there was concern the dissociative attachment cross section was large enough at high energy (above 10 eV) to permit efficient anion production using FTMS, since most dissociative attachment resonances occur at low energy (for example, [48, 104, 106]). Straightforward production of negative ions was desirable for the collisional detachment measurements, the primary objective of this dissertation. The purpose of this chapter is to report the measurements of the total negative ion production cross section for electron impact from ~10–50 eV on trifluoromethyl iodide (CF_3I). Ionization (total and partial) cross sections are also reported over the same energy range for the first time.

This chapter discusses why CF_3I was chosen as the source of negative ions, provides a broad discussion on previous work, describes the experimental approach and presents the quantitative results for ion production.

Why Trifluoromethyl Iodide?

Trifluoromethyl halides (CF_3X , where $X = F, Cl, Br, I$) have received interest for a potential role in lasers (atomic [39], chemical, nuclear pumped [6]), for their prolific ability to produce negative ions, and for their interesting collisional steric effects. This chapter and the next present experimental studies of one of the trifluoromethyl halides, CF_3I (trifluoromethyl iodide).

CF_3I was chosen for several reasons. As suggested by a colleague [107], negative ion production of I^- via electron impact has a large attachment cross section which could

provide the efficient production of negative ions critical to the collisional detachment experiments. Iodine has a single stable isotope, with a mass (126.9045 amu) in the optimal excitation and detection range for FTMS (see Appendix A). The single isotope has the advantage of straightforward data analysis but the disadvantage of preventing quantification of resonant charge transfer. CF_3I is nonflammable and there is no evidence that it is toxic.

Background

Previous work on CF_3I generally falls into three broad classes of experimental study: *photon* (photoionization [9, 102, 114, 112], photodissociation [39, 65, 112, 127], photoelectron spectroscopy [12, 112], etc) and collisional: *electron impact* [1, 9, 57, 59, 127] and *atomic impact* [13, 17, 51, 95, 99, 118, 126]). Probably because of the difficulty in addressing relativistic and the various coupling (spin-orbit, orbit-orbit, spin-spin, etc) corrections associated with the heavy iodine nucleus (for example, [141:17–21]), no electronic structure calculations of CF_3I could be found.

Photon Studies. Photoionization and photoelectron spectroscopy studies have investigated ionization and appearance potentials associated with CF_3I^+ and its fragments. As seen in Figure 18 (reproduced from [112:Figure 4a]), the CF_3I^+ ground state has a doubly degenerate spin-orbit doublet (term symbols $\tilde{X}^2E_{3/2}$ and $\tilde{X}^2E_{1/2}$) separated by about 0.6 eV. This is similar to iodine, which has a doublet separation of 0.94 eV [127:5100]. The two states have the same degeneracy, so they are populated with equal probability by electron impact at energies well above threshold [127:5100].

The lowest ionization potential (about 10.25 eV) is associated with the removal of an *I* lone pair orbital [12:1224] or [35:3709], while the next ionization potential (13.35 eV in Figure 18) is associated with removal from the *C–I* bonding orbital [12:1225] or [35:3709]. Higher ionization potentials are associated with *F* lone pairs, degenerate *CF* bonding and degenerate *F* lone pairs [35:3709]. A summary of relevant ionization potentials is shown in Table 2. The references for each compound are listed in chronological order.

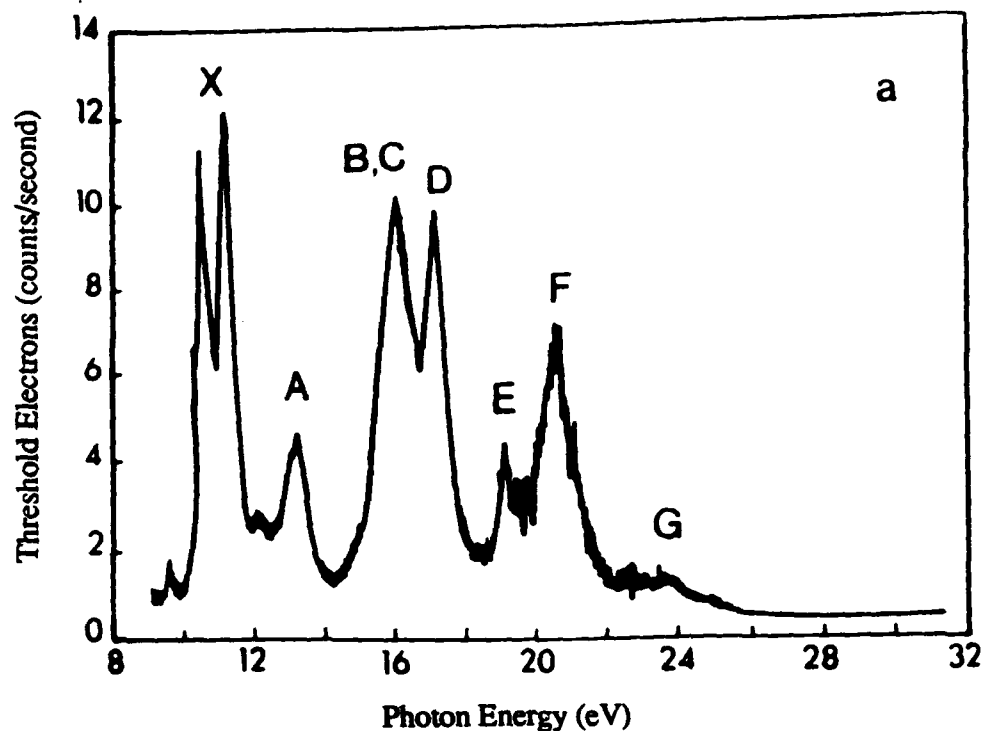


Figure 18. Photoelectron Spectroscopy of CF_3I

Within 1 eV of the ionization potential, fragment ions begin to appear. Table 3 summarizes the appearance potentials of these fragments. Coupled with thermochemistry data, the ionization and appearance potentials can be used to deduce bond energies (as summarized later in Table 4).

The lifetime of the spin-orbit excited CF_3I^+ is speculative. Several authors noted the possibility of excess energy in CF_3I^+ (for example, [102:482]) affecting experimental results, although the thermodynamic dissociation limit is only about 1 eV above the ground state [127:5101]. Thorne and Beauchamp [127] suggest the lifetime may be comparable to $I(^2P_{1/2})$ at 0.11 s or $Xe(^2P_{1/2})$ at 0.056 s. Jarrold et al. [65] agree the lifetime is much longer than a rotational period but their observed unimolecular dissociation rate is greater than $10^6 s^{-1}$ (implying a lifetime of less than a μs). Likely mechanisms for decay of the excited state are collision induced radiative transition, radiationless internal conversion [127:5104] and collision induced dissociation [65] to almost exclusively $CF_3^+(^1A_1) + I(^2P_{3/2})$

Table 2. Ionization Potentials of CF_3I and Associated Fragments

Compound (state)	Ionization Potential (eV)	Reference
$CF_3I(X^2E_{3/2})$	10.23	[102]
	10.8	[12]
	10.29	[127]
	10.32 ± 0.03	[9]
$CF_3I(X^2E_{1/2})$	11.37	[12]
	10.91	[127]
CF_3	9.25 ± 0.04	[84]
	8.62	[102]
	9.17	[133]
	9.14	[9]
	8.8	[99]
CF	9.23 ± 0.08	[133]
	9.11	[99]
$I(^2P_{3/2})$	10.45	[120]
$F(^2P_{3/2})$	17.42	[120]

[127:5101]. No explanation for the wide range of experimentally observed CF_3I^+ metastability was offered.

Photon studies have also examined vibrational modes. Multiphoton (for example, [127]) and single photon (for example, [65]) dissociation studies have identified the most common stretching modes in CF_3I^+ .

Table 3. Appearance Potentials Associated with CF_3I

Fragment (state)	Appearance Potential (eV)	Reference
CF_3^+	10.89 ± 0.01	[102]
	11.36 ± 0.02	[9]
	10.91	[112]
$I^+(^3P_2)$	12.70	[112]
$I^+(^3P_0)$	13.50	[112]
$I^+(^3P_1)$	13.58	[112]
CF_2I^+	14.58	[9]
	13.40 ± 0.05	[112]
CF_2^+	17.62	[112]

Although negative ions were observed in a matrix (CF_3I frozen into solids of argon [114] or tetramethylsilane [52]), only Berman et al. [9] has reported photon induced production of negative ions (I^-) in the gas phase. They believe the I^- was not produced by the pair process $CF_3I + h\nu \rightarrow CF_3^+ + I^-$, but rather by dissociative attachment involving low energy photoelectrons. The latter is supported by the recent low energy attachment measurements of Alajajian et al. [1], which are discussed further below.

Collisional Studies. Collisional studies of CF_3I also contribute to data on ionization and appearance potentials, with less restrictive selection rules than the photon studies. Knowing the ionization and appearance potentials, along with thermochemistry data, permits deduction of bond energies (see Table 4). The $C-I$ bond strength is about 2.2 eV in neutral CF_3I , but ~ 0.4 eV in the negative ion, CF_3I^- .

Table 4. Bond Energies Associated with CF_3I

Bond	Energy (eV)	Reference
$I:CF_3$	2.32 ± 0.17	[40]
	2.28 ± 0.04	[102]
	2.2 ± 0.2	[95]
	2.28 ± 0.05	[103]
	2.05 ± 0.2	[126]
	2.0 ± 0.2	[27]
$F:C$	5.45	[102]
	≤ 5.6	[57]
$I^-:CF_3$	1.2 ± 0.4	[95]
	0.38 ± 0.1	[126]
	0.35 ± 0.2	[27]
	0.29 ± 0.2	[27]

Atomic collisional (neutral atom + CF_3I) experiments have identified steric effects. This class of experiments [13, 17, 27, 51, 85, 95, 118, 126] accelerated alkali atoms (K, Na, Cs) onto CF_3I to show the collisions had an outcome dependent on the orientation of the CF_3I . If the alkali atom approaches at the I end (called "heads"), an alkali- I diatomic molecule can be formed and is scattered backward in the center of mass frame. If the alkali approaches at the CF_3 end ("tails"), the diatomic molecule is scattered forward.

The atomic collisional experiments also detected negative ion production. I^- is the dominant product, although CF_3I^- (which won't be observed at low pressure by electron impact due to conservation of energy and momentum), F^- and IF^- were also reported (for example, [126]). Energy resolved charge transfer measurements permit estimation of the electron affinity, as shown in Table 5, although accurate measurements of the electron

Table 5. Electron Affinities of CF_3I -Related Negative Ions

Compound	Electron Affinity (eV)	Reference
F	3.400	[120]
I	3.07	[95]
	3.063	[126]
	3.066	[120]
	3.0591 ± 0.0001	[139]
CF_3I	2.2 ± 0.2	[95]
	1.4 ± 0.2	[126]
	1.29 ± 0.2	[126]
	1.54 ± 0.2	[27]
	1.60 ± 0.2	[27]
CF_3	1.7 ± 0.2	[60]
FI	1.0 ± 0.2	[57]
CF_2	0.179 ± 0.005	[100]

affinity are best obtained with photoelectron spectroscopy [100, 139].

The anion production and steric effects led to an understanding of "heavy-heavy" collisions involving CF_3I . A "harpoon" mechanism [51] and a "spectator stripping" model [126] appear to explain the experimental results. Both models involve initial electron transfer from the alkali atom to CF_3I . This transfer results from the crossing of covalent and ionic potential energy surfaces. In accordance with the Landau-Zener [143] relation, the crossing is adiabatic; the electron "jumps" to the molecule. Electron spin resonance data suggests the electron resides unpaired in an $a_1(\sigma^*)$ antibonding orbital composed largely of p orbitals ($C-I$) which lie along the C_{3v} symmetry axis of CF_3I^- [52:68]. The CF_3I^- then dissociates within a vibrational period. Since the electron is in an orbital centered mainly on I , the decomposition is generally to $CF_3 + I^-$. McNamee et al. [95]

observed exclusively $CF_3 + I^-$ (rather than $CF_3^- + I$), although Heni and Illenberger [57] observed very small amounts of CF_3^- in an electron impact study.

After the prompt CF_3I^- dissociation, there is a strong coulomb attraction between the alkali ion and the halide anion (I^-). If the second potential energy surface crossing is diabatic, then the electron stays with I^- [51]. This is the spectator stripping reaction—the CF_3I has stripped an electron from the alkali. The harpoon mechanism results if the alkali ion and halide anion leave together as a neutral diatomic molecule. This exit channel is estimated to be complete at about 7 Å (the second crossing point) for $K + CF_3I$ [51:1095].

Near threshold there is not enough energy for the ion fragments to separate against the Coulomb potential. Passing back through vibrational crossings, CF_3I^- may relax to a bound state. Indeed, McNamee et al. [95] observed the reaction $K + CF_3I \rightarrow K^+ + CF_3I^-$ had a threshold of 2.1 eV and a peak cross section at about 3.3 eV. Several subsequent studies also observed CF_3I^- in the gas phase. But the relaxation process may result in conversion to translational energy, which again permits the ions to escape [126]. Therefore, the spectator stripping model is applicable at higher energies.

Electron impact studies are obviously relevant to this dissertation. Previous work included experimental techniques of FTMS [8], ICR mass spectroscopy, time of flight (TOF) mass spectrometry and krypton photoionization [1]. These reports examined positive ion kinetics, negative ion production and, briefly, ionization.

One mechanism for creation of negative ions is dissociative attachment. The attachment process is analogous to the spectator stripping model—a free electron undergoes capture to form CF_3I^- , which then promptly dissociates. Low energy dissociative attachment is often exothermic (true for CF_3I because the electron affinity of I exceeds the the $C-I$ bond strength) and has very high cross sections [57:314]. There is an abrupt onset of negative ion formation at zero energy, in accordance with Wigner threshold law for attachment [1:3629].

These general features of dissociative attachment have been observed experimentally. Alajajian and others measured dissociative attachment at ultralow energies (0–160 meV)

using the krypton photoionization method [1]. Their results (reproduced from [1:Figure 3]) are shown in Figure 19. The cross sections for production of I^- are very large (10^{-15} – 10^{-13} cm^2), although they are still a factor of 2–10 below the theoretical maximum s -wave

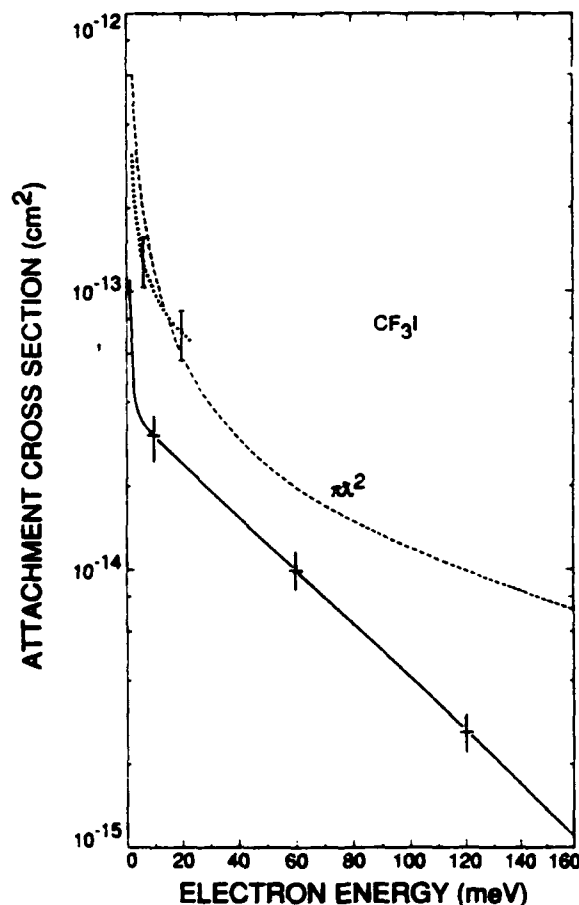


Figure 19. Dissociative Attachment Cross Section for Production of I^- in CF_3I

capture cross section (indicated by the dashed line in Figure 19).

They parametrized their attachment cross sections to the form

$$\sigma_{att}(\epsilon) = 3.81 \times 10^{-14} [0.0698 \epsilon^{-1/2} e^{-1.67 \times 10^5 \epsilon^2} + e^{-22.0 \epsilon}], \quad (10)$$

where ϵ is the electron kinetic energy in eV and σ_{att} is the attachment cross section in cm^2 . Equation (10) was then used with a maxwellian energy distribution to compute attachment rate constants, $\langle \sigma_{att} v \rangle$, as a function of energy. The rate constants are very large, in the range of $1\text{--}2 \times 10^{-7}$ cm^3/s over the energy range measured (0–160 meV).

Alajajian et al. noted I^- was the primary dissociative attachment channel [1:3630], but they made no mention of any other negative ion types. Only Heni and Illenberger [57] have reported other dissociative attachment channels. They measured negative ion production using 0–17 eV electrons with a quadrupole mass spectrometer and observed I^- , F^- , FI^- and CF_3^- . Their results (reproduced from [57:Figure 1]) are shown in Figure 20. I^- was by far the most common fragment, with a narrow resonance near 0 eV.

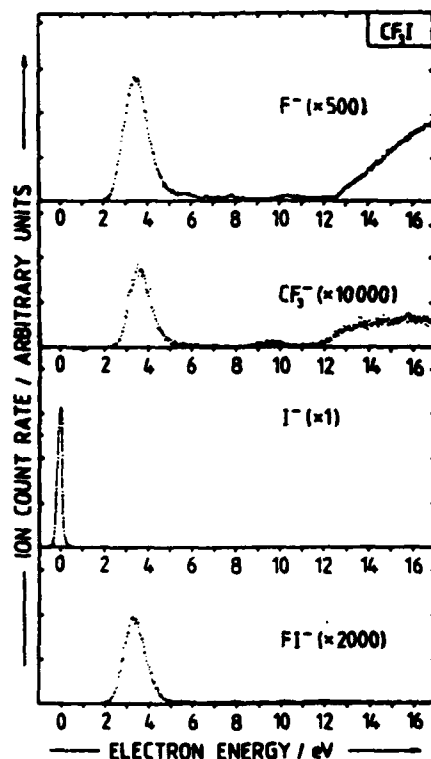
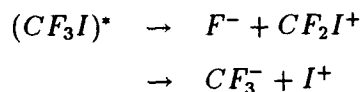


Figure 20. Dissociative Attachment Channels in CF_3I

The small amount of I^- that was observed above 0 eV was attributed to scattered thermal electrons. As seen in Figure 20, the other three fragments exhibit a broader resonance near 3.8 eV. Only F^- had substantial (relatively speaking) production above 12 eV. Unfortunately, the scale of Figure 20 does not permit determination whether the production of I^- exceeds F^- at high energies and the authors did not address this issue. It is also difficult to

ascertain whether contaminants are the source of the trace anions. The production of F^- and CF_3^- were attributed to the non-resonant pairing reactions of excited neutral CF_3I :



If true, CF_2I^+ and I^+ would have lower appearance potentials than permitted by dissociative ionization, due to the exothermicity associated with the electron affinity of F^- and CF_3^- .

Positive ion production from CF_3I has been reported only at a single energy. Berman et al. [9] used ICR instrumentation to report the abundant ions formed by 70 eV electrons at pressures below 10^{-6} torr are CF_3I^+ (37.6%), I^+ (32.9%), CF_3^+ (18.0%) and CF_2I^+ (11.5%) [9:48]. They did not report on any other fragment ions.

Summary. Photon and collisional studies have measured the key thermodynamic parameters associated with CF_3I . Photoionization studies have examined CF_3I orbital structure and have identified a spin-orbit splitting in CF_3I^+ . Heavy-heavy collisional studies have examined steric effects and negative ion production, which provided insight into the mechanism of electron transfer. Electron impact studies measured attachment cross sections for production of I^- at very low energy and the relative production rate of other negative ion fragments. Dissociative ionization branching ratios have been reported for only a single electron energy (70 eV).

Experimental Background

CF_3I was procured from Aldrich Chemical, at 99% purity. No additional purification was performed. Argon (Ar) was procured from Matheson Gas Products and xenon (Xe) was procured from Airco Specialty Gases, both at grade 5 (99.999%) research purity.

A detailed presentation of the experimental apparatus is found in Appendix A. Ion measurements were performed using three excitation waveforms, two sinusoidal and one SWIFT. For iodine, a 200 μs long sinusoid was created at 239.64 kHz. As discussed in the previous chapter, trajectory simulations predicted an AFG setting of 75 mV (a peak

rf output of 7.8 V) gives an iodine ion at the trap center a radius of 1.16 cm. For CF_3I^+ and Ar^+ , a 300 μ s long double sinusoidal excitation was created using superposition of two resonant sinusoids (CF_3I^+ at 155.18 kHz and Ar^+ at 761.42 kHz). The advantage of the double sinusoid is, at least within the variance of the rf amplifiers, the final radii will be the same for both CF_3I^+ and Ar^+ . Simulation predicted an AFG amplitude of 100 mV (a peak rf output of roughly 2.65 volts at each resonant frequency) generates a radius of 1.15 ± 0.025 cm. Since FTMS detection is linear (to first order) in radius, equivalent numbers of ions will generate equivalent peak magnitudes.

A wideband SWIFT waveform was also constructed. It has a flat power spectrum from 60 kHz–2.05 MHz (mass range 15–500 amu). The standard AFG amplitude setting was 700 mV, which created a peak rf output of about 75 volts. Simulation showed the final radii (for ions initially at the trap center) was 0.96 ± 0.07 cm, where the error bar is mostly attributed to the spectral variation in rf amplifier gain.

For all measurements reported below, the excitation waveforms were clocked out of the AFG at 20 megasamples per second (an excitation Nyquist frequency of 10 MHz). This provided adequate oversampling for all detectable ions (mass ≥ 16 amu), as discussed in Chapter 2.

Every experiment has a timing sequence controlled by the digital-to-analog convertor (DAC; see Appendix A for details). For the ionization measurements, the electron gun was pulsed for 2 ms and the rf excitation was triggered 10 ms after the gun turned off. Normally, it is desirable to allow the ions to relax to the bottom of the potential well before excitation, but ion kinetics (discussed in the next chapter) dictated a prompt excitation. For the negative ion production measurements, the electron gun was pulsed much longer (52–80 ms) and the rf excitation trigger was somewhat later (30–50 ms).

The ion signal was acquired using a LeCroy 9410 oscilloscope. Signal acquisition was triggered 150 μ s (negative ions) or 200 μ s (positive ions) after the rf excitation was complete. A total of 10,000 data points were sampled at a Nyquist frequency of 5 MHz (10 megasamples per second), which meant the total duration of the acquired time domain was

1 ms. There were 250–700 (ionization measurements) or 300 (negative ion measurements) samples averaged at each electron energy.

Any other experimental parameters were specific to the type of measurement being made and can be found within each category below.

Ionization Measurements

A combination of CF_3I and argon (Ar) were loaded into the lower manifold, with an initial mixing ratio of 8.9 to 1, as measured by the 1000 torr capacitance manometer. The idea was to calibrate the CF_3I^+ signal to the well known cross section for Ar^+ [140]. Subsequent pulsed valve calibration placed the CF_3I partial pressure at 180 ± 16 ntorr (sinusoidal measurements) and 135 ± 6 ntorr (SWIFT measurement). The partial pressure of Ar was never calibrated, for reasons discussed further below, but was approximately 10% of the CF_3I partial pressure. For both sets of measurements, the trapping potential was +2 V.

Time domain ion signals were zero-filled to 256k and Fourier transformed. Peak values of the magnitude spectra were extracted and compensated for the variation in electron gun output and for the variation in preamplifier gain (bandwidth). The corrected peaks were plotted versus electron energy, as shown in Figure 21. In theory, the CF_3I^+ cross section could be computed by simply dividing the CF_3I^+ peaks by the pressure ratio (about 9:1) and calibrating to the well known Ar cross sections.

In practice, several problems arose. The gas mixture flowing into the vacuum chamber was something higher than a 9:1 ratio. Presumably because CF_3I has a much higher polarizability and is much heavier than Ar , there was a problem with settling and diffusion in the manifold. The ion ratios (CF_3I^+/Ar^+) were monitored and they evolved over several days. Therefore, the CF_3I cross sections could not be calibrated based simply upon the nominal manifold mixture.

In addition, the 9410 oscilloscope is an 8-bit ADC. Since the ionization potential for Ar is over 5 eV higher than it is for CF_3I , one might anticipate the production of CF_3I^+ to exceed Ar^+ for all electron energies of interest. By setting the pressure ratio

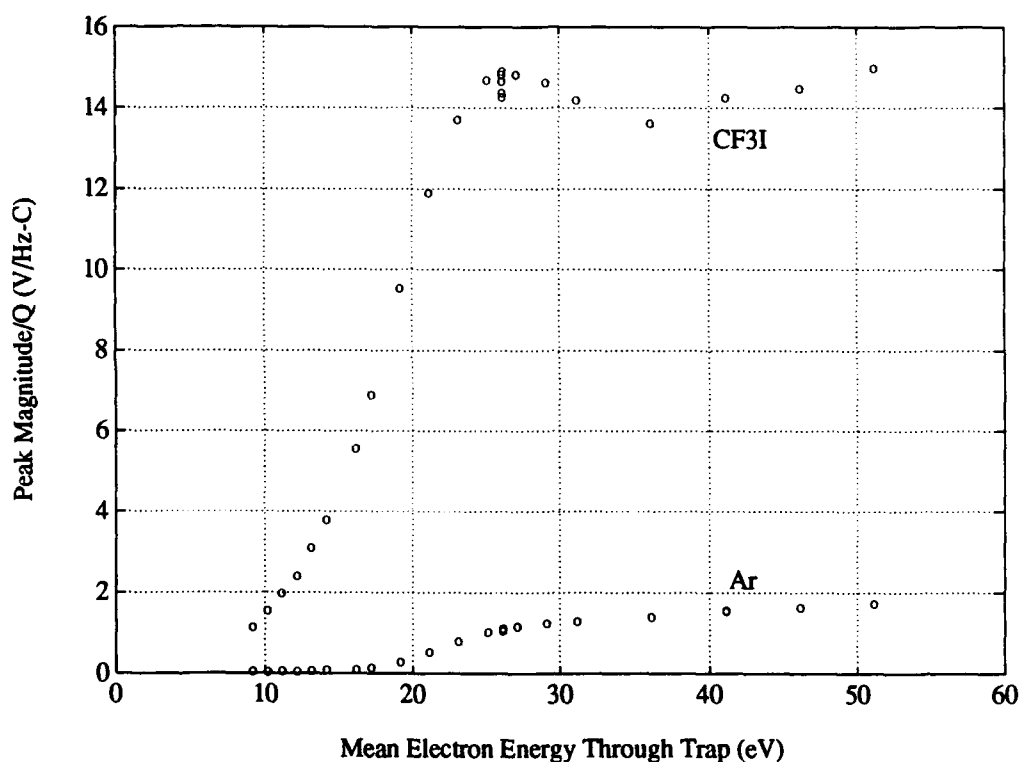


Figure 21. *Ar* and *CF₃I* Peak Intensities vs Electron Energy. The *Ar* signal is much smaller because the nominal gas mixture is 1:8.9 (*Ar*:*CF₃I*).

heavily in favor of *CF₃I*, the *Ar*⁺ ion signal was using only 1-4 bits of the ADC. This raises the systematic error associated with detection, which is only $\pm 0.2\%$ for a full scale signal, to $\pm 3\text{--}50\%$, thereby reducing the reliability of the *Ar* data as a calibration point. The (relatively) high ionization potential of *Ar* also made it susceptible to charge transfer and chemical reactions with contaminants, particularly water vapor, and with *CF₃I* [98].

Instead of calibrating to *Ar*, the data was obtained by using the pulsed valve to calibrate the *CF₃I*⁺ peaks to xenon (*Xe*). This proved to be a better choice, in part because the ionization potential for *Xe* (12.13 eV) is closer to that of *CF₃I*. Single gas puffs (285.5 ± 6.5 ntorr for *Xe*; 150 ± 4 ntorr for *CF₃I*) were ionized at a nominal energy of 25 eV. Knowing the pressure for each species and the *Xe*⁺ cross section at 25 eV is $(3.46 \pm 0.42) \times 10^{-16}$ cm² [140:573], it was straightforward to determine the ionization

cross section of CF_3I at 25 eV is $(1.93 \pm 0.48) \times 10^{-16} \text{ cm}^2$. Using this calibration point, the cross section was mapped. The sinusoidal excitation resulted in the ionization cross sections shown in Figure 22a and the SWIFT excitation resulted in the cross sections shown

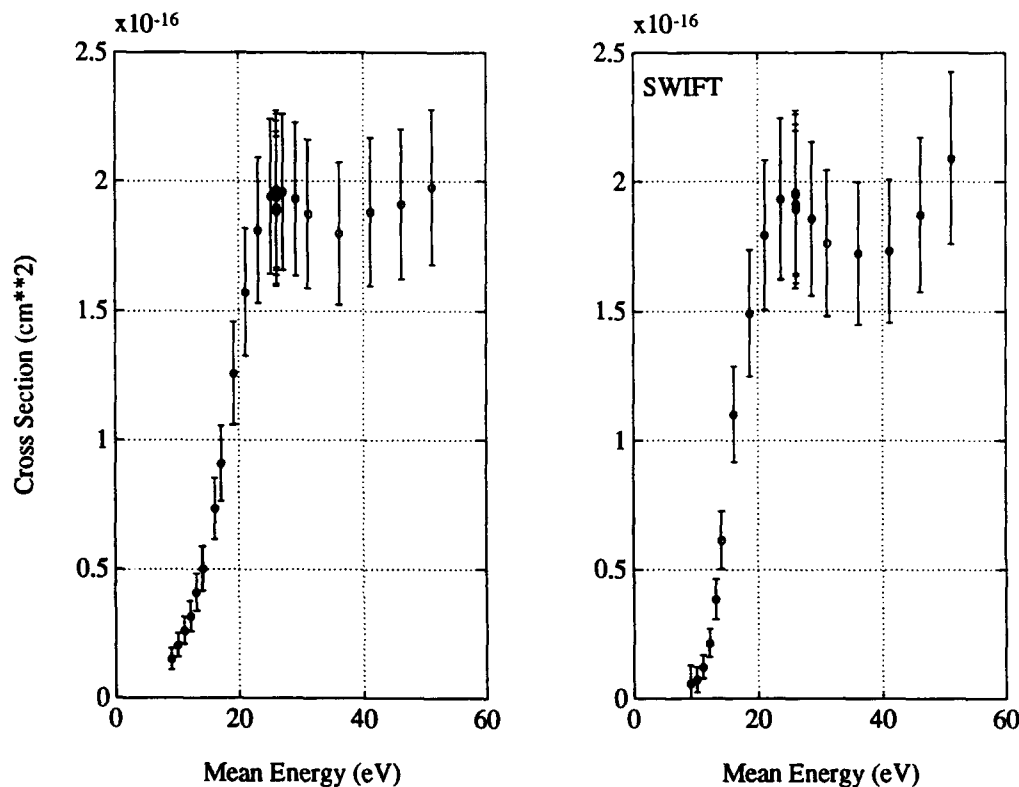


Figure 22. Partial Ionization Cross Sections for $e^- + CF_3I \rightarrow CF_3I^+$ from Different RF Excitations

in Figure 22b. Both figures show the *relative* error bars, of which the primary contributor is the pressure fluctuations which occur during the experiment (typically $\pm 5\%$). The variation in system performance can be seen in the multiple data points (five in Figure 22a) at 26.1 eV, which were dispersed throughout the data acquisition. The absolute error exceeds $\pm 30\%$, primarily because the error on the absolute Xe^+ cross section was $\pm 12\%$ and the total error on the two pulsed valve calibrations was $\pm 10\%$. The error in the mean electron energy (horizontal error bars which are not depicted) is $\pm 0.46 \text{ eV}$.

Both excitations show the same general trends of a threshold region (around 9–13 eV) and a plateau region beginning near 26 eV. The cross section appears to be non-zero below the ionization potential because of the effect of the energy dispersion of the electron beam; the mean energy (nominal energy + 1.13 eV from the trap potential) through the trap is shown as the abscissa. Figure 22a has a larger convolution near threshold, which is consistent with the electron gun output being about four times higher than in Figure 22b. A larger electron gun output increases the beam space charge, which increases the effective beam temperature. It appears the cross section passes through a local minimum between 35 and 40 eV, although conclusion of a resonance is tenuous considering the relative error bars.

Additional data was taken using the wideband SWIFT excitation with a trap potential of +1 V. Partial ionization cross sections are shown in Figure 23. As above, the error bars reflect only the relative error. There are several interesting features. To create I^+ , a C–I bond must be broken and an electron must either remain with the radical to form CF_3^- (called “polar dissociation” here) or be placed into the continuum. This is a more complicated process than simply removing an electron from CF_3I , so it is somewhat surprising that the I^+ production nearly equals the CF_3I^+ production at high energy. Cross sections are not measured above 50 eV because of secondary electron emission from the collector [48], but the branching ratios should be accurate. The abundances at 70 eV were 37% (37.6%), 14% (11.5%), 34% (32.9%), 14% (18%), 1.1% and 0.9% for CF_3I^+ , CF_2I^+ , I^+ , CF_3^+ , CF_2^+ , CF^+ , respectively. The numbers in parentheses are those reported by Berman et al. [9] and are in close agreement. Both data sets verify that the partial ionization cross section for I^+ equals (within error bars) that for CF_3I^+ at 70 eV. Also of interest, the partial cross sections for CF_3I^+ and CF_3^+ appear to peak around 25–30 eV, while the cross section for the other fragments continue to increase. The fragment kinetic energy distribution is not known, so no corrections for ion evaporation (see Chapter 2) were applied to the data.

The total ionization cross section for CF_3I is shown in Figure 24. The error bars represent the relative error. The total cross section is the sum of the parent ion plus all fragment ions (including some not shown in Figure 23), so its absolute error is also in the

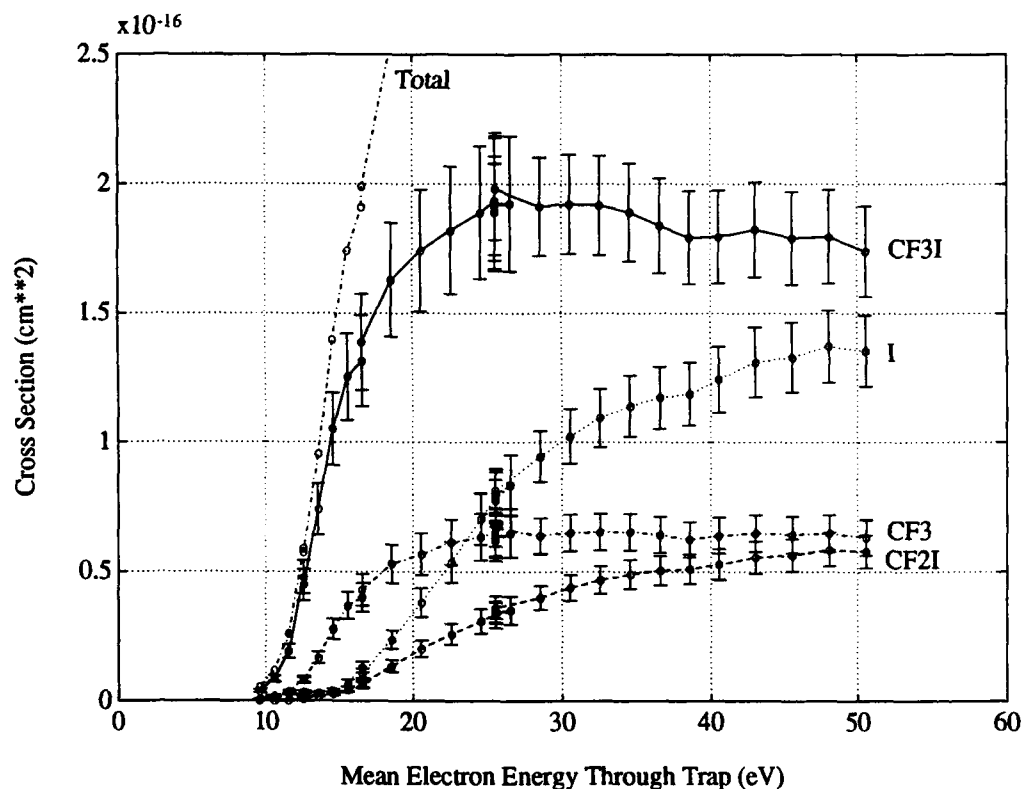


Figure 23. Partial Ionization Cross Sections for $e^- + CF_3I$. Fragment ion type is labelled at the end of each trace.

30–40% range. As seen in the figure, the total cross section may still be rising at the highest energy measured ($\bar{\epsilon} = 50.6$ eV), so the maximum value for the total cross section is bounded as no lower than 4.5×10^{-16} cm². There are no corrections for reactions in which a single electron makes more than one fragment ion (for example, $e^- + CF_3I \rightarrow CF^+ + F^+ + 3e^-$); ionization studies of CF_4 showed positive ion pair production to be exceedingly small below 50 eV [14].

Two of the “trace” fragments, CF_2^+ and CF^+ , are shown in Figure 25. The third, F^+ , is virtually negligible; its cross section never exceeds 2×10^{-18} cm² over the energy range measured. Once again, no corrections were applied for ion evaporation. CF_2^+ and CF^+ have, within relative error bars, the same cross sections. Similar results were noted in electron impact studies of CF_4 [86].

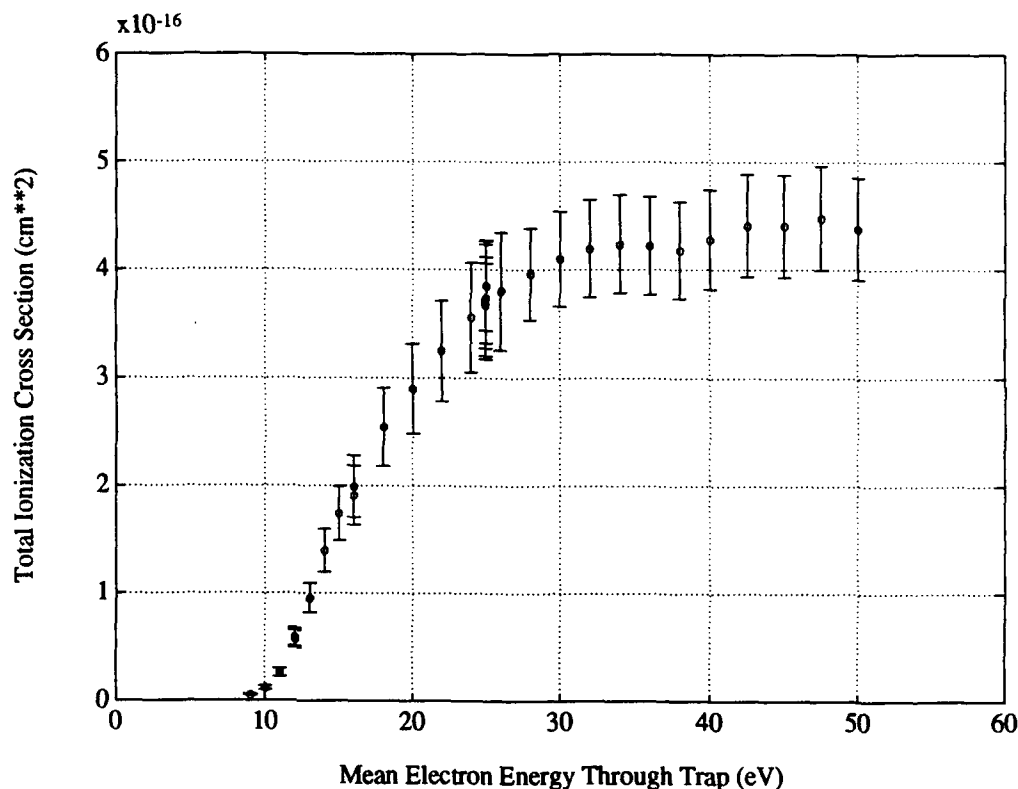


Figure 24. Total Ionization Cross Section for $e^- + CF_3I$

Deconvolution of the cross sections to account for the energy dispersion of the electron beam was not attempted. The CF_3I^+ ground state has a doublet separated by less energy than the increments (1 eV) used to map the cross section. FTMS only measures the total number of ions and cannot diagnose spin state information. The necessary resolution is not available to deconvolute the two ground state cross sections. Further, the average electron energy varies through the ion trap due to the trapping potential. For example, a trapping potential of +2 volts causes a nominal 15 eV electron beam to vary from 17 eV to 15.67 eV and back to 17 eV as it passes through the trap. This spatial dependence greatly complicates the conventional approach to deconvolution, which involves Fourier transforms over the velocity space. Finally, the determination of the energy dispersion of the beam is complicated by space charge, which increases as the beam is transported from the gun to the trap (see discussion in Appendix A).

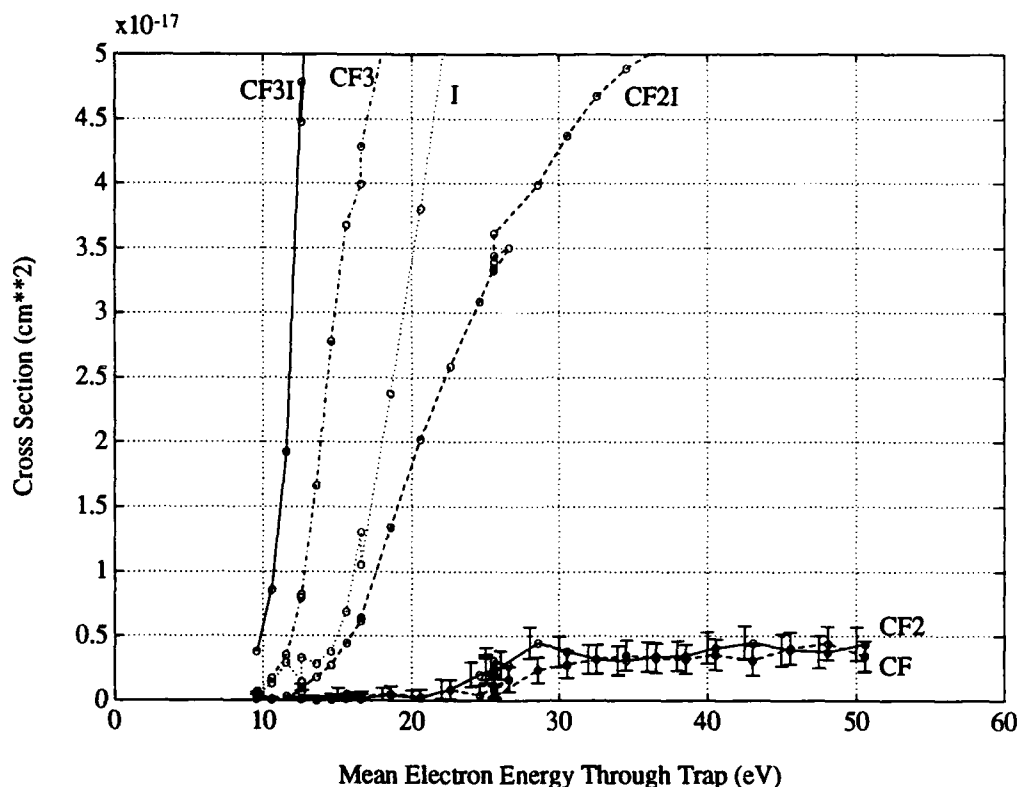


Figure 25. Ionization Cross Sections for Fragment Ions, Expanded Scale

Linear extrapolation of the cross sections were used to bound the ionization and appearance potentials. For example, (see Figure 25) the extrapolation of the CF_3I^+ cross section over the range 11.6–15.6 eV has an ionization potential bounded as no higher than 10.9 eV. Similarly, the appearance potentials are upper bounded at 11.7 eV (CF_3^+), 14.5 eV (I^+) and 14.3 eV (CF_2I^+). The systematic overestimation, as compared with the values reported in Table 3, of 0.5 eV is plausible given the energy spread of the beam due to the trap potential is almost 0.5 eV.

I^+ is interesting because it appears to have a finite partial ionization cross section with a threshold between 11 and 12 eV, but doesn't increase sharply until 14.6–16.6 eV. According to photoionization studies (see Figure 18), the structure near 15.5 eV is associated with removal of *F* lone pair electrons. From the observations here, it also appears likely there is removal from the *C-I* bonding orbital at about that energy.

Negative Ion Production Measurements

Experimental Details. Measurements were performed with undiluted CF_3I and, in one case, the CF_3I -Ar mixture. The trapping potential was -2 V. Time domain ion signals (for example, Figure 26) were zero-filled to 256k, Fourier transformed and gain corrected for the preamplifier spectral response. After gain correction, the magnitude

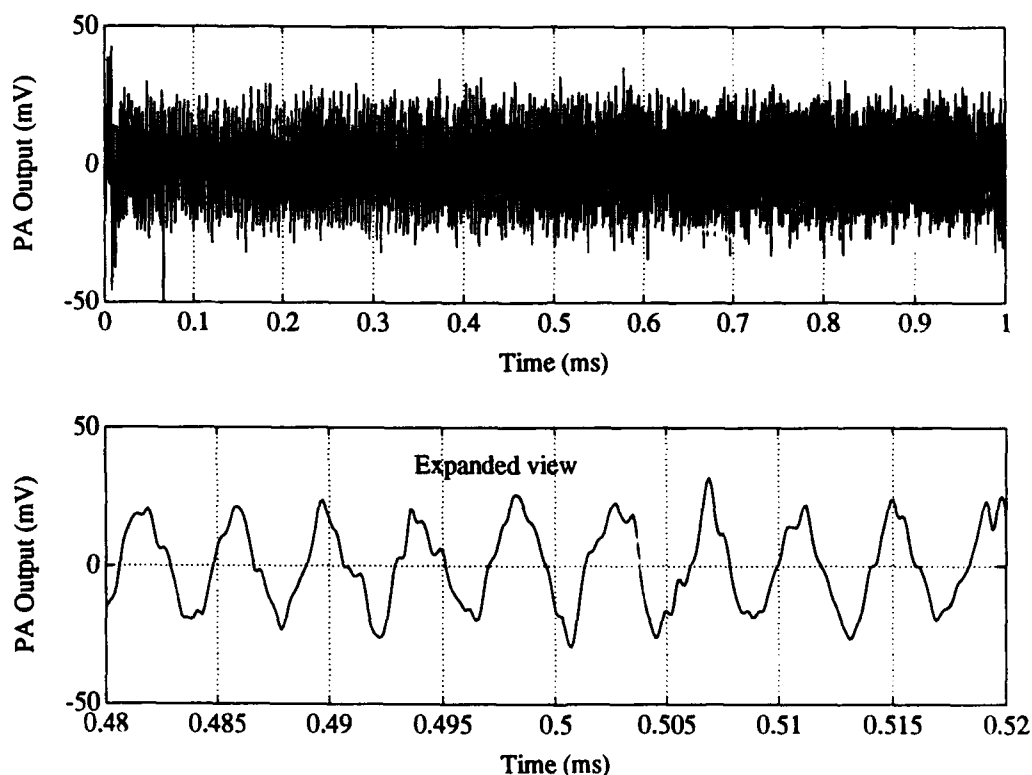


Figure 26. Typical Ion Time Domain Signal. Expanded view shows I^- oscillations.

spectrum represents the ion signal immediately before the preamplifier gain stage. If the preamplifier input impedance (nominally 25 pf) were accurately known, then the image current magnitude spectrum could also have been computed.

Data Analysis. The magnitude spectra were examined for peaks. A typical example is shown in Figure 27, where only one dominant peak, I^- , is seen. The several smaller peaks are due to system noise. For the 15 eV (nominal) electron beam, no other

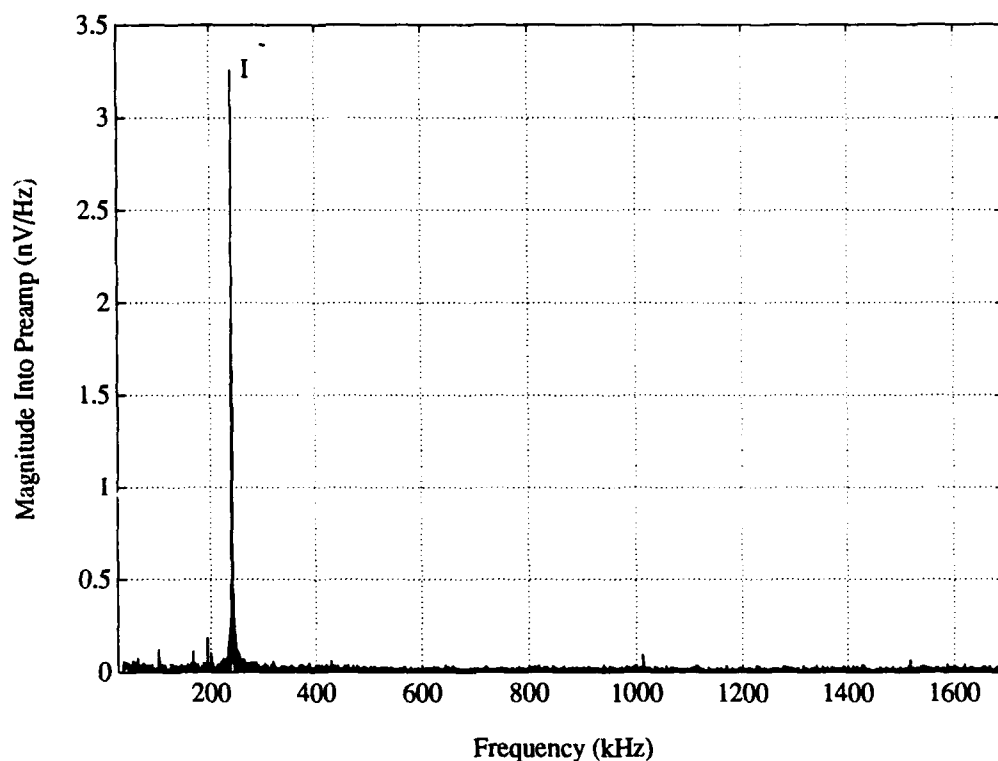


Figure 27. Typical Ion Magnitude Spectrum. The primary peak is from I^- , the next larger peaks are system noise.

negative ions were seen above the noise. Since the 9410 oscilloscope has an 8-bit ADC, the cross section of possible trace ions cannot be measured to a value smaller than the ADC systematic noise of $\pm 1/2$ bit. The observed signal becomes an upper bound for the production cross section. Table 6 lists the bounded cross sections (referenced to I^-) for a list of potential anions, some of which have never been reported and likely are not possible. The larger bound for IF^- , which has a cyclotron frequency near I^- , is due to power leakage from the I^- signal and does not imply indications of an IF^- peak. The data shows that all of the negative ions, except I^- , have either very small cross sections or none at all.

Since it was apparent that I^- was the dominant electron impact production channel, its cross section was mapped using the sinusoidal rf excitation. The data was calibrated to

Table 6. Measured Upper Bound of Potential Anions at 15 eV, Referenced to I^-

Anion	Mass (amu)	$\sigma_{anion}/\sigma_{I^-}$
F^-	19	0.0045
CF^-	31	0.0040
CF_2^-	50	0.0037
CF_3^-	69	0.0054
I^-	127	1.0
IF^-	146	0.015
CF_2I^-	177	0.0064
CF_3I^-	196	0.0086

the ionization cross section by using the pulsed valve. I^- production at 10 eV (nominal) was found to be factor of 0.00424 ($\pm 7.7\%$) smaller than the production of CF_3I^+ at 25 eV (nominal), resulting in a cross section of $(8.2 \pm 2.7) \times 10^{-19} \text{ cm}^2$. Using this calibration point, the I^- production cross section was scaled and is shown in Figure 28. Relative error bars (not shown) range from $\pm 11\%$ at 12.9 eV to $\pm 8\%$ at 2.9 eV. The absolute error is in the range $\pm 41\text{--}44\%$. The error bar on the mean energy is $\pm 0.46 \text{ eV}$. Although the cross section appears small at energies above 10 eV, let it be emphasized that the ion signal is well above the noise—there is definitely I^- created even with electron energies as high as 50 eV. Using the reported cross section for a 14 eV (nominal) beam with 200 nA for 50 ms into 200 ntorr of CF_3I , there are over 10^3 anions produced. Since the electron gun is rated from 10–1000 eV, the cross section data below 10 eV should be viewed with caution. For very low energies (less than 7–8 eV) the electron gun output falls off and focussing is not guaranteed. Therefore, the front and rear traps were monitored to make sure the beam was still collimated onto the collector.

Discussion. Until this point, the data has been loosely referred to as a “production cross section” rather than a specific process such as dissociative attachment. The reason is the non-zero cross sections apparent at high energy. Conservation of energy dictates that if I^- production is strictly by dissociative attachment, then the fragments must carry away the electron energy. From fragment mass partitioning, the I^- would have kinetic energies in the range of a few eV to 10’s of eV. Ions with large random velocity vectors are difficult

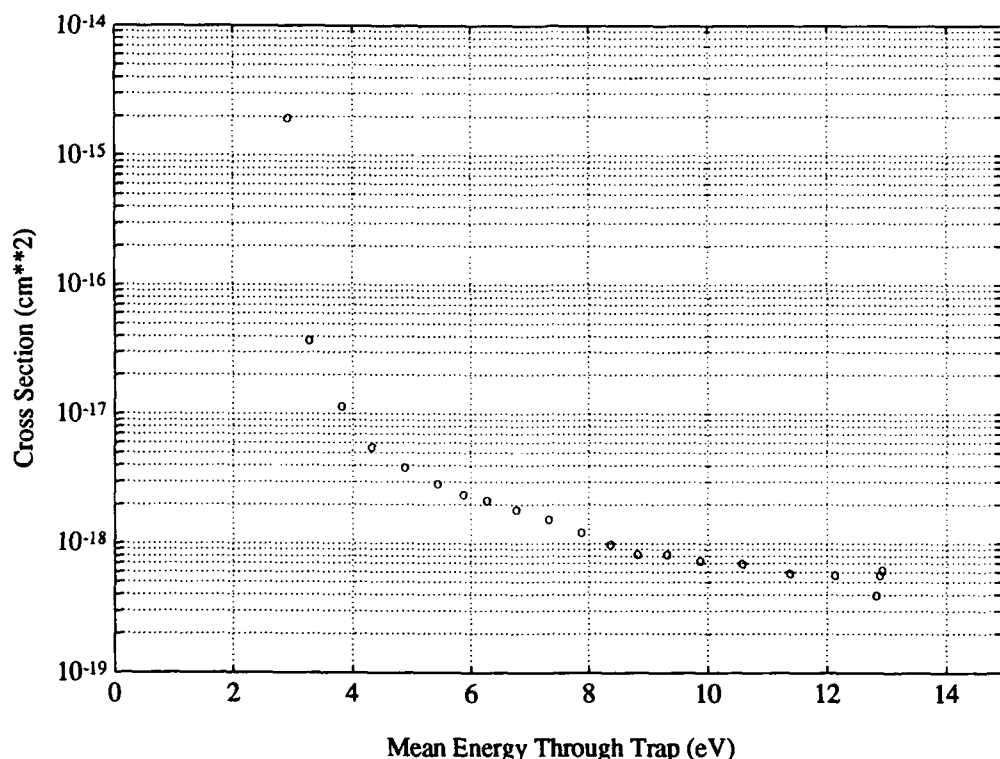


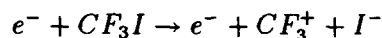
Figure 28. Electron Impact Cross Section for Production of I^- from CF_3I

to trap in the ion cell. If the negative ion production is truly by dissociative attachment only, then the actual cross section at high energies is much larger than shown in Figure 28, because a large portion of I^- would escape the ion trap before detection.

Heni and Illenberger [57] believe production at high energies is attributed to scattered electrons. Comparison of Figure 19 and Figure 28 show the attachment cross section is 5–6 orders of magnitude larger at meV energies than at 10 eV. But it is hard to justify many electrons scattering from 10's of eV to thermal energies within the spatial restrictions of the ion trap, so scattered electrons cannot be the entire explanation.

It is possible that polar dissociation plays a role in I^- production at high impact energies. In this mechanism, the electron interacts only long enough to place the CF_3I in

a high excited state so that it may polar dissociate:



The thermodynamic threshold for this process is $D(C-I) + IP(CF_3) + EA(I)$, or about 8.4 eV.

For these measurements the trap is configured to trap all negatively charged particles, including secondary electrons. At high beam energies, large numbers ($> 10^4$) of thermal electrons are trapped. Creation of I^- at high energies cannot be due strictly to thermal ionized electrons which are trapped in the ion cell and then undergo dissociative attachment at the high rate reported by Alajajian et al. [1]. If this were true, there would be a sharp increase in production near the ionization potential of CF_3I (10–11 eV) and the appearance potentials of I^+ and CF_3^+ (11–14 eV). This is not seen in Figure 28. Verification of the effect of thermal ionized electrons is seen in Figure 29, which shows data taken at a higher pressure and with a longer electron beam (80 ms) in the CF_3I -Ar mixture. The increases in I^- production at the CF_3I ionization potential (near 10 eV) and Ar ionization potential (near 15 eV) are easily seen along with an increasing slope at high (above 25 eV) energy.

The ion's internal energy is important to the dissociative attachment process [104]. As presently configured, FTMS cannot prepare or diagnose internal state information explicitly. Therefore, it is not the ideal technique to make detailed measurements of dissociative attachment.

Considering the smoothly varying nature of the cross section shown in Figure 28, it is likely that each of the processes makes some contribution to the I^- population: dissociative attachment with beam electrons, dissociative attachment with secondary electrons and polar dissociation.

Electron Impact Detachment. Electron impact detachment measurements ($e^- + X^- \rightarrow X + 2e^-$) were attempted using FTMS. The approach was to examine the evolution of the negative ion signal as a function of the electron beam time (see Figure 30). For ionization, for example $e^- + Xe \rightarrow Xe^+$, the relationship is quite linear. If electron impact

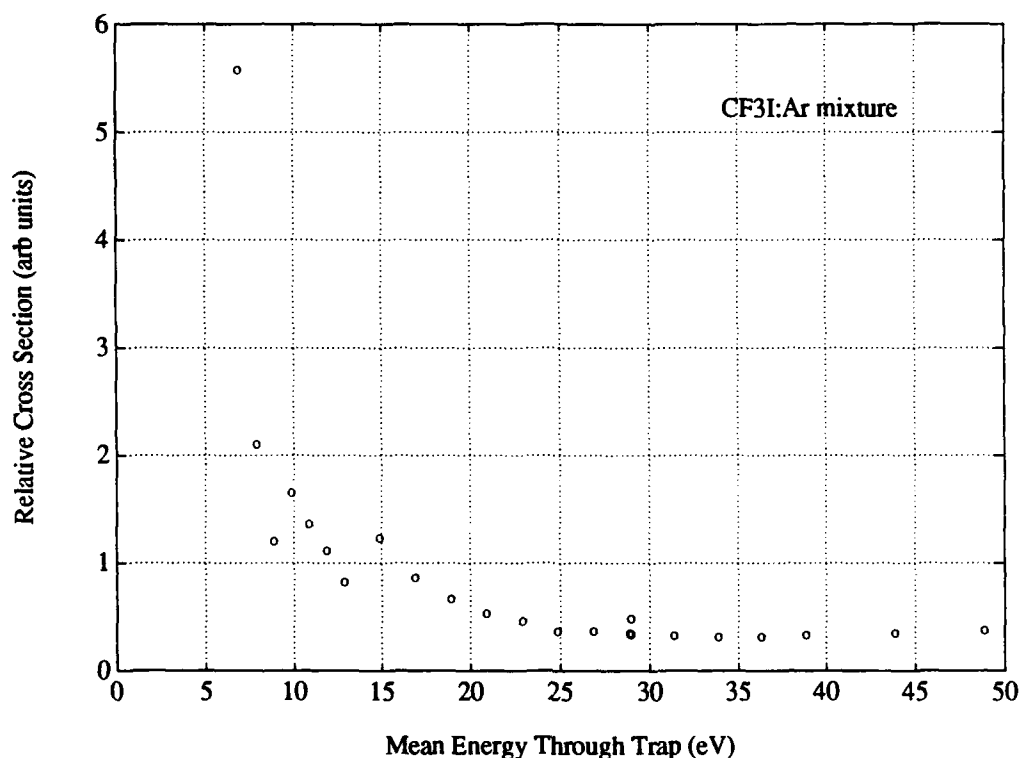


Figure 29. Relative Production of I^- in a CF_3I -Ar Gas Mixture

detachment is occurring, the curve will be concave down as it approaches some steady-state balance between negative ion production and destruction.

Negative ion detachment by electron impact has been investigated theoretically [5, 7, 38, 61, 67, 91, 101, 122, 123] and experimentally [30, 108, 109, 110, 128, 129, 134, 135]. The theoretical treatment has involved a variety of techniques (Born approximation, classical, Hartree-Fock, partial waves, etc) on predominately hydrogen ($e^- + H^- \rightarrow H + 2e^-$). Because of the difficulty in treating the Coulomb forces on the entering and exiting electron(s), theory has predicted a wide range of detachment cross sections.

Experimental studies have been performed on H^- , C^- , F^- and O^- , with overlapping work on only H^- . The magnitude of electron impact detachment cross sections scale inversely with the electron affinity. H^- (electron affinity of 0.75 eV) has a peak cross

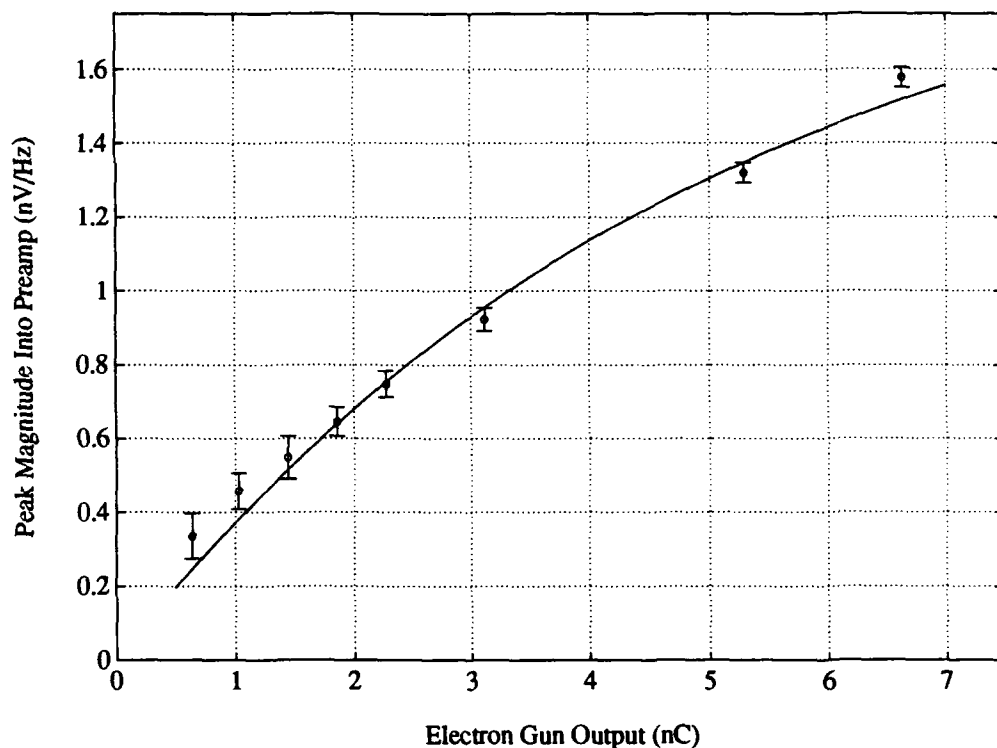


Figure 30. I^- Peak Magnitude vs Electron Beam Output

section of $4 \times 10^{-15} \text{ cm}^2$ at 13.8 eV [135:1347], while F^- (3.4 eV) has a peak cross section of only $2.74 \times 10^{-16} \text{ cm}^2$ at 68 eV [109:L115]. One would expect the electron impact cross section for I^- to have a peak value of several $\times 10^{-16} \text{ cm}^2$ in the range of 50–60 eV. Detachment at low energy (less than 20 eV) will have much smaller cross sections.

Two issues make electron impact detachment measurements challenging using FTMS. First, negative ions formed by dissociative attachment will have finite (but small) kinetic energy. The cyclotron orbits they assume may place them outside the electron beam. The accuracy of beam overlap is difficult to quantify, but necessary for cross section measurements. Second, the detached electrons will have low energies and remain trapped in the ion cell. If the target gas has a large attachment cross section for thermal electrons, anions will be quickly formed. The evolution of the anion signal with beam time will not reflect the actual detachment rate.

The latter likely accounts for the observations shown in Figure 30. A simple two-step model (attachment and detachment) could not accurately represent the data, as indicated by the solid curve in the figure. Detached electrons are probably reacting with CF_3I to form I^- at the very high rates reported by Alajajian et al. [1]. A test of this hypothesis could be done with another attaching gas; one which does not have the dissociative attachment resonance at ~ 0 eV.

The data in Figure 28 are uncorrected for electron impact detachment. Figure 30 shows the data for long beam times ($Q > 2$ nC) are nearly linear, so the losses to electron impact detachment must be nearly compensated by other effects.

Implications of Ion Production Data

The ion production cross sections permit estimation of the effect of adding CF_3I to a plasma. Assuming a maxwellian velocity distribution for the electrons, the rate constants for electron loss (via attachment) and electron production (via ionization) are shown versus temperature in Figure 31. The attachment cross section was formed by a fit to the data reported here and the data from Alajajian et al. [1], while the ionization cross section was taken to be the data from Figure 24.

The rate constants indicate CF_3I would introduce a net loss for electrons in a discharge which is operating at a temperature of less than 3 eV. Even though CF_3I is an considered an attaching species, addition to a hot discharge would result in a net increase for electrons. Previous experimental work added CF_3I to a N_2 discharge and observed it to become unstable, with a tendency towards constricted arc formation [111].

Summary

Cross sections for negative and positive ion production from electron impact in CF_3I have been measured and reported for the first time in the energy range of several eV to 50 eV. The rate constant for anion production dominates its cation counterpart up to temperatures of a few eV.

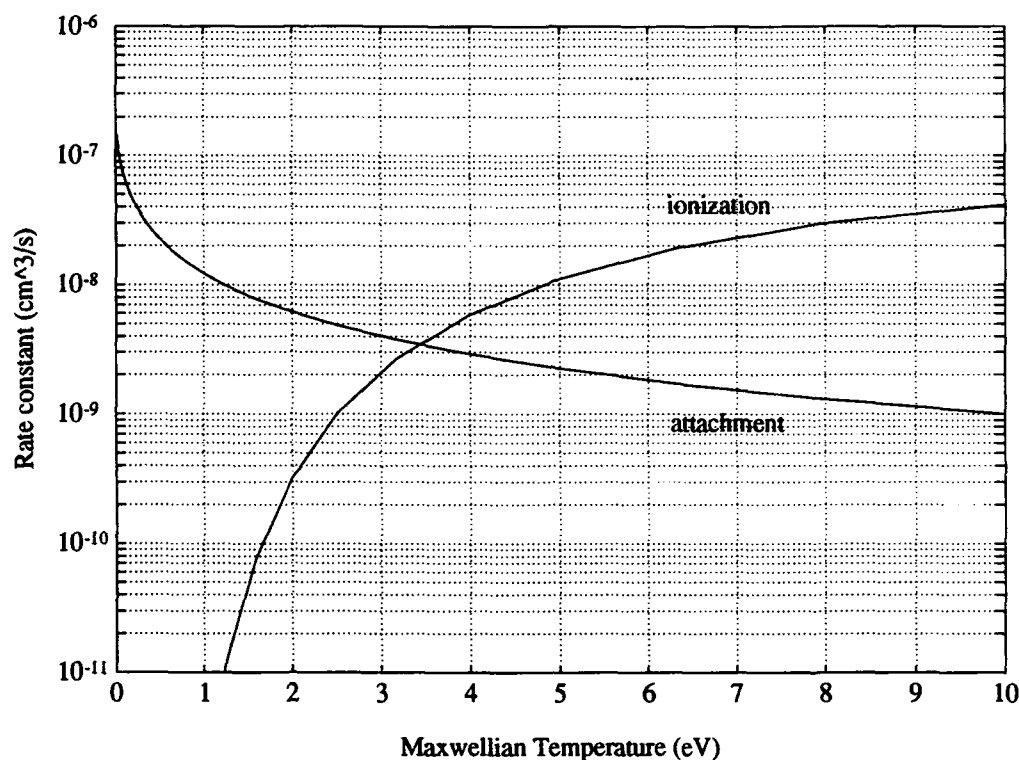


Figure 31. Rate Constants for Ionization and Attachment in CF_3I

I^- was the only negative ion observed and it was easily produced and detected using FTMS. The cross section for I^- production falls sharply with increasing energy to about 6 eV (nominal), but falls slowly for nominal electron energies above 11 eV. For energies within the electron gun rating (above 10 eV), the cross sections are in the range of 10^{-18} — 10^{-19} cm².

Positive ion cross sections showed a total ionization threshold no higher than 10.9 eV and a total maximum cross section no lower than 4.5×10^{-16} cm². The parent ion, CF_3I^+ , has the largest partial ionization cross section over the entire energy range measured. Below ~24 eV, the descending order of the other fragments is CF_3^+ , I^+ , CF_2I^+ , and (tied) CF^+ and CF_2^+ . At energies above 24 eV, the partial cross section for I^+ exceeds that of CF_3^+ and even approaches the cross section for the parent ion.

IV. Ion Kinetics in Trifluoromethyl Iodide

Purpose

The preceding chapter examined the formation of positive and negative ions by electron impact in CF_3I . This chapter looks at how the ions react in the time between formation and the rf excitation (*i.e.*, detection). The primary purpose, in support of the detachment experiments, is to determine whether I^- suffers from inelastic reactions other than detachment—particularly chemical reactions which form new anions—at near-thermal energies.

Since there have been several previous reports using well established techniques on positive ion kinetics in CF_3I , there was an excellent opportunity to calibrate FTMS performance. FTMS proved to be a powerful tool for examining ion kinetics; previous results are a subset of the data presented here.

This chapter discusses previous kinetics measurements, describes the experimental approach using FTMS, and presents quantitative results. Negative ion chemistry is shown not to be a factor in the detachment measurements presented in Chapter 5. By constructing a simple kinetic model based upon previous work and including a proposed new reaction for the collision induced dissociation of CF_3I^+ , the positive ion kinetics are modelled to reasonable accuracy.

Previous Work

Positive ion kinetics have been examined in several reports, under very diverse pressure conditions. Hsieh et al. [59] used TOF and ICR mass spectrometry to examine ion-molecule reactions. The TOF mass spectrometer permitted sample pressures as high as 0.5 torr [59:114], which required the electron gun to be run at 100 eV. As one might expect, reactions to form clusters like I_2^+ , $CF_3I_2^+$, and $(CF_3I)_2^+$ occurred. They also measured rate constants using ICR, which requires operation at low pressures where termolecular reactions are unlikely. The ICR electron beam energy was 25 eV. A summary of the reactions and rates proposed by Hsieh et al. [59:Table 2] is shown in Table 7. They claim Reactions (1) and (5) are very endothermic and Reaction (3) is slightly endothermic, the

Table 7. Ion Molecule Reactions in CF_3I (from Hsieh et al.)

Reaction	Rate Constant ($\times 10^{-10}$ cm ³ /s)	Method
(1) $CF_3^+ + CF_3I \rightarrow CF_3I^+ + CF_3$	0.8	ICR
(2) $CF_3^+ + CF_3I \rightarrow CF_2I^+ + CF_4$	1.68	ICR, TOF
(3) $I^+ + CF_3I \rightarrow CF_3I^+ + I$	2.06	ICR
(4) $I^+ + CF_3I \rightarrow I_2^+ + CF_3$	0.79	TOF
(5) $CF_3I^+ + CF_3I \rightarrow CF_3^+ + I + CF_3I$	1.20	TOF, ICR
(6) $CF_3I^+ + CF_3I \rightarrow CF_3I_2^+ + CF_3$	0.03	TOF
(7) $CF_3I^+ + CF_3I \rightarrow (CF_3I)_2^+$	0.22	TOF

forward reaction rates provide evidence of excited states in CF_3^+ , I^+ and CF_3I^+ . No decay of CF_2I^+ was observed.

Berman et al. [9] also used ICR mass spectrometry to examine ion kinetics. They used a 70 eV electron beam to ionize CF_3I at pressures of $0.5\text{--}1.0 \times 10^{-7}$ torr. Only bimolecular reactions were observed. As seen in Figure 32 (reprinted from [9:Fig 1]), they saw no collision induced dissociation of CF_3I^+ . Therefore, loss mechanisms for CF_3I^+ were omitted from their kinetic model. Berman et al. found their data was explained by Reactions (2) and (3) proposed by Hsieh et al. and one additional reaction for the loss of I^+ , as shown in Table 8. Berman et al. dispute [9:Table 1] the thermochemistry data used

Table 8. Ion Molecule Reactions in CF_3I (from Berman et al.)

Reaction	Rate Constant ($\times 10^{-10}$ cm ³ /s)
(a) $I^+ + CF_3I \rightarrow CF_3^+ + I_2$	3.5 ± 0.7
(b) $I^+ + CF_3I \rightarrow CF_3I^+ + I$	3.9 ± 0.8
(c) $CF_3^+ + CF_3I \rightarrow CF_2I^+ + CF_4$	4.8 ± 1.0

by Hsieh et al. by claiming all three reactions, (a)–(c), are exothermic.

Recently, Morris et al. [98, 99] reported on I^+ and CF_n^+ chemistry with CF_3I using a variable temperature—selected ion flow tube (VT-SIFT) instrument. CF_n^+ was formed in CF_3Br by 70 eV electrons and I^+ was formed by electron impact on CF_3I . The ions were mass selected prior to injection into the flow tube. Rate constants were computed

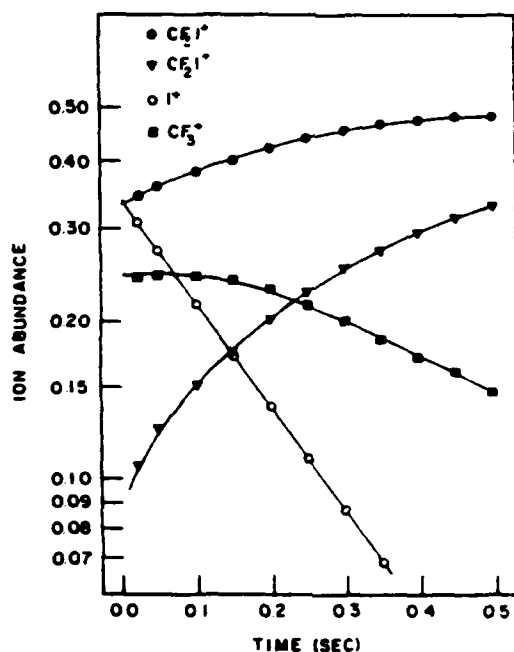


Figure 32. CF_3I Ion Kinetics Using ICR Mass Spectrometry

by fitting the ion signal versus CF_3I pressure (of order 10^{-4} torr). A summary of their observed reactions and rates are shown in Table 9. The data indicate an apparently strong dependence on temperature for Reaction (iv) and a somewhat weaker dependence for Reaction (i). Reaction (iii) is practically temperature independent. Reactions (i), (ii), (iii), (ix) had not been previously reported. Hsieh et al. and Berman et al. were in disagreement over the issue of single or multiple channel losses for CF_3^+ ; the recent data agrees with Berman et al. on a single channel loss only. There is mild disagreement over the precise loss rate; Morris et al. measured a rate constant almost twice as high as Berman et al., although the rate constants agree if a high temperature (496 K) is assumed for Berman et al.'s ICR experiment. The measurement of Reaction (v) showed CF_2I^+ was unreactive, which agreed with both previous works.

No published work (including the papers on dissociative attachment [1, 57]) has discussed negative ion kinetics, although some very recent work by Morris et al. [97] has bounded the rate constant for the reaction of I^- with CF_3I to be less than $2 \times 10^{-12} \text{ cm}^3/\text{s}$.

Table 9. Ion Molecule Reactions in CF_3I (from Morris et al.)

Reaction	Branching Ratio		Total Rate Constant ($\times 10^{-10}$ cm ³ /s)	
	300 K	496 K	300 K	496 K
(i) $CF^+ + CF_3I \rightarrow CF_2I^+ + CF_2$	N/A	N/A	16 ± 4	12.5 ± 3.1
(ii) $CF_2^+ + CF_3I \rightarrow CF_2I^+ + CF_3$	24%	32%	14 ± 3.5	13 ± 3.3
(iii) $CF_2^+ + CF_3I \rightarrow CF_3I^+ + CF_2$	76%	68%		
(iv) $CF_3^+ + CF_3I \rightarrow CF_2I^+ + CF_4$	N/A	N/A	8.7 ± 2.2	4.3 ± 1.1
(v) $CF_2I^+ + CF_3I \rightarrow (?)$	(?)	—	≤ 0.02	—
(vi) $I^+ + CF_3I \rightarrow CF_3^+ + I_2$	63%	—	8.7 ± 2.2	—
(vii) $I^+ + CF_3I \rightarrow CF_3I^+ + I$	26%	—		
(viii) $I^+ + CF_3I \rightarrow I_2^+ + CF_3$	6%	—		
(ix) $I^+ + CF_3I \rightarrow CF_2I^+ + IF$	5%	—		

Experimental Details

Ion kinetics measurements are different from ionization cross section measurements in that the primary variable is the delay time between ion formation and ion detection rather than the electron energy. The delay time (specified as the time between the electron beam termination and the rf excitation trigger) ranged from 4–2000 ms.

The ion kinetic experiments were performed with undiluted CF_3I . The rf excitation for all cases was the wideband SWIFT discussed earlier, clocked out of the AFG at a 10 MHz Nyquist frequency. The electron energy was 15 eV for most experiments, although positive ion data was also collected at 10 eV and 40 eV. The electron beam time was 100 ms (at about 35 nA) for the negative ion measurements and typically 2 ms (at a wide range of currents) for the positive ion measurements.

The ion signal was acquired using a LeCroy 9410 oscilloscope (negative ions) or a LeCroy 9450 oscilloscope (positive ions). Both scopes have an 8-bit ADC which was triggered 200 μ s after the rf excitation was complete. As with the production cross section measurements in the preceding chapter, a total of 10,000 data points were sampled with a Nyquist frequency of 5 MHz. The number of averaged samples varied from 100–300. The actual number and any other information relevant to the specific experiment is detailed below.

Positive Ion Kinetics.

Positive ion kinetics at near-thermal energies were examined using FTMS. The term 'near-thermal' is employed because, although the ions are formed at thermal energies, the trap potential can add up to 0.67 eV (+1 V trap) or 1.33 eV (+2 V trap) of translational energy in the axial mode.

Kinetics experiments were performed with different pressures, trapping potentials, and electron impact energies. A summary of the parameters is shown in Table 10. The energy is the nominal beam energy (uncorrected for the trap potential), V_T is the trap

Table 10. Experimental Parameters for Positive Ion Kinetics Measurements

Exprmnt	Energy (eV)	V_T (V)	Pressure (ntorr)	$n_a (\times 10^{10} \text{ cm}^{-3})$
(a)	10	1	660 ± 126	2.33 ± 0.44
(b)	15	1	780 ± 30	2.76 ± 0.11
(c)	15	2	760 ± 30	2.69 ± 0.11
(d)	15	2	309 ± 42	1.09 ± 0.15
(e)	40	2	260 ± 14	0.919 ± 0.049

potential and n_a is the neutral gas density computed from the pressure calibration measurement, assuming a gas temperature of 298 K.

Time domain ion signals were zero-filled to a length of 256k, Fourier tranformed, and gain corrected for the preamplifier spectral response. The criteria for selection of a "peak" was somewhat subjective. Trace ions were required to have a recognizable trend (either increasing or decreasing) with respect to delay time. Not having a trend implied an ion was unimportant kinetically. This meant the data generally needed to have a signal-to-noise ratio of at least 2-3 for a minimum of 3-4 delay times to be included. For each experiment, the criteria resulted in a set of ion peak magnitudes versus delay time. Harmonics were observed ($2\omega_c, 3\omega_c$), but not included in the database. An example database, for Experiment (e), is shown in Figure 33 (ions below 1% of the total not depicted). The large variations (for example, see the CF_3I^+ trace for delay times less than 100 ms) are due to fluctuations in pressure ($\sim 10\%$) and electron gun output ($\sim 10\%$); data was not collected sequentially in delay time, so the effect is accentuated. It is interesting

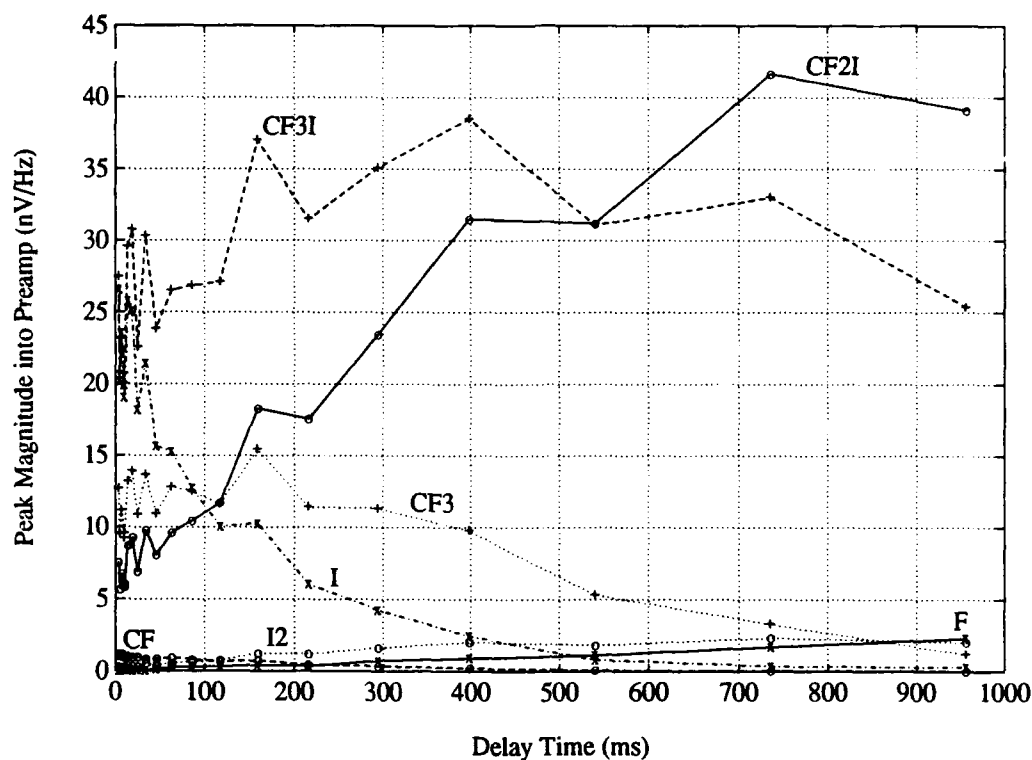


Figure 33. Ion Peak Magnitudes vs Delay Time, Experiment (e)

to note that flowing CF_3I degraded the electron gun output during the course of an experiment, sometimes by as much as 25%.

When corrections are made for the electron gun output and the ion intensities are normalized to the total ion signal, the ion peaks take on the more continuous appearance shown in Figure 34. All kinetics modelling was done with normalized abundances, which is acceptable as long as all ions are detected. The detection range was 16–500 amu.

A summary of observed mass peaks is shown in Table 11. Although Experiments (b),(c),(d) were all with a nominal electron energy of 15 eV, several types of trace ions were only visible in Experiment (d). This was a result of its lower pressure, which permitted a longer ion lifetime (and thus easier identification) of species like CF^+ and CF_2^+ .

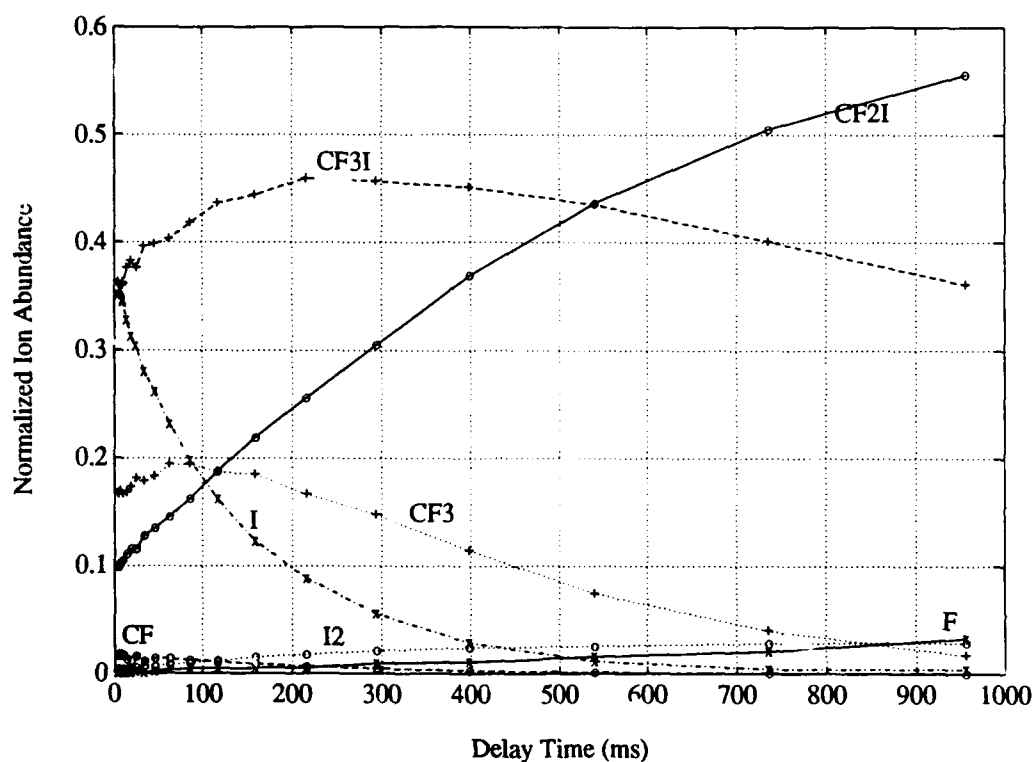


Figure 34. Normalized Ion Peak Magnitudes vs Delay Time, Experiment (e)

Based upon previous work (Tables 7-9), there are three fragment ions which are anticipated to undergo kinetic losses: I^+ , CF^+ , CF_2^+ . For ions that have no production terms, the decay is of the form

$$N(t) = N(0) e^{-n_a \langle \sigma v \rangle t} \quad (11)$$

where n_a is the neutral gas density and $\langle \sigma v \rangle$ is the total observed rate constant for decay. By fitting the experimental data for the three ions to the form $A e^{-t/\tau}$, the decay rate constant can be computed if the CF_3I pressure is known:

$$\langle \sigma v \rangle = \frac{1}{n_a \tau} \quad (12)$$

Table 11. Ions Detected in Ion Kinetics Experiments

Mass (amu)	Cation	Experimental Observation				
		(a)	(b)	(c)	(d)	(e)
17	$OH(?)$					✓
18	H_2O					✓
19	F or H_3O	✓	✓	✓	✓	✓
28	N_2					✓
31	CF				✓	✓
32	O_2					✓
37	$(?)$					✓
39	$F \cdot H_2O(?)$					✓
44	CO_2					✓
50	CF_2				✓	✓
69	CF_3	✓	✓	✓	✓	✓
87	$CF_3 \cdot H_2O(?)$	✓	✓	✓	✓	✓
127	I	✓	✓	✓	✓	✓
177	CF_2I	✓	✓	✓	✓	✓
196	CF_3I	✓	✓	✓	✓	✓
254	I_2				✓	✓

The data was fit by minimizing χ^2 (for the definition and implications of χ^2 , see [10:67-72, 255-260]). This was done using MATLAB's implementation of the Nelder-Mead simplex algorithm, which is a direct search method for finding the minimum value of a function [90:3-80]. The standard for a well-understood data set is to have a reduced chi-square (χ^2_ν) of 1.0. A large χ^2_ν implies poor measurements, incorrect error bars or an incorrect hypothesis of the functional form [10:69].

Two examples of experimental data are shown in Figure 35. The error bars are relative errors. The best fit, with χ^2_ν of 0.4 and 1.0, respectively, is shown as the solid line. The resulting decay constants (τ) were 250 ± 50 ms and 127 ± 5 ms. The variance of the fit parameters (σ_A , σ_τ) is determined by a monte carlo technique in which each data point is varied by a random number generator, constrained to a normal distribution by MATLAB, in accordance with the magnitude of the data point's error bar. The fit is then performed. The process is repeated N times (typically $N = 100$) and a distribution of A 's and τ 's is generated. The monte carlo runs corresponding to the results of Figure 35 are displayed in Figure 36. The standard deviation of the histograms is the reported error.

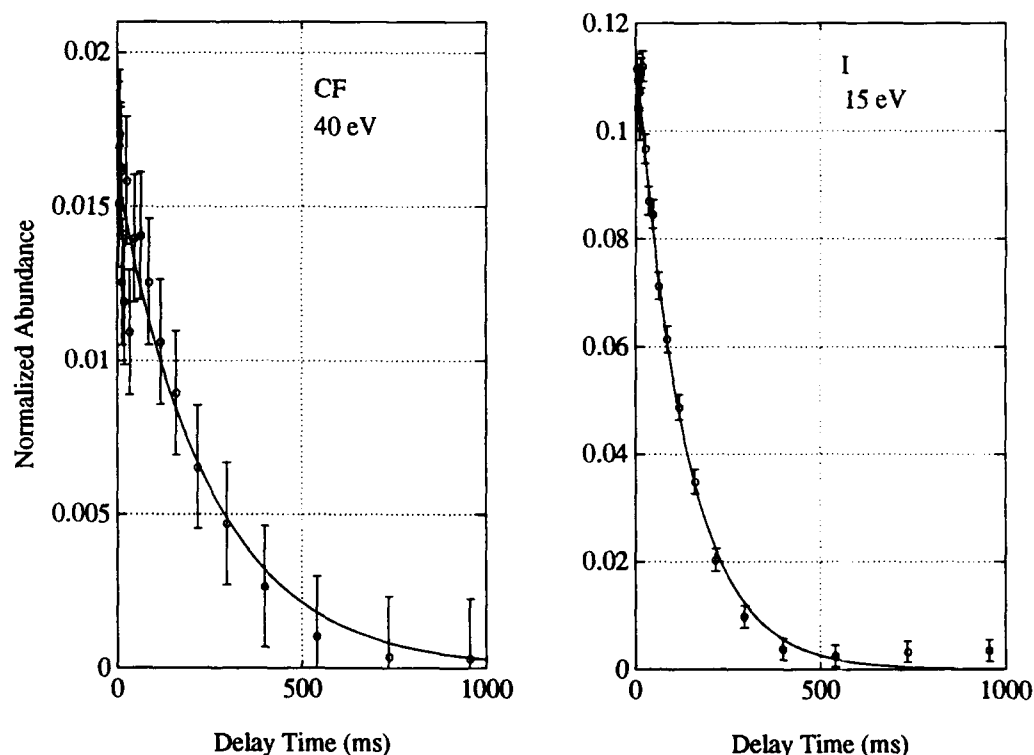


Figure 35. Ion Peak Magnitudes vs Delay Time

Occasionally, the distribution was somewhat skew; no compensation was made for the shape of the histogram to maintain the 67% confidence level associated with one standard deviation in a normal distribution with the error bars reported here.

A summary of the total decay rate constants for the three species which undergo losses only is shown in Table 12. The rate constant for I^+ is remarkably consistent, regardless of the variation of pressure, trapping potential or electron energy. For I^+ , Berman et al. reported $(7.4 \pm 1.5) \times 10^{-10} \text{ cm}^3/\text{s}$ (see Table 8) and Morris et al. reported $(8.7 \pm 2.2) \times 10^{-10} \text{ cm}^3/\text{s}$ (see Table 9), so one concludes the overall decay of I^+ is indeed well characterized.

The same cannot be said for CF^+ and CF_2^+ . As was seen in Table 9, the rate constants for both were previously reported to be comparable and in the range $12\text{--}16 \times 10^{-10} \text{ cm}^3/\text{s}$. The CF_2^+ rate constant measured here is consistent to within error bars;

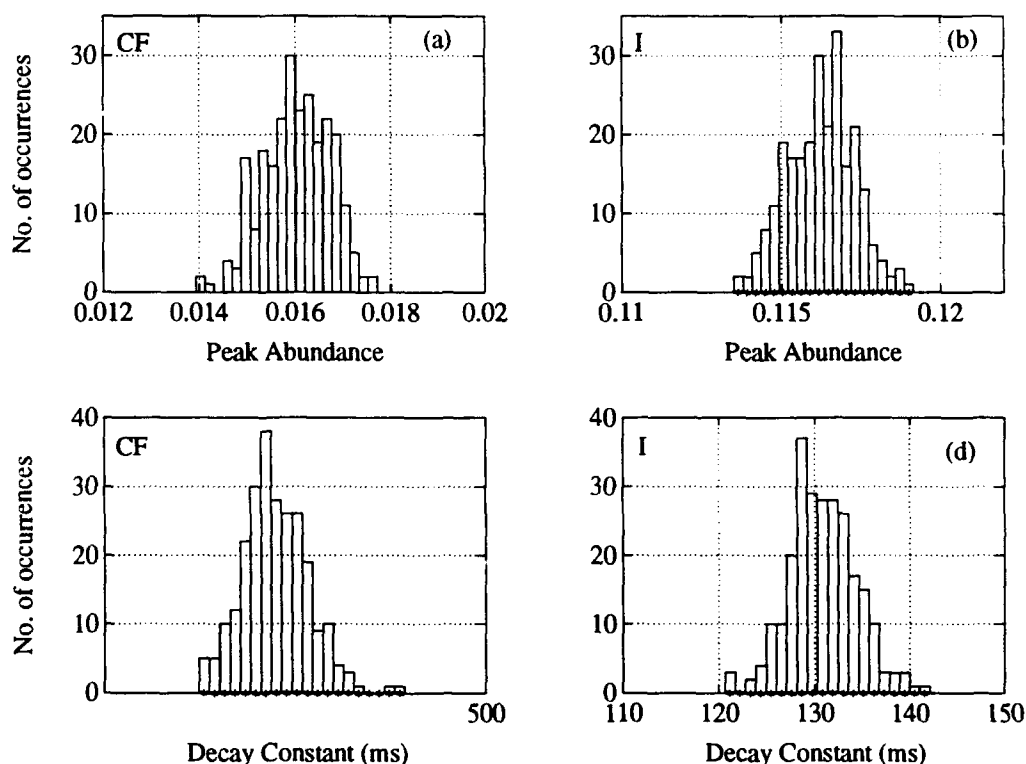


Figure 36. Histograms of Fitting Parameters from Monte Carlo Runs

the CF^+ rate constant for Experiment (e) (40 eV electrons) is about a factor of 3 lower. A possible explanation may be a "hot" distribution of CF^+ in the FTMS measurements. It is well known that electron impact is a good source of vibrationally excited molecules (for example, [65]). Additionally, the trapping well adds kinetic energy to the CF^+ distribution, since the ions are formed with equal probability along the z-axis. Morris et al. reported that the rate constant for CF^+ is particularly temperature sensitive, whereas the one for CF_2^+ is relatively temperature independent. For $CF^+ + CF_3I$, they reported the rate constant goes as $T^{-1/2}$ [97:2600]. To account for the factor of 3 difference in the measured rate constants, the FTMS data would need an effective temperature of roughly 4000 K, which is plausible.

The remaining ions have more complicated kinetics than simple decay. As can be seen in Figure 34, the four ions with the largest cross sections (CF_3I^+ , I^+ , CF_3^+ , CF_2I^+)

Table 12. Total Decay Rate Constants Determined Using FTMS

Ion	Total Decay Rate Constant ($\times 10^{-10}$ cm ³ /s)				
	(a)	(b)	(c)	(d)	(e)
I^+	8.0 ± 3.6	7.1 ± 1.0	7.2 ± 1.0	7.3 ± 1.2	7.5 ± 0.5
CF^+	—	—	—	5.6 ± 9.7	4.4 ± 1.0
CF_2^+	—	—	—	8.6 ± 7.8	12.4 ± 3.1

dominate the ion kinetics. The approach was to assume that trace ions do not play a role in the kinetics, compute rate coefficients based upon the limited interactions of the four dominant species and then verify the initial assumption was valid.

Simple rate equations were formulated to model the four dominant ions. Several systems were modelled, as shown in Table 13. 'System 1' was proposed by Berman et al.

Table 13. Proposed Kinetic Systems

Designator	Reactions
System 1	$I^+ + CF_3I \xrightarrow{k_1} CF_3I^+ + I$ $I^+ + CF_3I \xrightarrow{k_2} CF_3^+ + I_2$ $CF_3^+ + CF_3I \xrightarrow{k_3} CF_2I^+ + CF_4$
System 2	System 1 plus $CF_3I^+ + CF_3I \xrightarrow{k_4} CF_3^+ + CF_3I + I$
System 3	System 1 plus $CF_3I^+ + CF_3I \xrightarrow{k_4} CF_2I^+ + (CF_4 + I)?$

(Table 8), 'System 2' adds a loss mechanism for CF_3I^+ proposed by Hsieh et al. (Table 7) and 'System 3' proposes a new loss mechanism for CF_3I^+ . The differential equations for each system were solved using the Mathematica [142] software package to provide analytic forms for the ion time dependence. The normalized ion abundance data was fit to the analytic forms, once again using MATLAB's implementation of the Nelder-Meade simplex algorithm to minimize the *total* χ^2 . The variance (error bars) of the computed rate constants were computed using the monte carlo technique discussed above.

Figure 37 shows the normalized ion abundances versus delay time for Experiments (a) through (d). Experiment (e) was displayed earlier in Figure 34. It is obvious for all

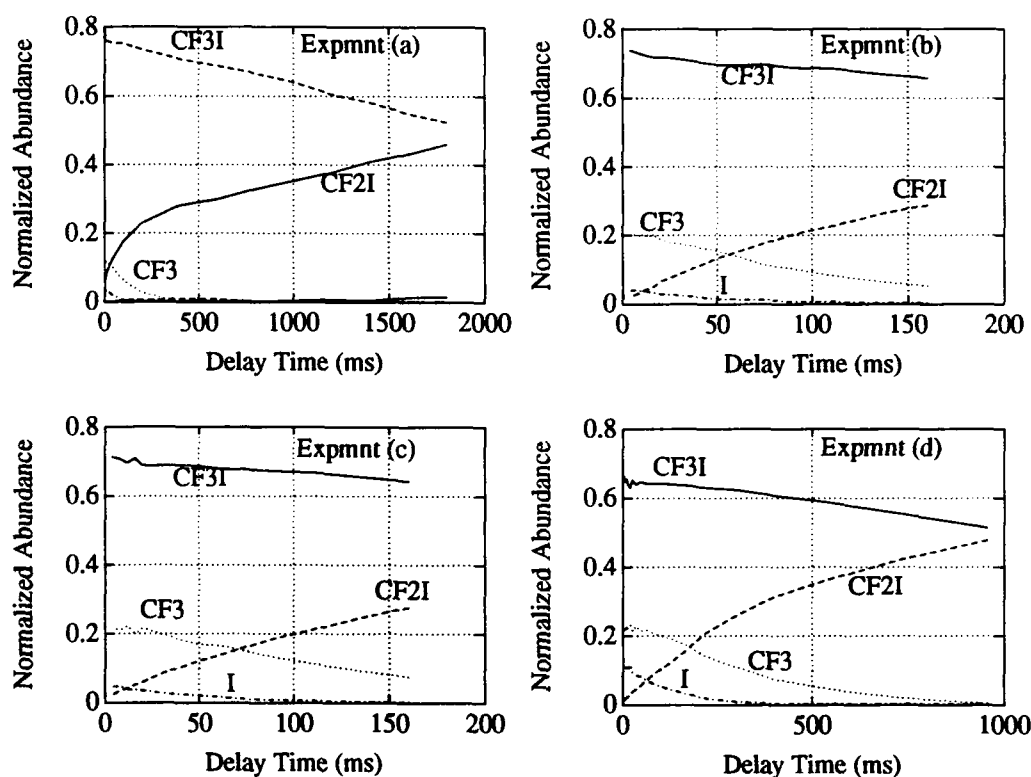


Figure 37. Normalized Abundances vs Delay Time for Experiments (a)–(d)

five experiments that there is a relative loss of CF_3I^+ . Both the figures and the fitting algorithm confirm System 1 has a low probability of accurately modelling the ion kinetics—it has no loss term for CF_3I^+ . Yet, when constrained to a similar parameter space as used by Berman et al., the data agrees with that presented in Table 8. Berman et al. used delay times up to 500 ms at pressures of 50–100 ntorr. Since Experiment (e) was run at about 0.25 μ torr, a maximum delay of 100–200 ms would constrain the FTMS data to the same pressure-time product. Examining the early portion of Figure 34 shows a close similarity to Figure 32. Fitting only the early portion of Experiment (e) (the first 200 ms) to System 1 results in the same rate constants (within error bars) achieved by Berman et al. Therefore, either Berman et al. did not run long enough delays to pick up the CF_3I^+ collision induced dissociation (CID), which they specifically stated they looked for, or (more likely) the trapping potential well contributes to (or causes) the CID of CF_3^+ .

With System 1 eliminated as best describing the experimental observations, fitting was performed for System 2 and 3. An example of the best fit for each is shown in Figure 38. Although the difference between the two systems appears subtle, χ^2_ν varied from 1.5 for

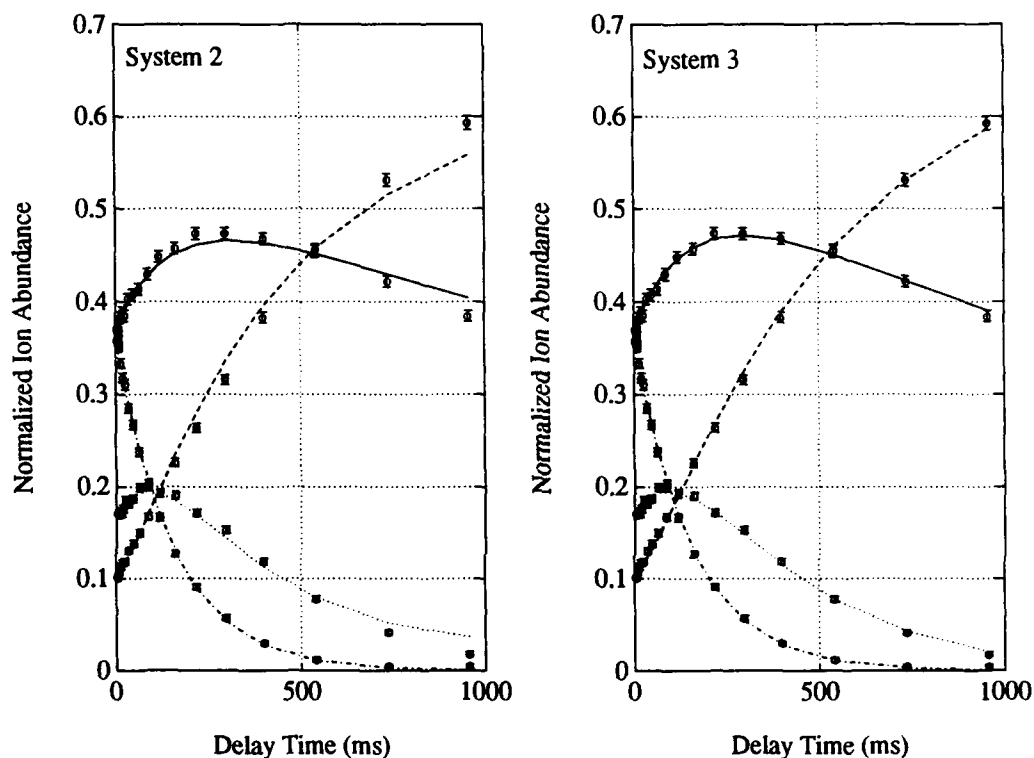


Figure 38. Comparison of the Best Fit of System 2 and 3 Applied to Experiment (e)

System 3 to 3.3 for System 2. Both the figure and the fits confirm System 3 has a higher probability of accurately representing the ion kinetics than System 2. In fact, this was true for all five experiments.

In light of the data, there is a more basic argument in favor of System 3. For most of the experiments, the CF_3^+ concentration is depleted for the longer delay times. If steady state conditions are assumed (with respect to CF_3^+), the following must be satisfied:

$$\text{System 2: } k_4[CF_3I^+] = k_3[CF_3^+] - k_2[I^+]$$

$$\text{System 3: } 0 = k_3[CF_3^+] - k_2[I^+]$$

Since the concentrations of CF_3^+ and I^+ (represented in brackets) are zero or nearly zero for long delay times, only the System 3 steady state criterion is met.

For all five experiments, System 3 produced the best fit in the form of the minimum χ^2 . Results for that system are summarized in Table 14. The negative rate constants indicated for k_1 are simply a mathematical result—at 15 eV there is a small concentration

Table 14. Summary of Primary Rate Constants in CF_3I Kinetics

Experiment	Energy (eV)	Rate Constant ($\times 10^{-10}$ cm ³ /s)				
		k_1	k_2	$k_1 + k_2$	k_3	k_4
(a)	10	0.038 ± 3.1	9.4 ± 5.6	9.4 ± 8.7	4.4 ± 1.3	0.086 ± 0.019
(b)	15	-10 ± 4.9	18 ± 5.1	7.3 ± 10	4.6 ± 0.6	0.078 ± 0.072
(c)	15	-3.4 ± 5.1	11 ± 5.0	7.4 ± 10	3.5 ± 0.6	0.14 ± 0.11
(d)	15	0.44 ± 0.67	6.4 ± 1.5	6.8 ± 2.2	3.5 ± 0.6	0.22 ± 0.047
(e)	40	3.5 ± 0.6	3.6 ± 0.5	7.1 ± 1.1	3.7 ± 0.4	0.41 ± 0.06

of I^+ and modelling the decay was made more difficult by the high pressure used for Experiments (b) and (c).

Table 14 displays several key results. There is some indication within k_3 that the trap potential affects the "effective" temperature of the ion distribution. Experiments (a) and (b), which were obtained with a +1 V trap, have a CF_3^+ reaction rate constant 33% higher than Experiments (c), (d), (e), which had a +2 V trap. These results are consistent with the temperature dependence for the reaction of CF_3^+ (which k_3 represents) reported by Morris et al.

More importantly, both k_4 and k_1 show a sharp increase with electron impact energy. Since the CID of CF_3I^+ (represented by k_4) is endothermic, this observation is taken to indicate the existence of excited states of CF_3I^+ . Carrying this argument to k_1 , it is implied that excited states of I^+ preferentially undergo charge transfer (represented by k_1) rather than reaction to form CF_3^+ . Interestingly, although k_1 increases with increasing electron energy, k_2 decreases so as to keep the overall decay of I^+ independent of electron energy! The dependence of some reaction rates on the formation energy says caution must be exercised when applying rate constants determined from high energy electron impact (70–100 eV) to actual plasmas (which are generally much colder).

With the dominant ion analysis complete, the System 3 fits were performed on the four ions normalized to the total ion signal, which included the trace ions. The rate constants were consistent within error bars of those shown in Table 14, verifying the original assumption to ignore trace ions was valid.

Negative Ion Kinetics.

Chapter 3 showed I^- was the only anion detectable by electron impact. Kinetic experiments were performed to see if I^- reacts with CF_3I to form other anions. Iodine has only one stable isotope, so resonant charge transfer ($I^- + CF_3I \rightarrow (CF_3I_2)^* \rightarrow CF_3I + I^-$) could not be discerned. This process was bounded by additional measurements, which are reported in Chapter 5.

Reactions of I^- with CF_3I at pressures in the 10^{-7} Torr range were examined over reaction times of 4–878 ms. Ion signals were processed in the same manner as discussed previously for the positive ion chemistry. No new anions were detected. As seen in Figure 39, the I^- signal shows no decay. Instead, it shows the z-axis relaxation typical of unreactive ions [116] that was discussed in the previous chapter. Simulation predicts the ion signal should increase by over 30%; at the longest delay times the signal had increased over 20% and was still rising. So it is concluded that the I^- is unreactive in CF_3I . This is in agreement with very recent work [97], which measured no reactions other than a very weak clustering reaction (formation of $CF_3I \cdot I^-$) with a rate constant no greater than $5 \times 10^{-12} \text{ cm}^3/\text{s}$.

Conclusions

Positive ion kinetics at near-thermal energies were studied using FTMS. Four ions (CF_3I^+ , CF_2I^+ , I^+ and CF_3^+) dominate the ion kinetics. Based upon previous work, several kinetic models were constructed; the model which most accurately described the data included the reactions proposed by Berman et al. [9] and a new reaction for the collision induced dissociation of CF_3I^+ .

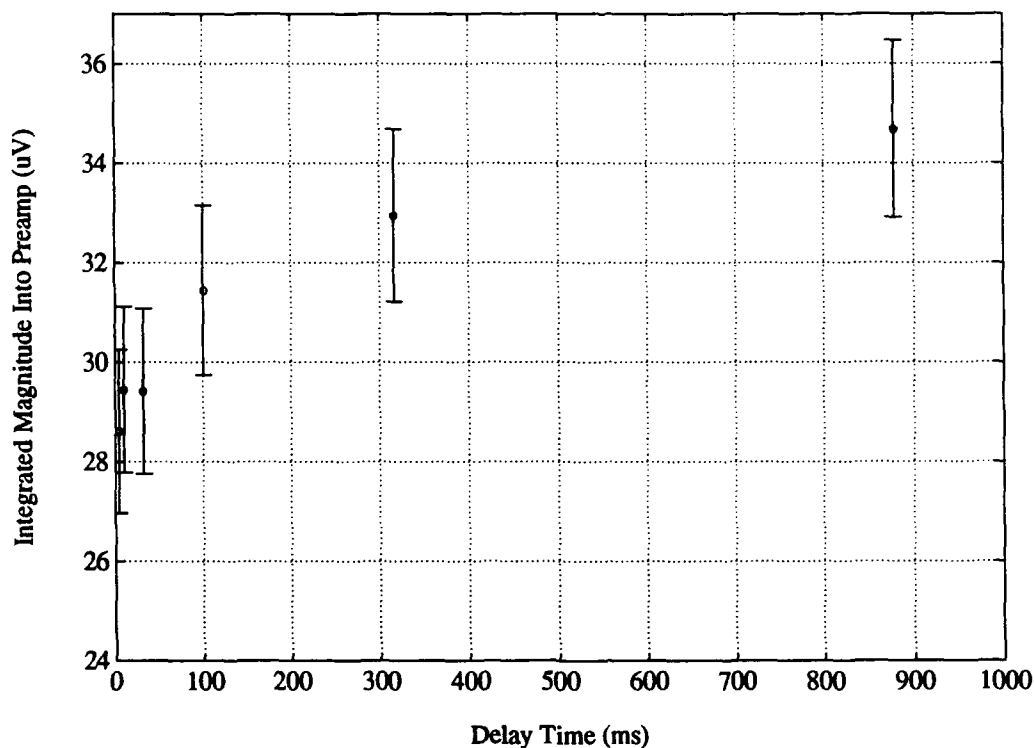


Figure 39. I^- Signal vs Delay Time Showing the Unreactive Negative Ion Kinetics

Several fragment ions (I^+ , CF^+ , CF_2^+) undergo simple decay (no kinetic production) after formation. The decay of I^+ was observed to be independent of the electron energy of formation and had a rate constant ($7.4 \pm 0.8 \times 10^{-10} \text{ cm}^3/\text{s}$) in excellent agreement with previously published results. The rate constant for CF_2^+ ($12.4 \pm 3.1 \times 10^{-10} \text{ cm}^3/\text{s}$ at 40 eV) also agreed with previous results. CF^+ had a rate constant ($4.4 \pm 1.0 \times 10^{-10} \text{ cm}^3/\text{s}$ at 40 eV) lower than previous results, but consistent if the trap potential well increases the effective temperature of CF^+ to 4000 K. There was indication the trap potential affected other reaction rates.

Reaction channels within I^+ and for the collision induced dissociation (CID) of CF_3I^+ had rate constants which were a function of the electron energy of formation. At low impact energies (10, 15 eV) the chemical reaction of I^+ with CF_3I to form CF_3^+ was the only channel observed. At higher impact energy (40 eV), charge trans-

fer ($I^+ + CF_3I \rightarrow I + CF_3I^+$) was equally probable as the chemical reaction. The CID of CF_3I^+ grew with electron energy. Both observations are interpreted as indicating the role of excited states in the ion kinetics. These results emphasize that caution should be applied when using rate constants determined from high energy electron impact (70–100 eV) to analyze low energy plasmas.

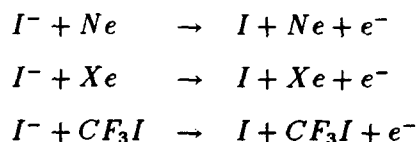
I^- was found to be unreactive with CF_3I at near-thermal energies, in agreement with very recent work [97].

V. Collisional Detachment

Overview

Previous chapters have presented how an ion responds to an rf excitation in an FTMS ion trap, showed examples of the efficiency of ion formation and detection as a function of electron impact energy, and measured ion-neutral reactions which occur in the time between formation and detection at near-thermal energies. This chapter extends that work to examine how negative ions react when they are given high translational energies.

The focus of this research was to make measurements of collisional detachment of the following systems:



The primary objective was to assess whether FTMS could be used to make such measurements. It could, with the advantage of also being able to estimate the competition between elastic and inelastic (detachment) collisions. But the competition made the detachment threshold difficult to resolve.

This chapter explains the experimental method and analysis technique for using FTMS to make inelastic measurements. It shows the total collision rate is straightforward to measure and, by estimating the contribution of elastic scattering, bounds on the detachment cross section can be established. These bounds are compared with published results and the implications are discussed.

Experimental Approach

Detachment experiments were performed with target gases of *Ne*, *Xe* and *CF₃I*. The neon was procured from Matheson Gas Products at grade 5 (99.999%) research purity; the *Xe* and *CF₃I* vendors and purity were discussed in Chapter 3. The *Ne* and *Xe* were loaded at separate times in the lower manifold and undiluted *CF₃I* was placed in the upper manifold. The variable leak valves were used to flow a small quantity of *CF₃I*

(steady-state pressures of order 10^{-8} Torr) and a large quantity of target gas (roughly 0.5–20 μ Torr).

I^- was formed by low energy electron attachment to the "trace" CF_3I . The electron gun was run well below its energy rating (at an uncalibrated energy of several eV) for 60–105 ms. The low beam energy ensured a lack of trapped secondary electrons from ionization of the target gas. Even with very low (\sim nA) electron beam current, care had to be taken to avoid space charge issues because of the tremendous low energy attachment cross section.

Chapter 4 presented evidence that, at near-thermal energies, I^- is unreactive kinetically in CF_3I . I^- is also unreactive in the rare gases Ne and Xe . Therefore, a long delay (240 ms) between ion formation and rf excitation was permissible. High pressures (by FTMS standards) were employed, so the long delay guaranteed the iodine anions were thermalized. The elastic collision frequency of I^- in the three target gases is about 10–300 collisions per second over the pressure range employed, so the anions were assumed to be completely relaxed to the center of the trap.

A standard resonant sinusoidal excitation, 200 μ s long, was used for all detachment experiments. The trap potential was set to -1 volt. Initially, a high trap potential was thought to be preferable because of the enhanced ion compression to the trap center. But experiments with $V_T = -4, -6, -8$ V all had shorter-lived ICR signals when compared with $V_T = -1$ V. This was probably due to the combination of detachment via the axial mode, caused by the translational energy obtained from the high trapping well, and the stronger coupling (with higher trap potentials) between the trapping and excitation fields, which is more sensitive to mechanical misalignments which may exist in the ion cell.

The sinusoidal excitation amplitude was varied to an accuracy of ± 1 mV (using the ± 10 μ V accuracy of the AFG). As discussed in Chapter 2, resonant sinusoidal excitation creates an I^- "beam" of reasonably defined energy. The image current was digitized and recorded using a LeCroy 9450 oscilloscope. Long waveforms of 40,000 or 50,000 data points were collected at a 2 MHz Nyquist frequency (250 ns sampling time per point). Data from each energy (AFG setting) was averaged in the range of 150 to 500 samples.

Measurements were made at 3–4 different pressures, in order to verify no significant pressure effects. Neutral gas pressures were determined by the pulsed valve calibration techniques discussed in Chapter 3 and Appendix A. A summary of the experiments and target pressures is provided in Table 15. Cases where there was an unfavorable ratio of

Table 15. Summary of Pressures in Detachment Measurements

Experiment Designator	Reactants	Pressure (μTorr)	Target: CF_3I Pressure Ratio
1	$I^- + Xe$	(1) 0.201 ± 0.010	~ 38
		(2) 0.594 ± 0.104	"
		(3) 1.6 ± 0.4	"
		(4) 7.9 ± 1.7	"
2	$I^- + Ne$	(1) 0.59 ± 0.03	20
		(2) 1.3 ± 0.3	8
		(3) 3.0 ± 0.7	2
3	$I^- + Ne$	(1) 2.14 ± 0.11	15
		(2) 4.20 ± 0.21	32
		(3) 15.7 ± 0.12	150
4	$I^- + CF_3I$	(1) 5.3 ± 0.2	1
		(2) 12.7 ± 2.5	1
5	$I^- + Xe$	(1) 1.11 ± 0.10	80
		(2) 3.25 ± 0.20	350
		(3) 13.4 ± 0.6	3100

target gas to CF_3I , such as Experiment 2, were analyzed but not included in the data summary because of the probability of contaminated results.

Determination of the Collision Rate Constant

ICR signal decay occurs from three mechanisms: power dissipation in the image current detection circuit, space charge effects, and collisions. Circuit loading has been modelled by Comisarow [23] and the time constant for the FTMS preamplifier is calculated to exceed 100 seconds. As discussed in Chapter 2, space charge effects are minimized by creating less than 10^5 anions. Space charge is eliminated as an experimental variable by maintaining all parameters, except the ion radius, at each pressure. In other words, approximately the same number of ions were created at each pressure. Collisions are left

as the only variable to explain changes in the ion signal decay as the excitation amplitude (ion energy) are varied.

As discussed in Chapter 4, ions which undergo losses have the time dependent form

$$N(t) = N(0) e^{-n_a \langle \sigma_{tot} v \rangle t} \quad (13)$$

where σ_{tot} is the total cross section for interaction(s) which cause the loss of ion signal, n_a is the CF_3I gas density and v is the I^- velocity in the center of mass frame (assumes the I^- kinetic energy \gg neutral gas temperature). If the ion signals can be accurately modelled by an exponential decay, then information about the collision rate constant and the cross section itself can be inferred.

A typical ion signal, clearly exhibiting an exponential decay, is shown in Figure 40. The ion signals were transformed to the frequency domain by a sliding fast-Fourier transform (FFT) algorithm. The peak magnitude for I^- is extracted and stored versus the time midpoint of the sliding transform. Although the time domain and frequency domain are equivalent, transforming to the frequency domain has the advantage of avoiding the broad band noise that is contained in the time domain data. An example of the frequency domain peak magnitude, corresponding to Figure 40, is shown in Figure 41.

The peak magnitude data from the sliding FFT is fit to the form $Ae^{-t/\tau}$ using MATLAB's implementation of the Nelder-Mead simplex algorithm [90:3-80] to minimize χ^2 . For the example in Figure 41, $\chi^2_\nu = 1.1$, indicating a well-understood data set, and $\tau = 2.20 \pm 0.01$ ms. Once the decay constant is obtained, it is related to the total rate constant for collisional loss of signal according to Eq (13):

$$\langle \sigma_{tot} v \rangle = \frac{1}{n_a \tau} \quad (14)$$

The neutral gas pressure is determined by the pulsed valve technique discussed earlier. Given the pressure and the computed decay constant, the total reaction rate constant for ion loss can be determined as a function of the excitation amplitude (ion energy). For the

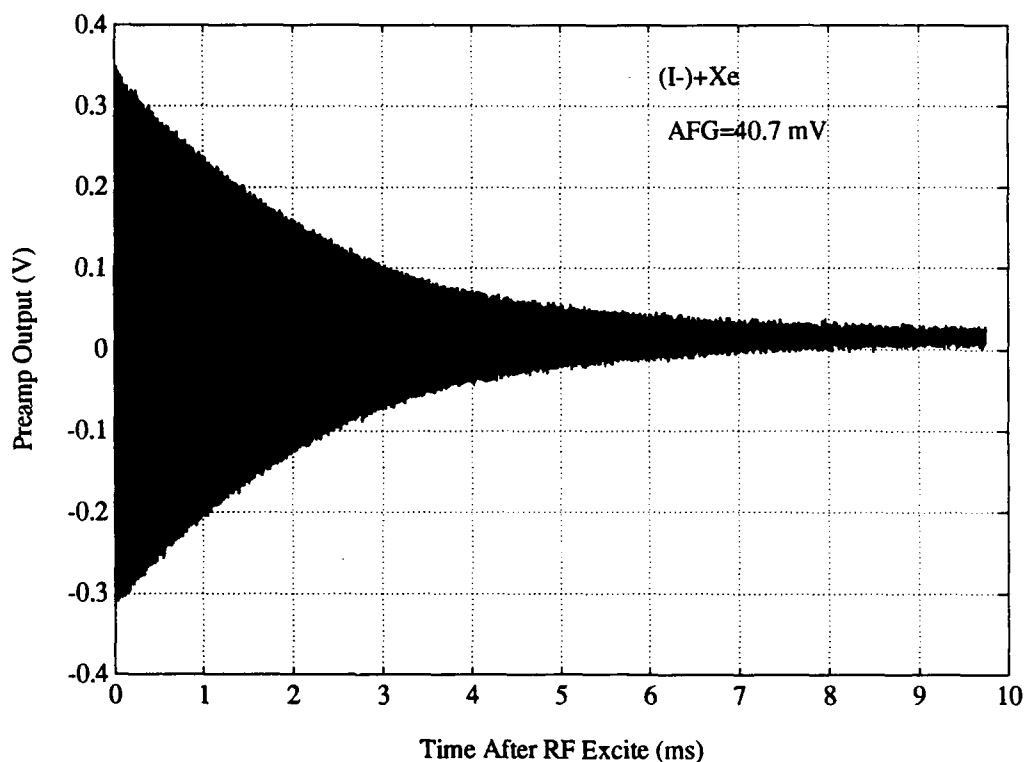


Figure 40. Typical Time Domain Spectra Showing ICR Signal Decay. Displayed are 40,000 data points collected at a 2 MHz Nyquist frequency. The Xe pressure was 13.4 μ Torr.

example shown in the figures, $\langle \sigma_{tot} v \rangle = 9.6 \times 10^{-10} \text{ cm}^3/\text{s}$, at a lab frame energy of 59 eV.

The evolution of the ion signal decay is easily observed as a function of excitation amplitude. Figure 42 shows the peak magnitudes versus the time after excitation for four different AFG settings. The dramatic change in decay constant is apparent. Of course, an increased excitation amplitude means a larger radius, which translates into a larger image current. Thus, the intercept of the decay curve increases with excitation amplitude. Had the electron gun been operating in a stable energy regime ($\geq 8 \text{ eV}$), the intercept would be approximately linear with excitation amplitude.

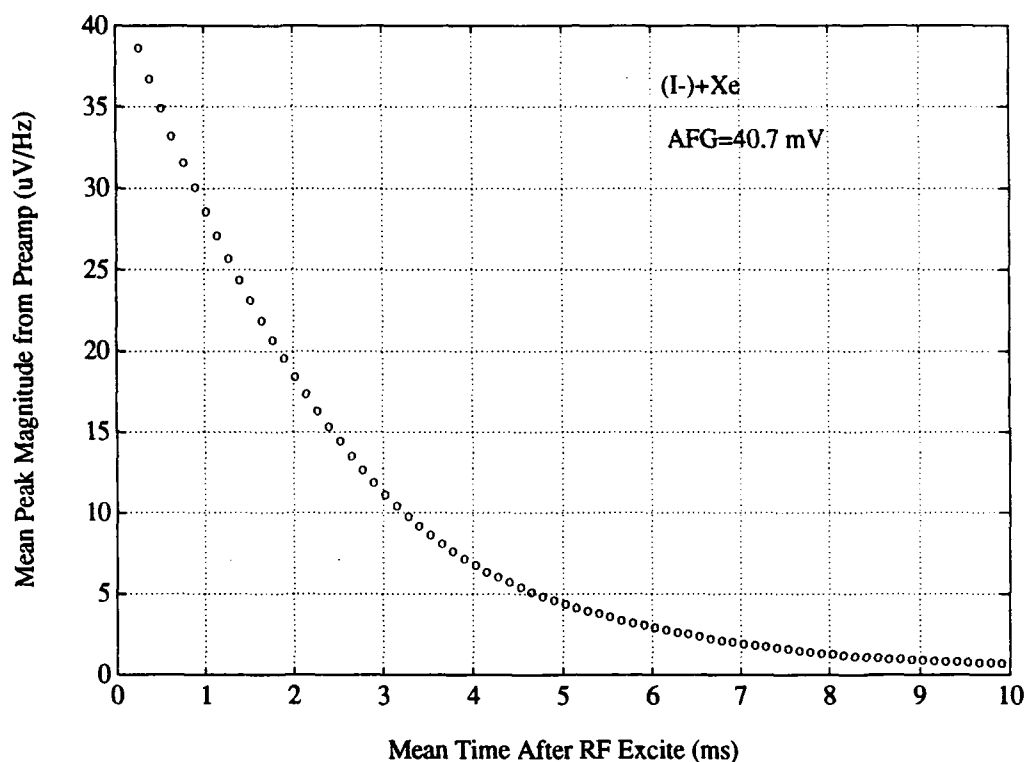


Figure 41. Typical Peak Magnitude from Sliding FFT vs Time. The data results from a sliding FFT on Figure 40 and is plotted vs the mean time after the rf excitation.

Fits were performed on the data gathered in Experiments 1,3,4,5 to compute the decay constants. An example, for $I^- + Ne$ (Experiment 3, pressure (3)), is shown in Figure 43. The error bars associated with τ are quite small, typically in the range 0.5% to 1.4%, and are not shown in the figure. The top portion shows the decay time versus excitation amplitude, in the form of the actual voltage setting on the AFG. As discussed in Chapter 2, ion simulations were run with various AFG settings (see Figure 12). The simulations show the relationship between the most probable kinetic energy and the ion radius (which is nearly linear with AFG setting) has the expected quadratic form:

$$\epsilon = 149.0 \tau^2 \quad (15)$$

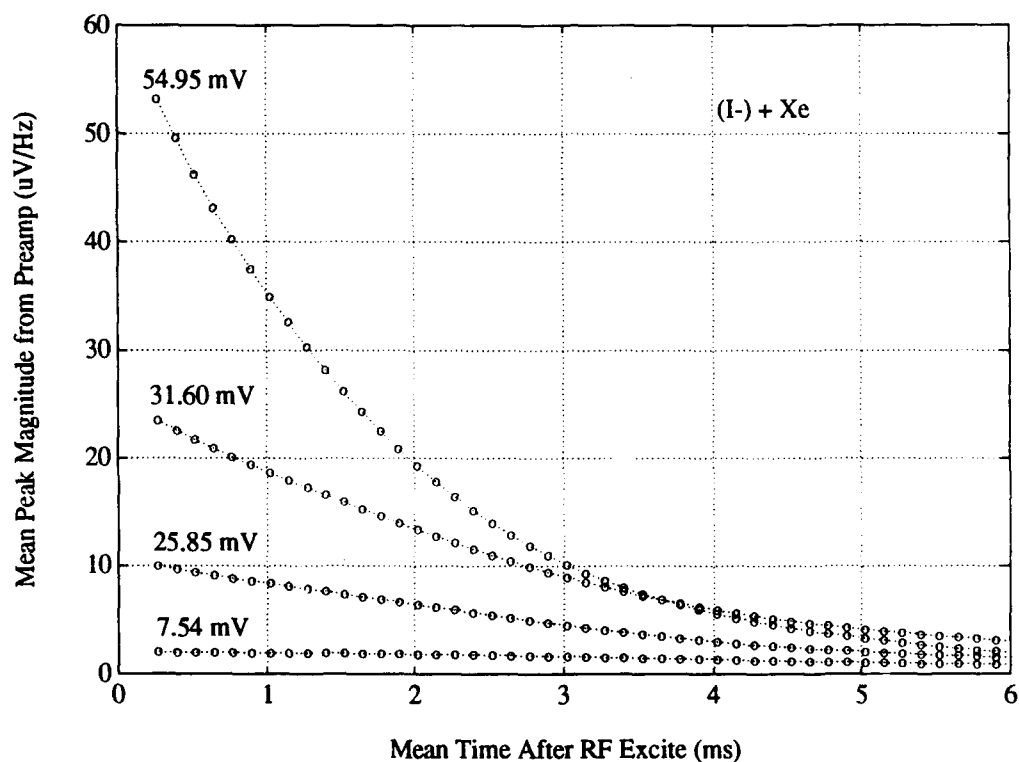


Figure 42. Evolution of Signal Decay With Excitation Amplitude for $I^- + Xe$. The excitation amplitude is annotated above each trace, showing the setting of the AFG.

where ϵ is the laboratory frame kinetic energy (in eV) and r is the final cyclotron radius (in cm). Using the relationships between excitation, ion radius and ion energy, the bottom portion of Figure 43 was created, displaying the most probable kinetic energy in the lab frame as the abscissa. In this format, the decay time is seen to fall quickly with energy until almost 50 eV and then fall much more slowly.

Using Eq (14) and the pressures shown in Table 15, the total collisional decay rate constant was computed and is shown for all cases in Figure 44. The lab frame energy is plotted on the abscissa rather than center of mass frame (C.M. frame) energy to demonstrate there are no systematic effects. Since the intercept and magnitude vary widely between the targets, the observed rates must be real and not systematic. Error bars are

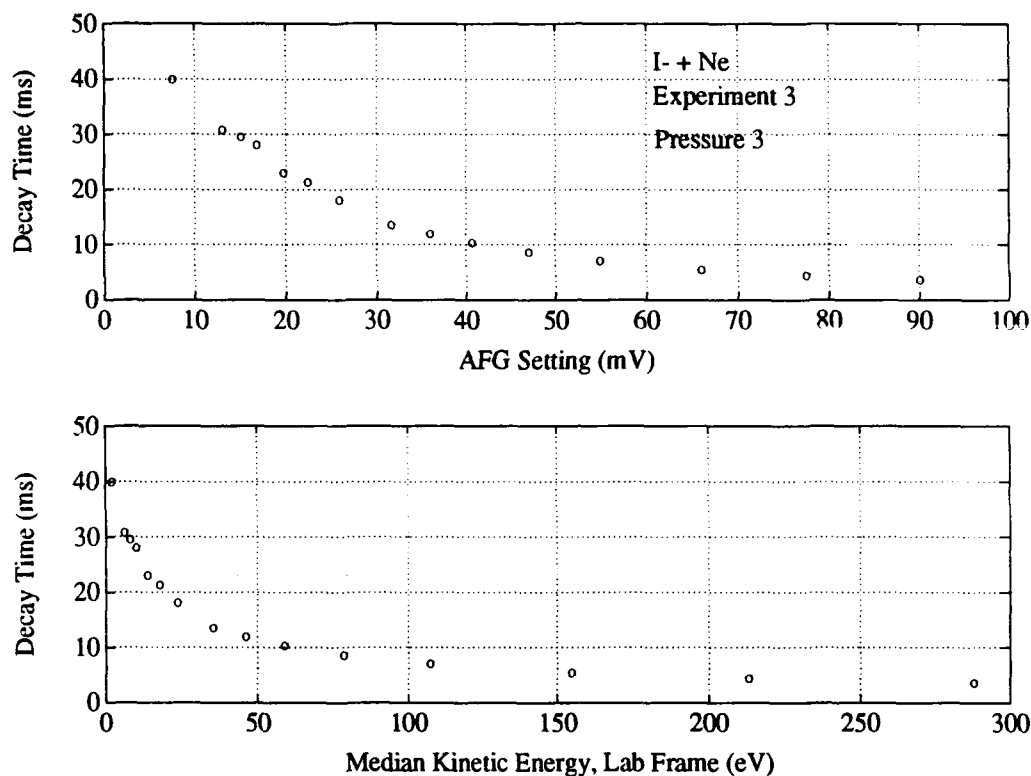


Figure 43. Decay Time vs Excitation Amplitude and Ion Kinetic Energy for $I^- + Ne$. See text for discussion.

not plotted because the plots become too congested, but are quite important in explaining the data. As seen in Table 15, the error in absolute pressure ranges from a few percent to 25%. Since τ is precise, the error in Figure 44 generally varies as the error in pressure, ranging from 5–25%. Although the Ne and Xe data has quite a bit of scatter, each trace is close to being within a standard deviation of the others. There is also a horizontal error bar associated with the I^- energy. As shown in Chapter 2 (see Figure 17), this error is large (up to 50%) at low energy, but small (about 2%) at large energy. The width of the kinetic energy distribution is a direct function of the gas temperature and the rf excitation amplitude (AFG setting), but is not dependent on the type of target gas or its pressure.

The data in Figure 44 was averaged, using a standard weighted mean [10:64–65], and fit to a high order polynomial which accurately represented the data. The results are

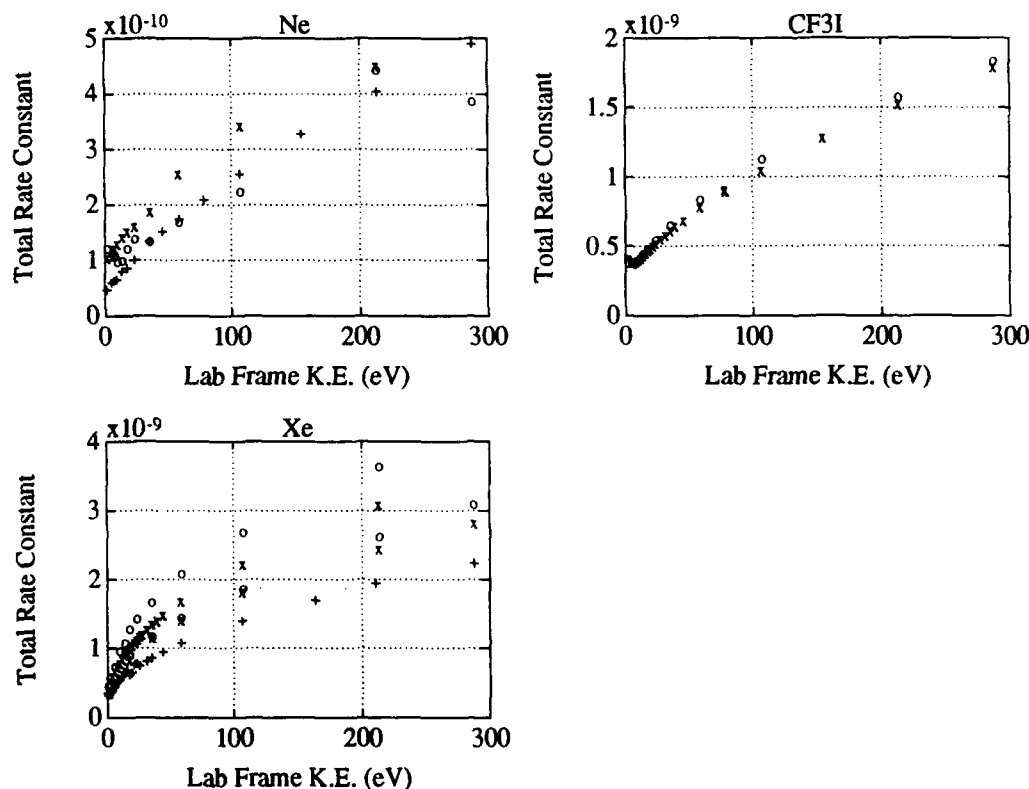


Figure 44. Total Collisional Rate Constants, Derived from I^- Signal Decay. Note the vertical scales are different for each plot.

shown in Figure 45. The error bars for each target gas, which are not displayed in the figure, are $\pm 14\%$ (Xe), $\pm 12.8\%$ (CF₃I) and $\pm 4.6\%$ (Ne).

When a collision occurs between a negative ion and a neutral atom, there are multiple possible outcomes, as summarized in Table 16. Charge transfer and associative detachment (Reactions (d) and (f)) are precluded for the rare gas targets. Landau and Zener [143] have shown the probability of a non-adiabatic transition is low when the relative velocity is small with respect to the separation of energy surfaces. The excitation intensity constrained the I^- to lab frame energies below 300 eV, so excitation and ionization (Reactions (b) and (c)) have a low probability of occurrence. The observed ICR signal decay is primarily caused by momentum transfer and collisional detachment (Reactions (a) and (e)).

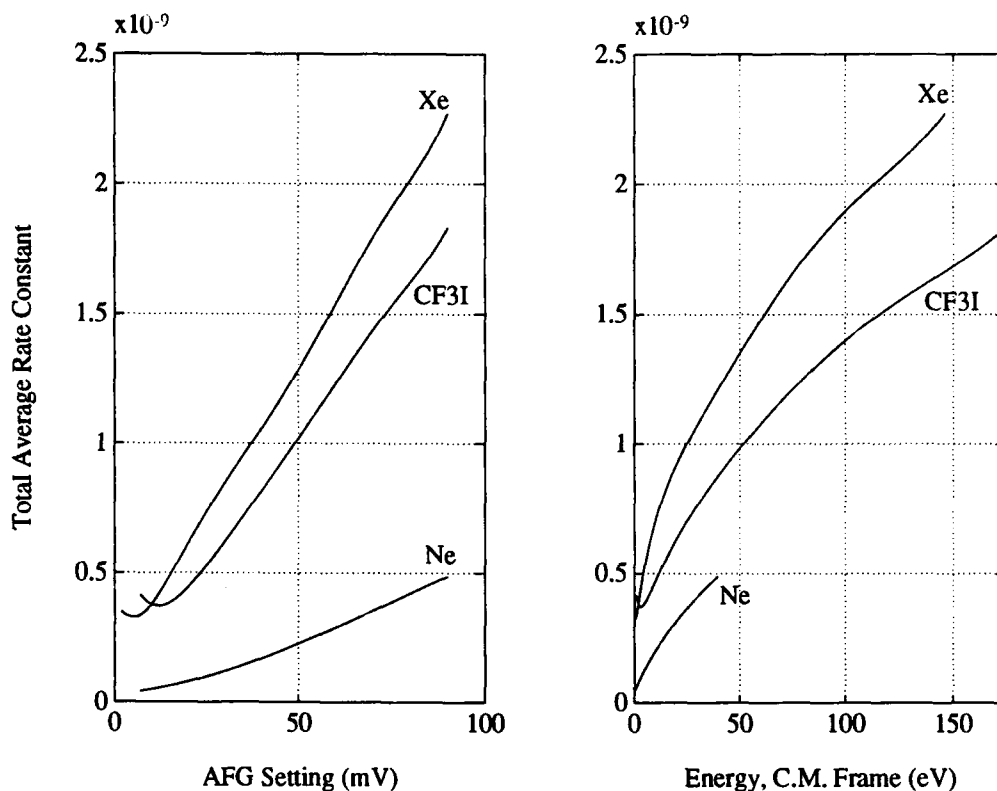


Figure 45. Average Total Collisional Decay Rate Constants vs a) Excitation Amplitude and b) C.M. Frame Energy. The curves represent an absolute upper bound on the collisional detachment rate constants. The 'hook' shape (concave up) at low energy is a result of the energy dependent axial loss of anions from elastic scattering.

Momentum transfer represents the only elastic collision in Table 16. By assuming the contribution of collisional dephasing from momentum transfer collisions is negligible for all energies, an upper bound for the collisional detachment rate constant can be established. This bound is displayed in Figure 45b.

Of course, not every collision undergone by the anions is inelastic. The existence of elastic scattering is seen by examining the observed rate constant at center of mass frame energies below the electron affinity, where collisional detachment is thermodynamically forbidden. Figure 45b shows such rate constants are non-zero and can even be roughly as large as $4 \times 10^{-10} \text{ cm}^3/\text{s}$. The elastic scattering contribution must be estimated and

Table 16. Possible Reactions Involving a Negative Ion

Reaction	Reactants-Products	Description
(a)	$X^- + Y \rightarrow X^- + Y$	Momentum transfer
(b)	$X^- + Y \rightarrow X^- + Y^*$	Excitation
(c)	$X^- + Y \rightarrow X^- + Y^+ + e$	Ionization
(d)	$X^- + Y \rightarrow X + Y^-$	Charge transfer
(e)	$X^- + Y \rightarrow X + Y + e$	Detachment
(f)	$X^- + Y \rightarrow XY + e$	Associative detachment

subtracted from the total collision rate to get a good estimate of the detachment cross section.

Elastic Scattering

For large interaction distances, elastic scattering is known to be well represented by the polarization interaction [29, 53]. Computing the elastic cross section from the $1/R^4$ potential has been performed classically [53] and quantum mechanically [29], with the resulting form

$$\sigma_{elas} \simeq 2.21\pi \sqrt{\frac{\alpha e^2}{\epsilon_{C.M.}}} \quad (16)$$

where α is the polarizability of the target atom, e represents the elementary charge unit and $\epsilon_{C.M.}$ represents the kinetic energy in the center of mass frame. Because the elastic cross section goes as $1/v$, the rate constant is independent of kinetic energy:

$$\langle \sigma v \rangle_{elas} \simeq 2.21\pi \sqrt{\frac{2\alpha e^2}{\mu}} \quad (17)$$

where μ is the reduced mass. Computing this rate for targets of Ne , Xe and CF_3I results in the following Langevin rates:

$$\begin{aligned} Ne: & \quad (5.52 \pm 1.3\%) \times 10^{-10} \text{ cm}^3/\text{s} \\ Xe: & \quad (9.16 \pm 0.65\%) \times 10^{-10} \text{ cm}^3/\text{s} \\ CF_3I: & \quad (1.20 \pm 10\%) \times 10^{-9} \text{ cm}^3/\text{s} \end{aligned}$$

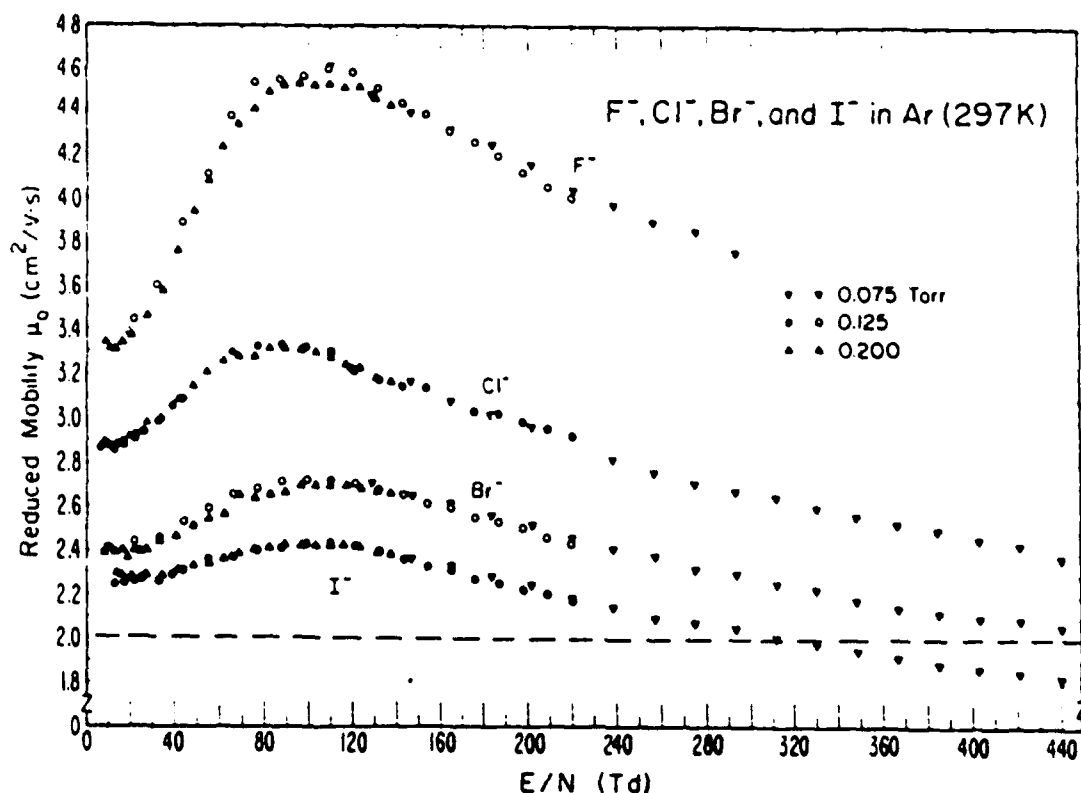


Figure 46. Mobility Measurements of Halogen Anions in Argon. The reduced mobility resulting strictly from the polarization interaction is shown as the horizontal dashed line.

The error bars are a result of the uncertainty in the polarizability (which accounts for the large CF_3I error) and the reduced mass being treated as the weighted average of all stable isotopes.

It is not known how well the Langevin approach (Eqs (16) and (17)) models elastic scattering of I^- with Ne , Xe and CF_3I . Although there have been several experiments which examined differential scattering of I^- , no previous report could be found which measured the total elastic scattering cross section at low energies ($\epsilon_{lab} < 100$ eV) in any of the three gases.

It was thought that mobility measurements might provide insight into the elastic scattering cross section. There have been several measurements of halogen negative ions in rare gases (for example, [33, 34, 92]), but none used Ne or Xe as the buffer gas. An example

mobility measurement, where Ar was the target, is shown in Figure 46 (reproduced from [33:5239]). The zero field value is roughly 10% higher than the rate determined from the polarization interaction. Smirnov [121] has noted, using other anion mobility data, that targets with a large polarizability have low-field mobilities represented by the Langevin rate to within $\simeq 10\%$. The problem with mobility measurements is that they are measured in terms of E/N . To convert E/N to kinetic energy, a form for the elastic cross section must be assumed—yet the energy dependence of the elastic cross section is precisely what is being sought. The problem is non-linear and the solution will likely not have high precision. There is also the possibility the observed decrease in mobility for large E/N is partly due to collisional detachment. Therefore, using mobility data would not provide a significantly more accurate estimate of the elastic cross section than using the Langevin rate.

The elastic cross section is not well known, so the approach was to assume the polarization interaction accurately models the cross section. The elastic collision rate can then be subtracted from the data in Figure 45b to provide a *lower* bound on the detachment rate. This bound is displayed in Figure 47.

By subtracting the Langevin rate from the total, it was implicitly assumed that every elastic scatter causes a loss of I^- signal. This is not the case. A small angle scatter will permit the ion to continue to contribute, perhaps in a reduced form, to the image current of the I^- beam.

Estimate of Collisional Dephasing

To estimate how many elastic collisions were required to cause a complete loss in ion signal, the data for energies below the electron affinity (3.07 eV) was examined. In this regime, detachment is thermodynamically forbidden and the signal decay can only be attributed to elastic collisions. By fitting the total cross section data to the form A/v (as shown in Figure 48 for Xe), it was determined that it took 8.9 ± 0.4 , 2.6 ± 0.4 and 3.1 ± 0.5 elastic scatters in Ne , Xe and CF_3I , respectively, to account for the observed decay rate which occurs below the electron affinity. That Ne has a much higher requirement than the others follows from the fact that I^- (~ 127 amu) is much heavier than Ne (~ 20 amu) but

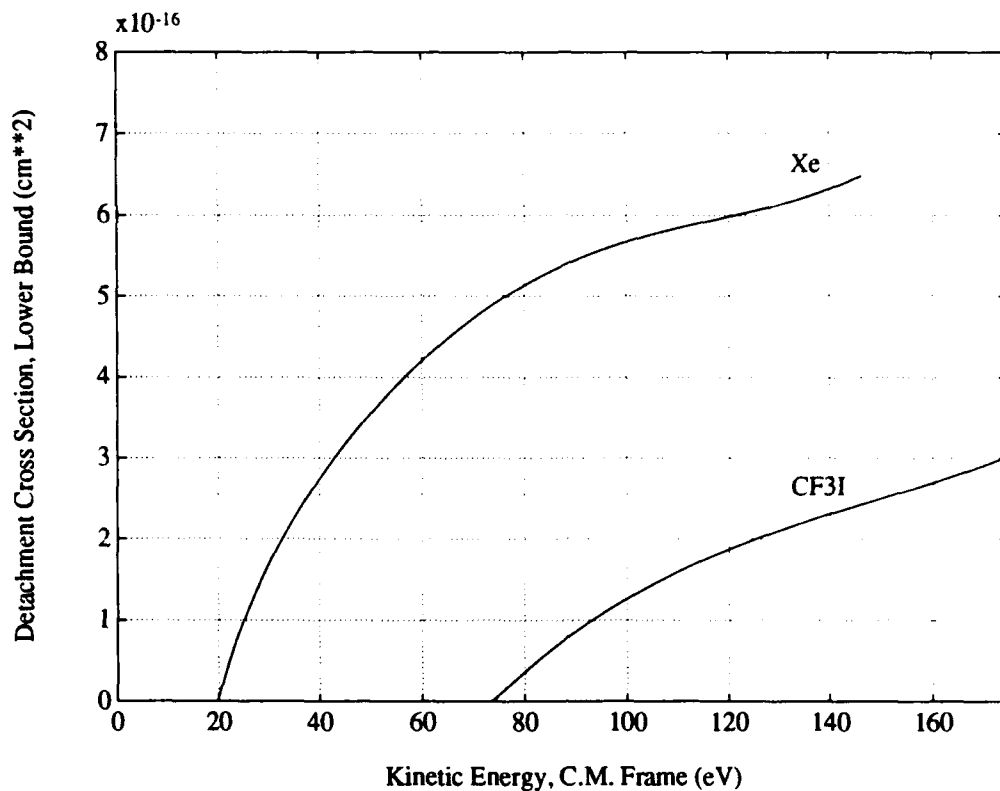


Figure 47. Lower Bound for Collisional Detachment. The lower bound for *Ne* is zero over the energy range measured.

lighter than *Xe* (~ 131 amu) and *CF₃I* (~ 196 amu); conservation of momentum and energy prevent the scattering angle on *Ne* from exceeding 9° in the lab frame (no backscatter). All collisions off *Ne* will be small angle and have a lower probability of perturbing the coherence of the ion motion.

Results and Discussion

Taking the results for collisional dephasing and applying them to the Langevin cross section, the best estimate of the detachment cross section was obtained. The summary of results for each collision system and its comparison to previous work follows.

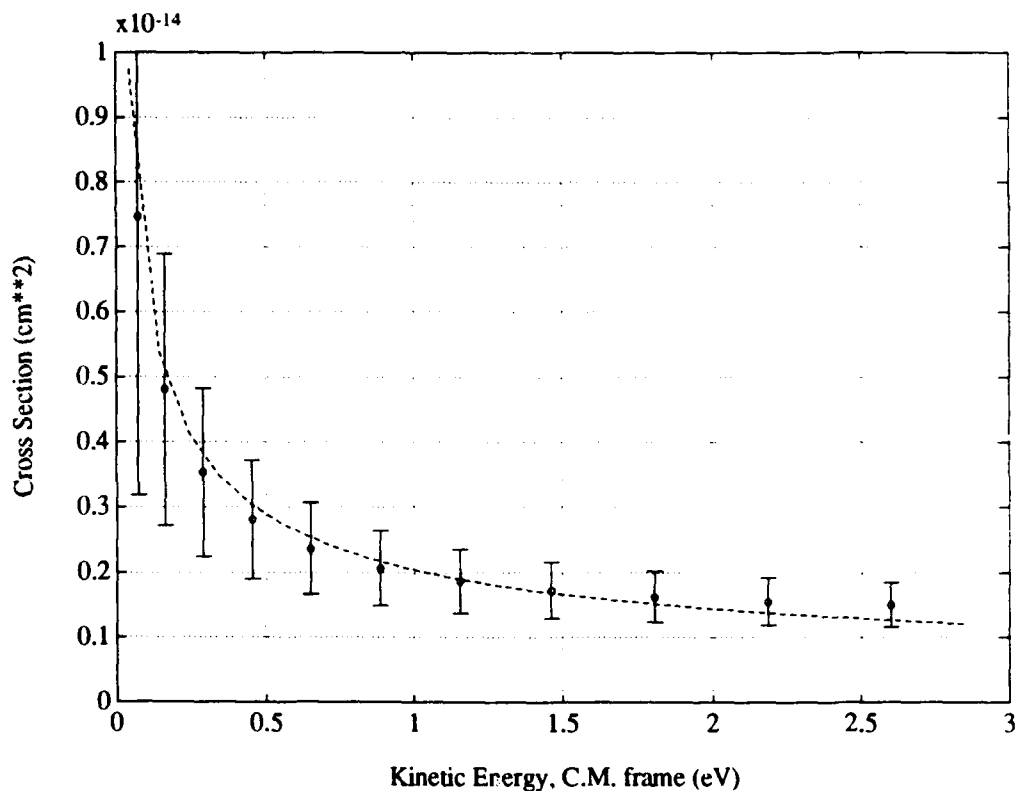


Figure 48. Elastic Scattering Efficiency Below the Electron Affinity

$I^- + Xe$. The collisional detachment summary for $I^- + Xe$ is shown in Figure 49. The upper and lower bounds, determined as discussed above, are displayed. The middle trace is the best estimate of the detachment cross section, based on a 38% dephasing efficiency (on average, roughly two in five elastic collisions result in a complete loss of ICR signal) for momentum transfer collisions. The dashed lines give the $\pm 67\%$ confidence level of the best estimate. There is also a horizontal error bar, highly dependent on energy (see Figure 17), which is not displayed.

Previous work on $I^- + Xe$ is also included in Figure 49. Pictorial data from Bydin and Dukel'skii [18] and Haywood et al. [55] were digitally scanned for inclusion. Their work made detachment measurements using collision chambers, where a momentum analyzed anion beam is launched through a gas cell. Electrostatic fields sweep the low energy detached electrons to a collector; surviving anions are collected elsewhere. Comparison

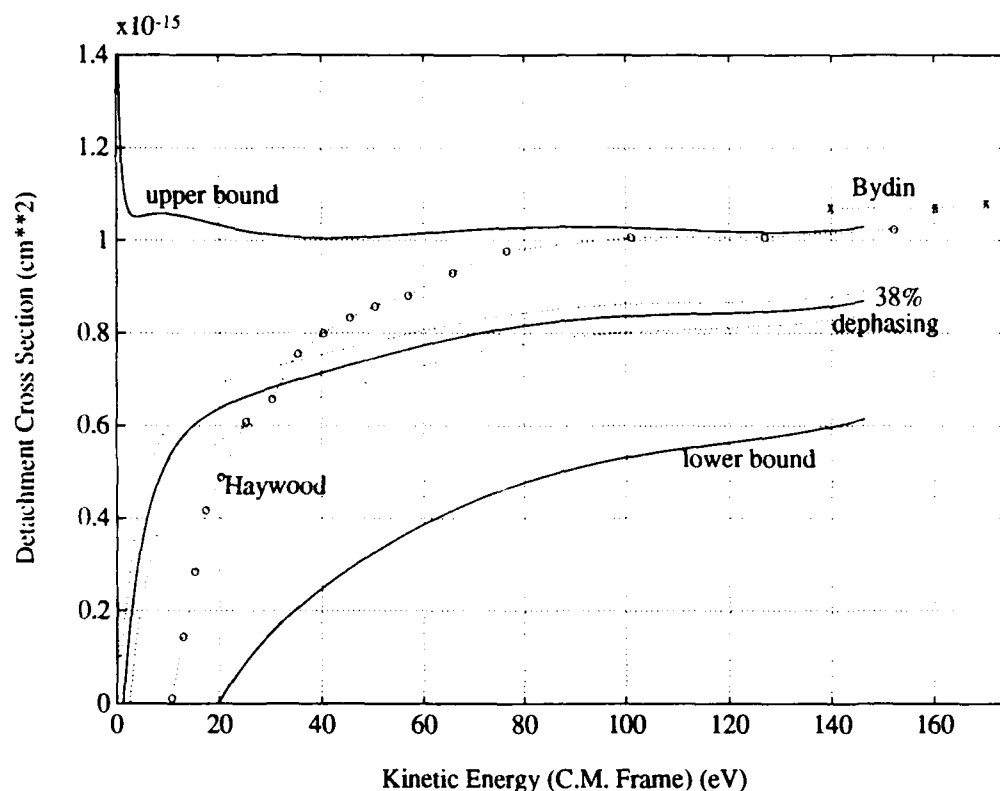


Figure 49. Collisional Detachment Summary for $I^- + Xe$

of the two signals as a function of beam energy can permit sensitive detection of the detachment threshold, but the collisional history (the number of elastic collisions) of the ion beam prior to detachment or collection is unknown.

In 1957, Bydin and Dukel'skii made halide anion-rare gas detachment measurements over the energy range 200-2000 eV (lab frame). They reported the first resolution of the detachment threshold, although the mass ratio permitted such resolution for only He and H_2 targets. Haywood et al. published the most recent (1981) and comprehensive data on collisional detachment of I^- with rare gas targets. The lab frame energy ranged from threshold to 500 eV. All thresholds were resolved (see additional discussion below).

The previous results are consistent with the bounds established here, acknowledging Bydin and Dukel'skii's data are slightly higher than the upper bound. For $\epsilon_{C.M.} > 75$ eV,

both previous works closely match the upper bound. Perhaps it is more than coincidence that their experiments, which have no way to track elastic collisions, have similar results as the FTMS measurements which assume no elastic collisions take place. For high energies, the best estimate and the previous data are in agreement within error bars.

The cross sections are very different at low energies, which cannot be resolved by simply taking the dephasing efficiency to be inaccurate. A higher dephasing efficiency would bring the thresholds closer to agreement but worsen the agreement at high energy. A lower dephasing efficiency would worsen the threshold agreement. No explanation is offered for the different slopes.

$I^- + Ne$. The collisional detachment summary for $I^- + Ne$ is shown in Figure 50. The best estimate is the lower solid trace, and is based on a 11% dephasing efficiency (on

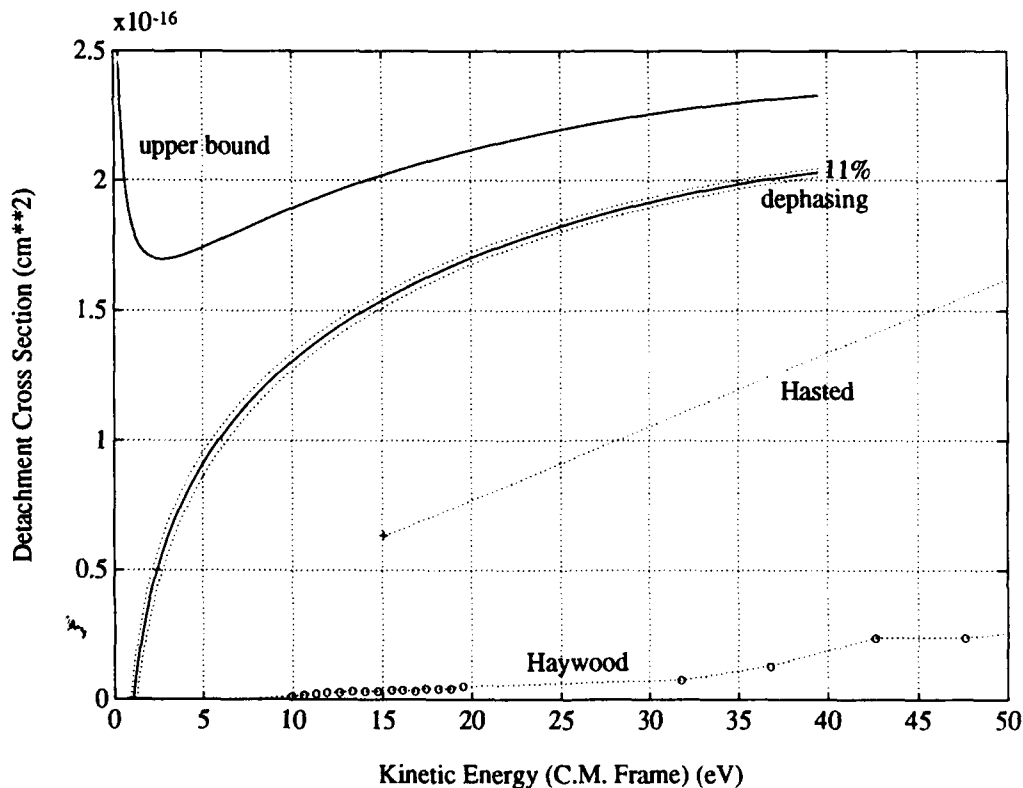


Figure 50. Collisional Detachment Summary for $I^- + Ne$

average, only one in nine elastic scatters will account for a loss in ion signal). The dashed lines in the near vicinity of the middle trace represent the 67% confidence level of the best estimate. An assumption of 100% dephasing results in no detachment—the entire signal decay is attributed to elastic scattering. Therefore, the lower bound is zero over the energy range measured.

Previous work, by Hasted [54] and Haywood et al. [55], is consistent with the bounds reported here. There is significant disagreement at all energies between their work and the best estimate. A fourth measurement, by Bydin and Dukel'skii [18], exceeded the energy range in the figure, but extrapolated closest to Haywood et al.'s data.

Collisional detachment of $I^- + Ne$ has long been recognized as an unusual case which doesn't follow the trends established by other halide anion-rare gas systems. Bydin and Dukel'skii recognized the correlation between the detachment probability and atomic number was defied by $I^- + Ne$. Hasted (1952) used a collision chamber for measuring detachment (and charge transfer of cations) over the energy range 100–3600 eV (lab frame). His inopportune choice of primarily Ne targets led him to conclude the much larger cross sections achieved by other rare gas targets indicated anion excited states. De Vreugd et al. [31] performed a differential scattering study of $I^- + Ne$ at energies of 1000–3000 eV. They observed an energy dependence which could not be described by the complex potential model; they hypothesized the $I^- + Ne$ ($X^1\Sigma$) potential energy surface does not cross the $I + Ne$ ($X^2\Sigma$) surface. If true, direct collisional detachment would require dynamic transitions from a bound state to the continuum.

$I^- + CF_3I$. The collisional detachment summary of $I^- + CF_3I$ is shown in Figure 51. The best estimate is based on a 32% dephasing efficiency. As before, the dashed lines represent the 67% confidence level about the best estimate and the horizontal error bars associated with the uncertainty in energy are omitted.

There has been no previous work reported for $I^- + CF_3I$.

Lack of Theoretical Predictions. One cannot look to theoretical studies to resolve differences in the experimental observations. The theory of collisional detachment is

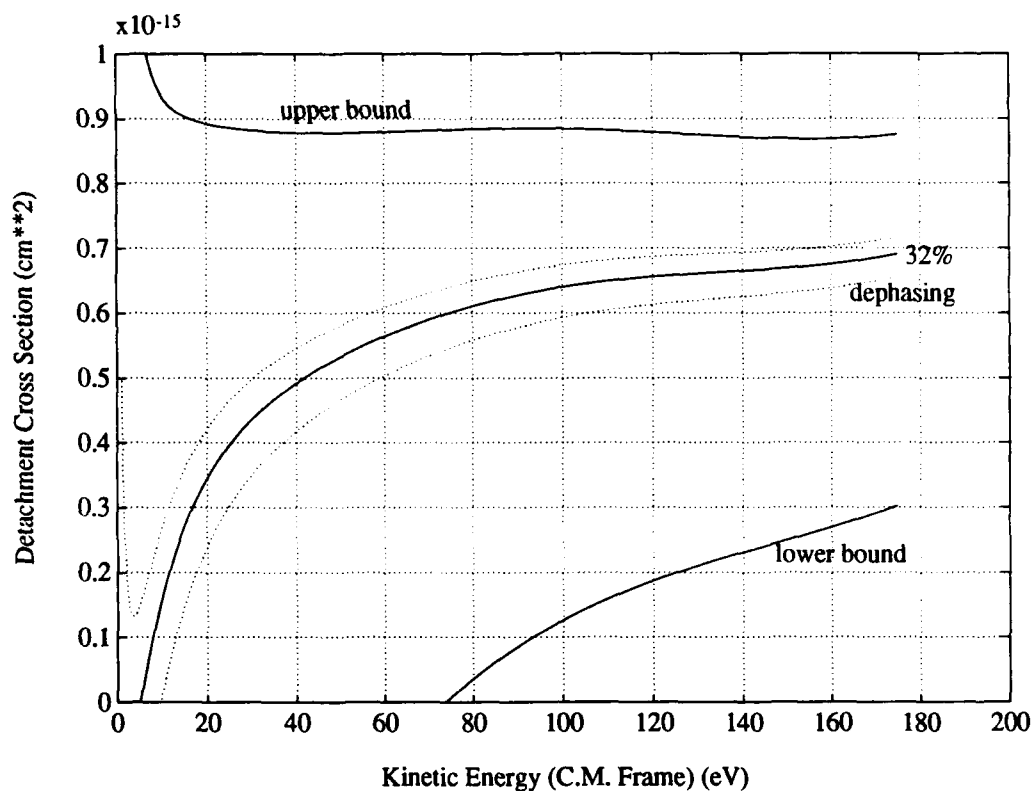


Figure 51. Collisional Detachment Summary for $I^- + CF_3I$

not well understood. At high energies, where the Born approximation is valid, predictions are close to experimental observations. At low to medium energies (the regime reported here), where a molecular description is required, prediction is generally less accurate.

The two common theoretical approaches are the zero range potential model (for example, [32, 70, 37]) and the complex potential model (for example, [19, 20, 31, 76, 117]). Both require detailed information about the molecular core during the collision. Electronic structure calculations for iodine are difficult due to the relativistic and the various coupling (spin-orbit, orbit-orbit, spin-spin, etc) corrections associated with its heavy nucleus [141:17–21]. No potential energy surfaces or subsequent collisional detachment predictions have been located in the literature for any collision involving iodine anions.

Scaling With Target Size and Polarization. All three detachment cross sections were still increasing at the highest energy (~ 300 eV, lab frame) measured. At that point, the magnitudes were 8.7×10^{-16} cm² (*Xe*), 2.0×10^{-16} cm² (*Ne*), and 6.9×10^{-16} cm² (*CF₃I*). For the limited sample size of three targets, the detachment cross section does not scale with target size, since *CF₃I* is spatially larger than *Xe*.

The cross section magnitude does not scale with polarizability. Early experimental work invoked long range forces to explain their measurements. Mason and Vanderslice [89] showed the polarization interaction plays a very limited role in the magnitude of the detachment cross section. Since the polarizability of *CF₃I* is roughly twice as high as *Xe*, their results are confirmed (for the limited set of targets herein).

It is curious that although *CF₃I* is more polarizable, spatially larger and has a variety of molecular channels available, it has a smaller detachment cross section than *Xe*.

Detachment Thresholds. Using the upper and lower bounds for detachment, the detachment threshold range is established:

Ne: 0– ∞ eV

Xe: 0–20 eV

CF₃I: 0–74 eV

Use of the extreme detachment bounds does not provide much insight on the detachment threshold. Using the best dephasing estimate results in detachment thresholds of $1.1^{+0.3}_{-0.3}$ eV (*Ne*), $1.4^{+1.2}_{-1.4}$ eV (*Xe*), $5.1^{+4.5}_{-5.1}$ eV (*CF₃I*). Haywood et al. [55] measured thresholds of 3.04 ± 0.26 eV (*Ne*) and 8.5 ± 0.4 eV (*Xe*). The latter is nearly three times the electron affinity for iodine. The former confirms that $I^- + Ne$ is an unusual system—it has the only threshold ever reported that is consistent with the electron affinity.

For the best estimate reported here, both *Ne* and *Xe* have thresholds below the electron affinity. Due to the uncertainty in the precise form of the elastic cross section, FTMS is not the best technique for measuring detachment thresholds.

Three-body Attachment. Collisional detachment is the reverse process of three-body attachment ($X + Y + e^- \rightarrow X^- + Y$). The rates for the forward and reverse direction

are related through detailed balancing [120:386-391]. Three-body attachment is difficult to examine directly by experiment, so the best insight may be gained through the detachment reaction.

Detachment thresholds are in the range of several eV. For temperatures of ~ 1000 's K, detailed balance computations are extremely sensitive to uncertainties in the threshold. The data reported here has the worst precision at threshold, so detailed balance calculations were not performed. Should three-body attachment rates be desirable at temperatures exceeding several eV, detailed balancing could be performed to reasonable precision.

Conclusions

Collisional detachment of I^- has been measured using FTMS. Negative ions are excited to well defined energies over the range 1-300 eV (lab frame) by using the ion cell as an rf accelerator. The ion signal decay is attributed to elastic and inelastic collisions. By measuring the decay time and determining the gas pressure, the total collisional rate constant can be computed. Assuming no contribution from elastic scattering establishes the upper bound for the collisional detachment cross section.

Using the Langevin rate for the elastic component, which assumes every elastic collision causes a loss of ion signal, establishes the detachment lower bound. Examination of the signal decay below the electron affinity permits estimation of the dephasing efficiency of elastic scattering. Deducting this estimate from the total collision rate results in the best estimate of the detachment cross section. Near threshold, the large elastic component makes threshold resolution difficult.

Measurements were made on Ne , Xe and CF_3I targets. That Xe had a larger cross section than CF_3I supports early theoretical work which showed the polarizability of the target plays a negligible role in the detachment probability. The cross sections were still increasing at the highest energy measured, so a lower bound for the maximum detachment cross section is estimated at $2.0 \times 10^{-16} \text{ cm}^2$ (Ne), $8.7 \times 10^{-16} \text{ cm}^2$ (Xe) and $6.9 \times 10^{-16} \text{ cm}^2$ (CF_3I).

VI. Summary and Implications

This research investigated measurements of collisional detachment Fourier Transform Mass Spectrometry (FTMS). The FTMS ion cell is used as an rf accelerator for energy resolved measurements. Since ions are not collected in FTMS, particle trajectories and the observable image current were calculated from first principles.

The ion motion was simulated by solving the time-dependent electrostatic boundary value problem for arbitrary boundary conditions (rf excitation and trap potential) in a cubic ion cell. A precise knowledge of the ion kinetic energy resulted. The relationship between the ion motion and the image current was accurately quantified. Given the excitation waveform and the preamplifier response characteristics, the number of ions can be determined to within $\pm 20\%$ without knowledge of any other experimental parameters. Given additional information, such as how quickly the ions relax in the trap potential, the number of ions can be determined to high precision.

The simulation was used to examine other FTMS issues. Resonant sinusoidal excitations with identical $V_{pk}T$ (the product of the peak excitation amplitude and the duration of the excitation) have the same radius only to first order. The rf excitation must be over-sampled by a factor of 10 or larger to achieve the same radius as from a continuous (infinite bandwidth) excitation. The trap potential well was computed and ion evaporation (loss of energetic ions over the trapping barrier) was quantified. SWIFT excitation was shown to have off-resonance excitation, which may result in premature ion ejection.

The mathematical descriptions of ion motion and image current were verified by making ionization cross section and ion kinetics measurements. Cross sections for ion production by electron impact with CF_3I were reported for the first time in the energy range of 10–50 eV. I^- was the only anion observed, and it persisted over the entire energy range. This implied formation by polar dissociation, in addition to the previously reported dissociative attachment. Six positive ions were observed (CF^+ , CF_2^+ , CF_3^+ , I^+ , CF_2I^+ , CF_3I^+), with CF_3I^+ having the largest cross section at all energies. The total ionization cross section has a threshold no higher than 10.9 eV and had a peak value no smaller than $4.5 \times 10^{-16} \text{ cm}^2$.

Ion kinetics measurements in CF_3I resulted in rate constants in agreement with previous results from well-established techniques. The branching ratio for I^+ and the collision induced dissociation of CF_3I^+ were dependent on the electron impact energy used for ion formation. This observation emphasized that caution must be applied when using rate constants determined from high energy electron impact to model plasma characteristics. Negative ion kinetics were also measured; I^- is unreactive in CF_3I .

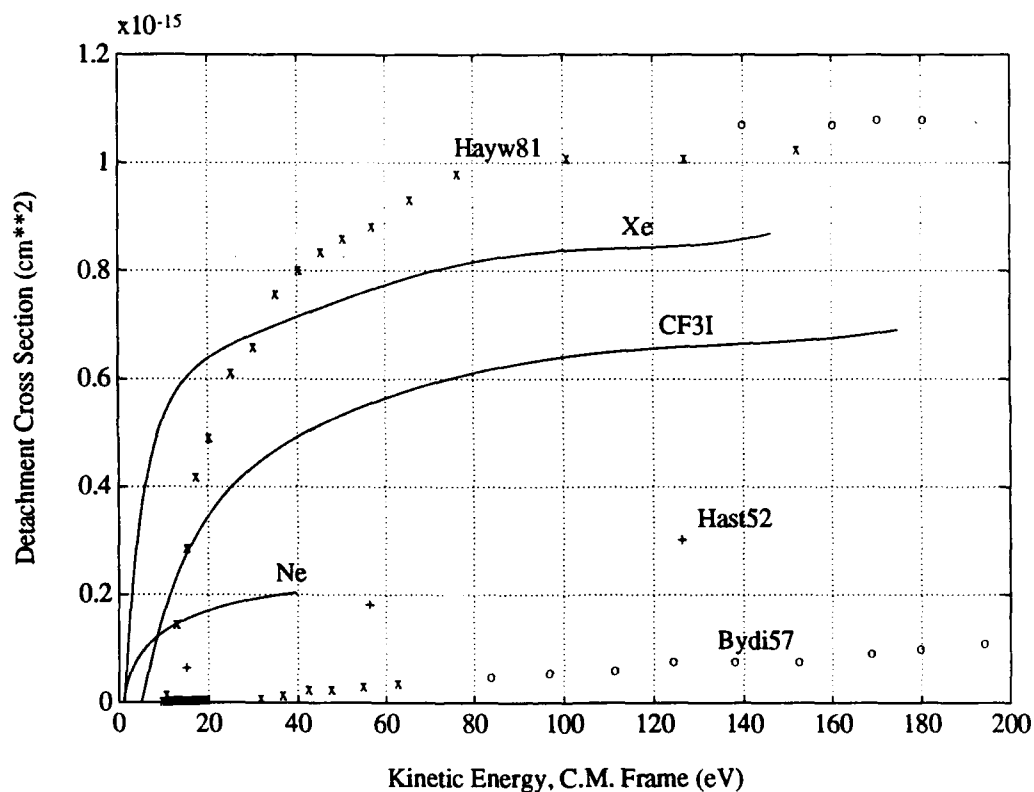


Figure 52. Collisional Detachment Cross Sections Compared to Previous Work

Collisional detachment was observed using FTMS. The technique permits monitoring of the total collisional losses of accelerated anions as a function of time. By assuming elastic scattering is determined solely by the polarization interaction, a lower bound on the detachment cross section is established. The elastic contribution is modified, since every scatter does not cause a loss of ion signal. Subtracting this modified elastic contribution results in the best estimate of the detachment cross section. The threshold for detachment

is bounded and may be as low as the electron affinity. A consolidated summary of results is shown in Figure 52. The success of collisional detachment measurements may lead to use of FTMS for other energy-resolved inelastic measurements, such as charge transfer or momentum transfer.

Appendix A. Experiment Details

The Wright Laboratory FTMS is a Nicolet FTMS-1000 system, procured in the mid-1980's. From 1989 through the early stages of this dissertation, the spectrometer was overhauled and most subsystems were replaced with "off the shelf" modular components, which greatly enhanced system reliability, efficiency and performance. Besides improving system capability, the move to modular components provides flexibility for further upgrades, particularly in the computational area. Computer technology is advancing so rapidly that one can anticipate doubling the computational power every few years. Of the original Nicolet system, only the magnet (with cryogenic shield), ion trap, gas manifolds and a portion of the vacuum chamber remain intact. A block diagram of the FTMS is shown in Figure 53. This chapter provides an overview of the present instrument configuration and component performance.

Reagent Gas Flow

The precision and accuracy of cross section work using FTMS is largely controlled by how well the reagent gas pressure is known. The ability to add, delete or maintain stable reagent gas pressures is dictated by the vacuum pumps, manifolds, valves and pressure gauges.

Vacuum Pumps. The vacuum system features a redundant, entirely oil free pumping system. The original vacuum pumps were oil diffusion type, which required higher maintenance and presented a contamination threat to the ion cell. The new pumping system, shown in Figure 54, incorporates a cryopump and turbopump as the primary elements.

The cryopump is model Cryo-Torr 8, manufactured by CTI-Cryogenics. It is highly reliable and operates on the principle that gases can be condensed and trapped at extremely low vapor pressures. The cryopump requires almost no maintenance, has no operating fluids and requires no backing pump. The rated pumping speed is 1500 l/s (air), with the rated capability to reach pressures below 10^{-9} Torr [28].

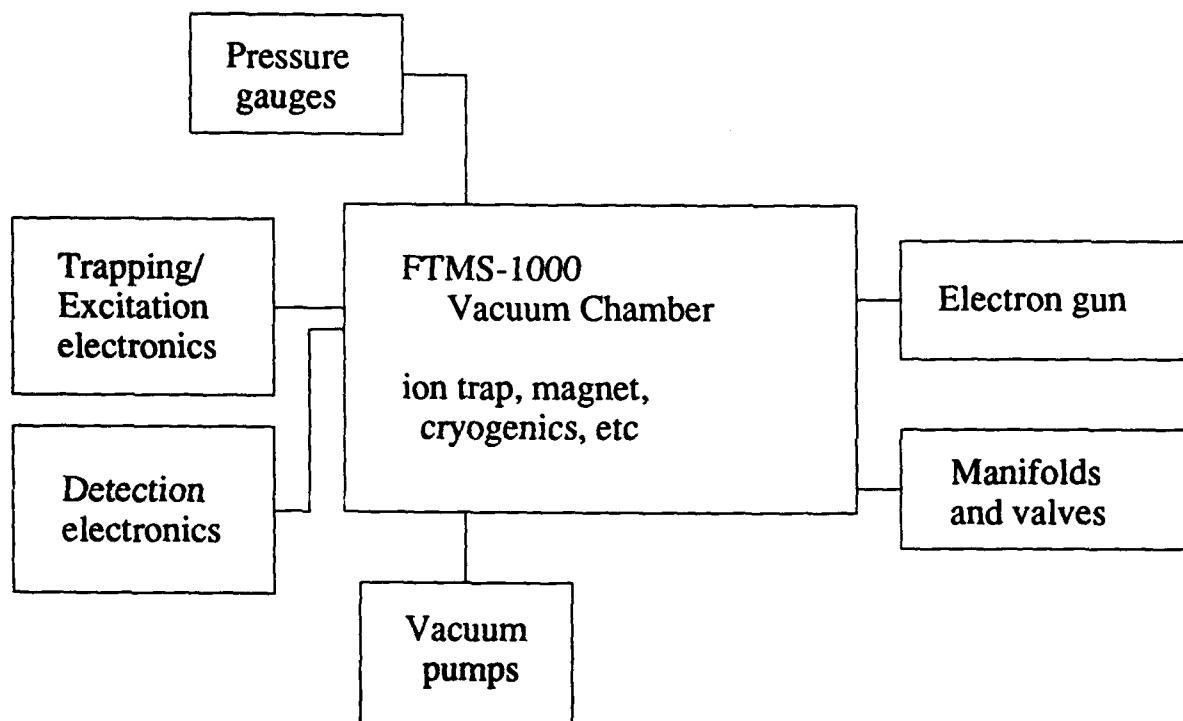


Figure 53. FTMS Block Diagram

The turbomolecular pump is model 5150, manufactured by Alcatel Vacuum Products. It has a 100% turbo multistage design with a 27000 rpm rotation at full speed. The rated pumping capacity is 140 l/s (nitrogen), with the rated capability to reach system pressures below 10^{-8} Torr [3].

The turbomolecular pump requires fore pumping. This is performed by a drag pump and a diaphragm pump. The molecular drag pump is an Alcatel model MDP5010. This pump has a multiblade rotor which runs at 27000 rpm. It may be started at atmospheric pressures and has a pumping speed of 7.5 l/s (nitrogen), with the capability to reach pressures below 10^{-5} Torr [2]. The twin diaphragm pump is model N726.3ANP, made by KNF Neuberger, Inc. It provides 100% oil free pumping at 20 l/min (air) and is rated for pressures as low as 5 Torr [75]. The stock twin diaphragms have been replaced with teflon-clad diaphragms for maximum reliability during long pumping operations. Through

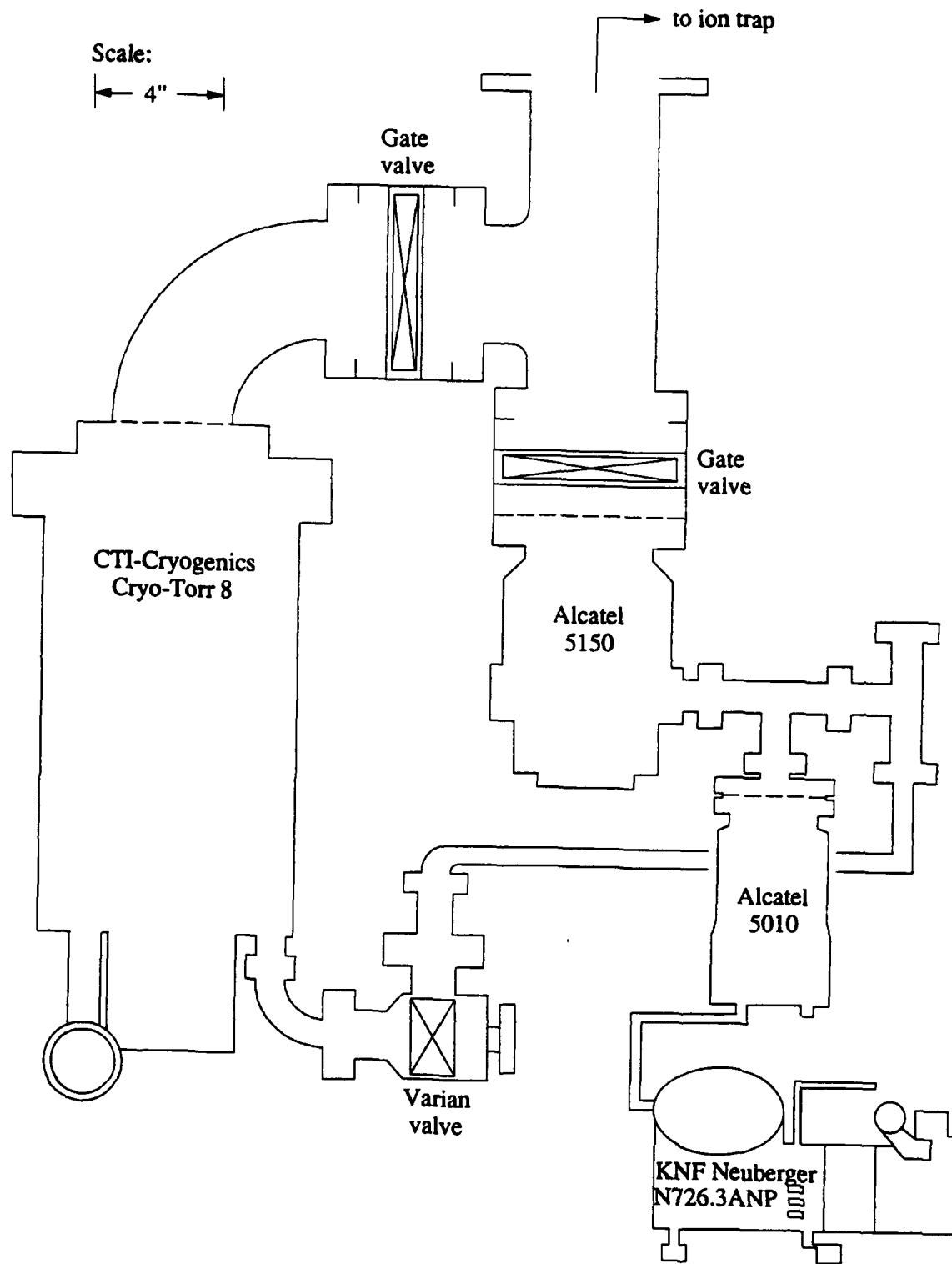


Figure 54. Vacuum Pump Schematic

cross-over valving, these pumps are used to clean the cryopump during a regeneration cycle.

With rare exception, the cryopump has been used as the FTMS vacuum pump. Base pressures typically reside in the high 10^{-9} Torr range, with most of the base pressure attributed to water vapor. Other trace species include carbon dioxide, nitrogen and oxygen. As expected, it can take many hours to reach the nominal base pressure after experiments with a "sticky" reagent gas (such as trifluoromethyl iodide or tetraethoxysilane).

Gas Manifolds. The source gas manifolds were custom designed and delivered with the original Nicolet system. An overhead schematic of the FTMS is shown in Figure 55. There are two manifolds, referred to as "upper" and "lower", each monitored by dual capacitance manometers (10 Torr, 1000 Torr). Changing reagent gas is a quick task; purging the manifold of the previous reagent can take much longer. The manifold design is straightforward; system capability and performance is contained in the valving.

Valves. Vacuum valves are available to isolate the vacuum chamber from all external plumbing. For the source gas manifold and the pressure gauges, standard bellows valves (manufactured by Varian and Nu-Pro) are employed, while the primary pumps use gate valves (see Figure 54) driven by fractional horsepower gearmotors (Bodine Electric Company type NCI-13D3).

There are additional specialized valves in the source gas manifold, which are two variable leak valves and a pulsed valve. The variable leak valves are model 951-5100 made by Varian. They are manually operated by a thumbscrew and are highly sensitive in their ability to permit constant low pressure gas flow. Leak rates as low as 10^{-9} Torr-liters/second are possible [132]. The pulsed valve is a model LPV made by Lasertechnics. It is a voltage activated valve, not manually controlled, designed to produce continuous or short pulse molecular beams [77]. The model 203B Pulsed Valve Driver, also made by Lasertechnics, converts TTL input waveforms into high voltage (typically 120 volts) driver pulses. A driver pulse operates the pulsed valve by flexing a piezoelectric bimorph disc, which lifts the poppet (a plunger) from the nozzle allowing gas to flow. In the experiments

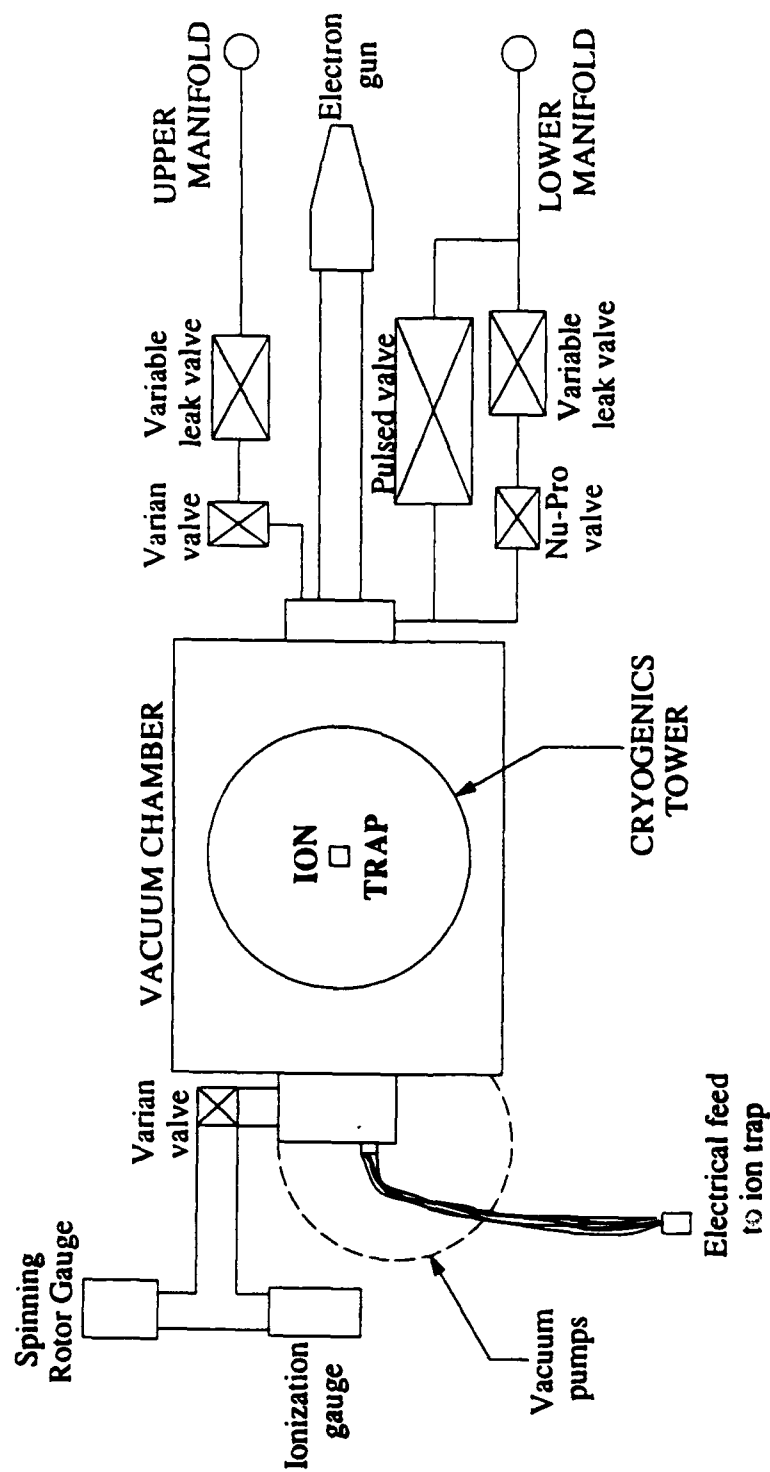


Figure 55. FTMS, Top View

reported herein, reagent gas is added through one or both variable leak valves to form a steady state pressure in the 10^{-8} — 10^{-5} Torr range. The pulsed valve, in conjunction with a spinning rotor gas friction vacuum gauge, is generally only used to calibrate the FTMS.

Pressure Gauges. Accurate measurement of pressure at ultra-high vacuum (pressures less than 10^{-6} Torr) in the presence of a strong magnetic field is difficult. These difficulties have been discussed previously [48] and include the difference in the conduction path length due to the location of the pressure gauges with respect to the ion trap and vacuum pumps, perturbation of gauge calibration by the fringe magnetic field and the ionization gauge response having to be scaled by the gas ionization cross section, which itself may be the object of the measurement.

Two pressure gauges are employed to monitor system pressure: a standard nude ionization gauge and a spinning rotor gas friction vacuum gauge. The ionization gauge has a hot filament which emits electrons to form ions in the reagent gas. The ions are then accelerated and collected; the ion current determines the pressure [41]. Disadvantages of ionization gauges include emission current stability requirements, ion trajectories to the collector are perturbed by the FTMS fringe magnetic field and the gauge is calibrated for nitrogen (N_2). The spinning rotor gauge (SRG) is a model SRG-2 made by MKS Instruments. The SRG determines pressure by the frictional torque of the gas being investigated. A rotating sphere is suspended magnetically; measuring its deceleration determines the gas pressure if the mass and temperature of the reagent gas are known. Initial acceleration and periodic reacceleration of the sphere are performed by a motor. The SRG can measure down to the 10^{-7} Torr range, but is only precise at pressures exceeding 10^{-5} Torr [96]. Under typical experimental conditions (pressures in the range 10^{-8} to 10^{-7} Torr), the two pressure gauges cannot accurately determine the gas pressure. They only contribute data on the stability of the gas flow.

The procedure for accurate determination of reagent gas pressure has been described previously [48]. It is accomplished using the pulsed valve and the SRG. The system leak-up rate is measured with the vacuum chamber isolated from the pumps and manifolds. After pumping back down, the pulsed valve is driven repeatedly, allowing bursts (puffs) of

reagent gas into the isolated chamber, as seen in Figure 56. When enough gas has been added to exceed 10^{-5} Torr, the SRG provides a precise pressure measurement. Knowing the number of gas puffs, the total pressure and the background leak-up rate calibrates the

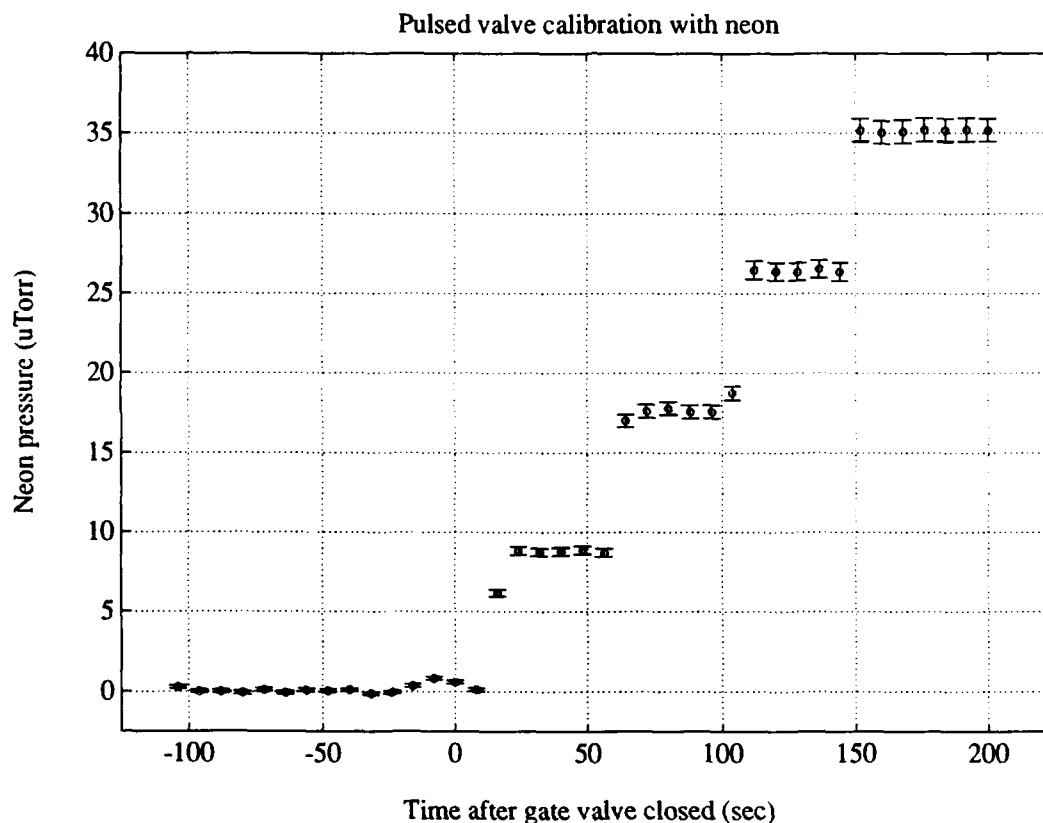


Figure 56. Pressure Calibration Using the Spinning Rotor Gas Friction Gauge. The gate valve is being closed in the 10 s prior to $t=0$. The laser pulsed valve is multiply triggered every 45 s. By knowing the final pressure and how many bursts of neon (Ne) are emitted, the pulsed valve is calibrated. The displayed data has been corrected for a background leak-up rate of 6.51 nTorr/s.

amount of gas released in a single puff (which is too low for accurate measurement by the SRG).

Pulsed valve consistency was examined by repeating the procedure several times with different gases. The mean pressure per puff was stable, with the standard deviation never exceeding 2.5% of the mean. Typically, the standard deviation was closer to 1.5% of the mean, indicating excellent pulsed valve stability.

Trapping Ions

Superconducting Solenoid. The steady-state magnetic field is created by a Nicolet 3 T superconducting solenoid, which replaced the original 3 T magnet in late 1988. The solenoid is maintained at liquid helium temperature (4.2 K). It has a room temperature bore of 15.2 ± 0.1 cm and a length of 78.7 ± 0.3 cm. There is excellent field homogeneity (100 parts per million) at the ion cell because of the small aspect ratio (radius to length). For all experiments reported here, the magnetic field was tuned to 1.980 ± 0.002 T (a solenoid current of 23.5 A), which permits ion detection to masses as low as roughly 16 amu (the bandwidth limitation of the preamplifier).

Ion Cell. The ion cell is the original Nicolet 5 cm cubic trap. It is located at the center of the superconducting solenoid. Early FTMS cell designs were rectangular ($2.5 \times 2.5 \times 7.5$ cm) [24, 25], but the cubic cell provides better resolution and greater reliability [24]. The six sides are electrically isolated by a spatial gap or by ceramic insulator supports. The end plate gap is not specified in the manufacturing process; it has a dimension of approximately 0.24 cm [73]. Although the six sides are locally isolated, they are ultimately referenced to the same ground through the preamplifier input impedance, the rf amplifier output impedance and the digital-to-analog convertor (DAC) output impedance. As shown in Figure 57, the two sides orthogonal to the magnetic field are the trapping plates, while the four sides parallel to the field comprise the excite and detect plates. Including the electron gun collector, seven active electrical contacts are on the vacuum system feedthrough (depicted in Figure 55).

Ion Formation

Although a variety of techniques exist to create ions (laser desorption, photoionization, electron impact, etc), the apparatus is presently configured only for electron impact.

Electron Gun. The electron gun is a model ELG-2, made by Kimball Physics. It is rated for energies of 10-1000 eV with beam currents of 1 nA-3 μ A [74]. The filament has a radius of 0.04 cm and is under 0.1 cm long. It operates at approximately 2300 K.

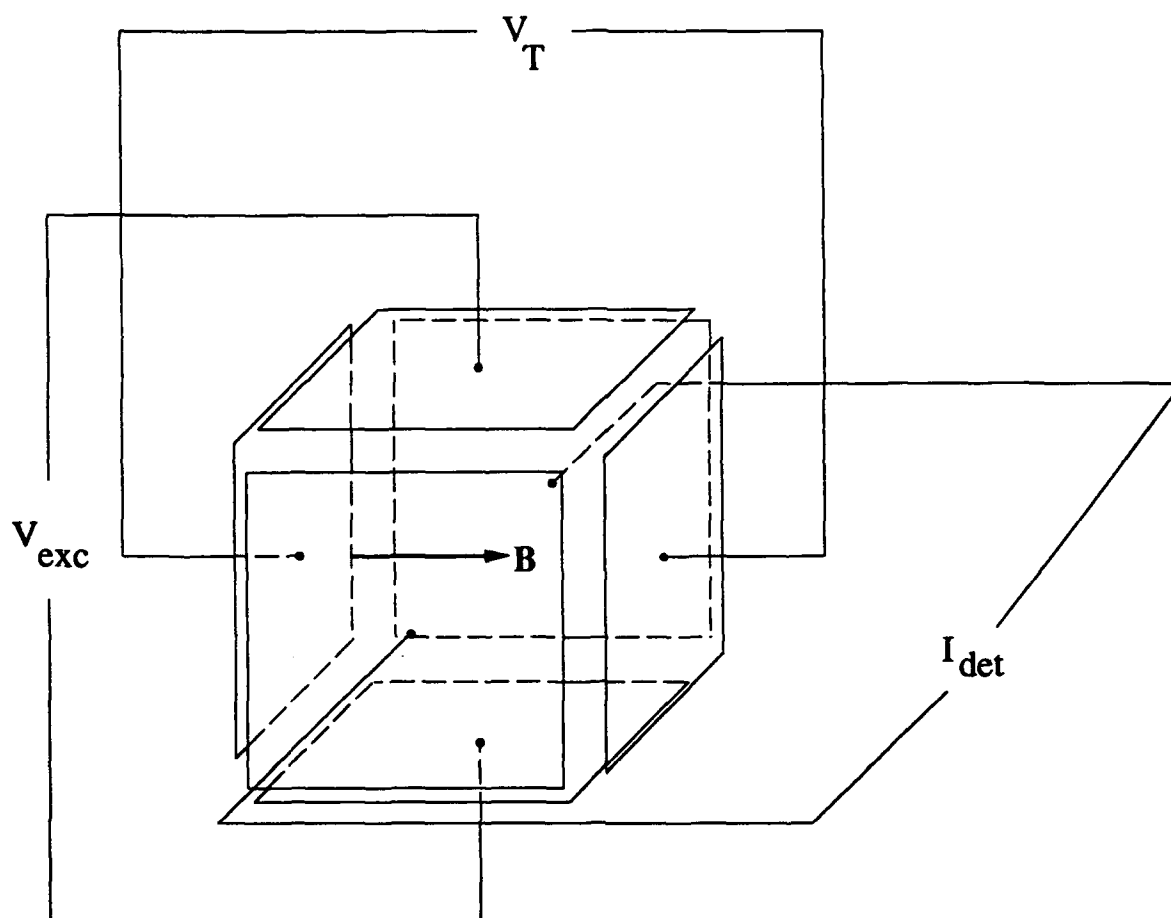


Figure 57. FTMS Ion Cell. V_T is the trapping potential, V_{exc} is the rf excitation and I_{det} refers to the image current associated with the detect plates.

The energy spread of the beam is about 0.2 eV plus the space charge well of the beam and the beam spatial distribution is gaussian. This gun replaced the original electron gun well before the system overhaul because the previous gun could only produce low currents at low energies (less than 50 eV).

The electron gun is mounted just under 100 cm from the ion trap—remote with respect to the typical electron gun location in most FTMS's. The gun is rated to have a beam diameter of 0.2 cm at a distance of 2 cm, but the beam undergoes compression as it moves into the strongly converging magnetic field. This increases the space charge, which increases forces trying to expand the beam. The competing forces of magnetic compression

and electrostatic repulsion have been estimated [48] and the electron-neutral interaction volume (inside the trap) cannot exceed 0.2 cm^3 .

The electron beam passes through two small washers, with diameter 0.2 cm, located on the front and rear traps and onto a collector located behind the rear trap. Monitoring the front and rear traps prior to data collection guaranteed electron gun alignment. The collector output is available to record the electron beam intensity. The electron gun was operated in pulsed mode, with a typical output for a 4 ms beam on-time shown in Figure 58. For electron-impact cross section studies, the electron gun was run below 50 eV because

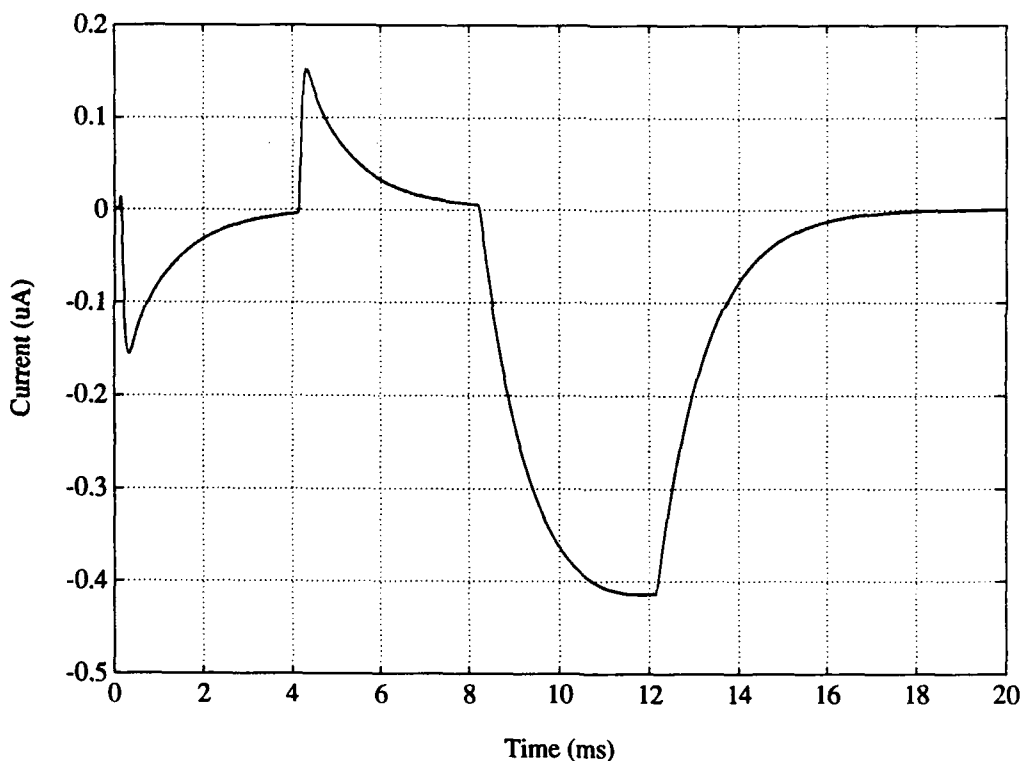


Figure 58. Typical Electron Gun Output. The actual output is the large negative pulse between 8–16 ms. The two earlier peaks (just after 0 ms and 4 ms) are capacitive pick-up of the changing trap bias (which electrostatically sweeps the trap of ions prior to ion formation) on the collector.

of secondary electron emission from the collector at higher energies [48].

The electron gun output can vary depending on how long it has been operating. It was noted that the current increased with time when the gun was initially turned on.

varying up to roughly 20%. To avoid stability problems, the gun was pulsed for several minutes before collecting data. The gun output was also dependent on the energy selected. Electron extraction is much more efficient at higher grid voltages (i.e., higher energies), as seen in Figure 59. By recording the collector output, ion signals were normalized for this

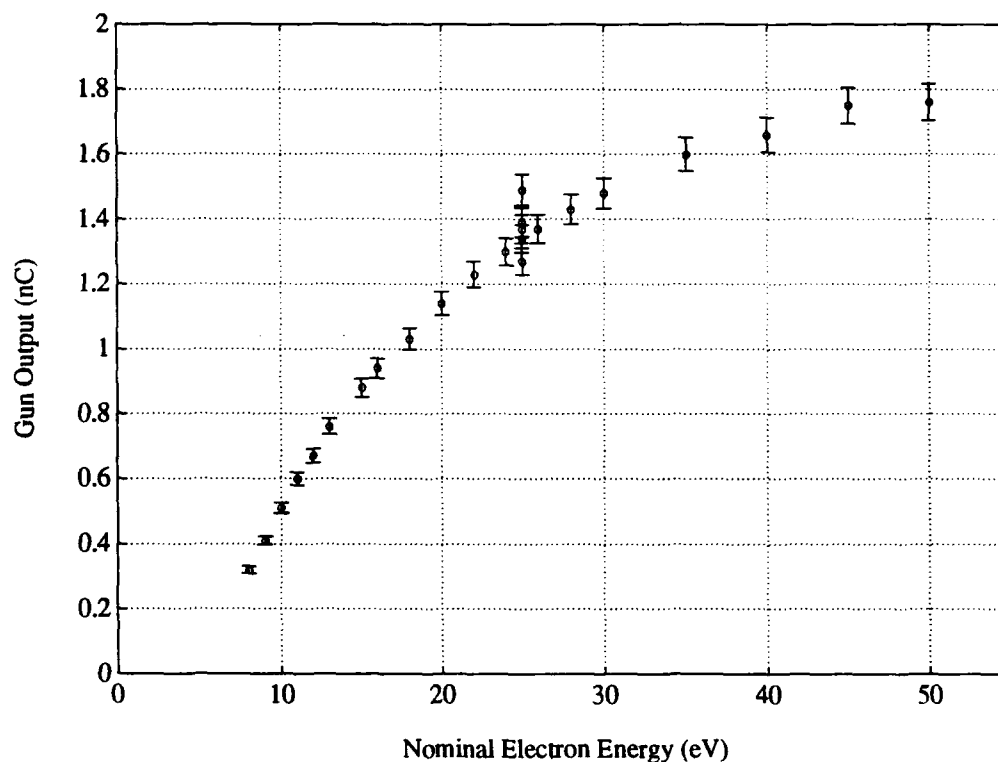


Figure 59. Electron Gun Output Versus Energy. When the only electron gun variable is energy, there is a sharp increase in the electron extraction efficiency at the gun's rated threshold.

variation.

Electron Transport. An electron sees a converging magnetic field, space charge and the trapping potential on its way from the gun to the collector. The magnetic field gradient will alter the pitch angle (defined as the angle between the electron velocity vector and the magnetic field vector), which may result in the electron mirroring before reaching the ion cell.

The path length an electron travels through the cell is determined by its energy and pitch angle. To verify the path length is independent of the nominal beam energy, a simple monte carlo simulation was constructed. The magnetic field was modelled as an ideal solenoid, with the dimensions of the actual magnet. Space charge and collisions were ignored. The electron energy distribution was taken to be maxwellian, with a temperature of 2300 K. The angular distribution at the cathode was assumed to be lambertian. Both positive and negative ion traps were simulated by taking the trap potential as +2 V and -2 V.

The results are summarized in Table 17. The probability of mirroring before reaching

Table 17. Electron Transport Through Ion Trap

Nominal Energy (eV)	Trap Potential (V)	% Mirroring Before Trap	Mean Path Length (cm)
8	2	7.3	5.50 ± 0.58
10	2	4.6	5.48 ± 0.59
12	2	3.2	5.46 ± 0.58
15	2	0.9	5.39 ± 0.53
20	2	0.1	5.29 ± 0.39
25	2	0	5.24 ± 0.32
30	2	0	5.19 ± 0.24
35	2	0	5.16 ± 0.21
40	2	0	5.14 ± 0.17
50	2	0	5.11 ± 0.14
8	-2	8.5	6.30 ± 2.16
10	-2	5.4	5.92 ± 1.45
12	-2	3.4	5.79 ± 1.20
15	-2	1.4	5.56 ± 0.85
20	-2	0.1	5.37 ± 0.55
25	-2	0	5.27 ± 0.38
30	-2	0	5.22 ± 0.28
35	-2	0	5.19 ± 0.24
40	-2	0	5.15 ± 0.19
50	-2	0	5.12 ± 0.15

the trap is nearly zero for most energies of interest. The path length statistics, which are represented by the mean and standard deviation in the table, are not strictly independent of beam energy. For positive ion trapping, the variation from 10-50 eV is only about 6%.

But for negative ion trapping, the variation is over 20%. The implication is that if the electron follows a longer path, there is a corresponding increase in the probability of ion formation. Cross sections reported in Chapter 3 assumed the electron path lengths were independent of electron energy; no corrections were applied to the data.

Ion Excitation

Ion excitation is performed by a digital function generator and a matched pair of rf amplifiers. These devices represent an improvement over the original excitation electronics, both in bandwidth and maximum output amplitude. A higher bandwidth device was chosen to ensure oversampling during excitation (as discussed in Chapter 2). Large excitation amplitudes are required for short excitation times and for stored waveform inverse Fourier transform (SWIFT) waveforms. Short excitations have the advantage of reduced magnetron motion, but the disadvantage of stronger coupling to axial motion (z -oscillations) along the magnetic field.

Excitation waveforms are loaded into the function generator memory from the computer. Timing is controlled by a digital-to-analog convertor (DAC). A schematic of the excitation electronics is shown in Figure 60.

Function Generator. The function generator is a LeCroy Corporation model 9112 Arbitrary Function Generator (AFG) [82]. It is a high performance AFG capable of generating standard or user-defined waveforms. The 9112 has a 12-bit dual channel output capable of ± 5 volts (into a $50\ \Omega$ load) at up to 50 megasamples per second. User-defined waveforms are limited to 65536 points by the high speed memory (64 kilobytes RAM), which occasionally created a trade-off between oversampling the excitation and the total excitation time.

The 9112 AFG has a variety of programmable features which provide tremendous flexibility for application to FTMS. The output rate may range from 20 ns to 100 sec (Nyquist frequencies of 25 MHz to 0.005 Hz) per time step. Triggering is usually performed externally from the DAC, although manual or bus triggering is available. The digital clock output is accurate to ± 4 ns and is used as a trigger for ICR signal acquisition, upon

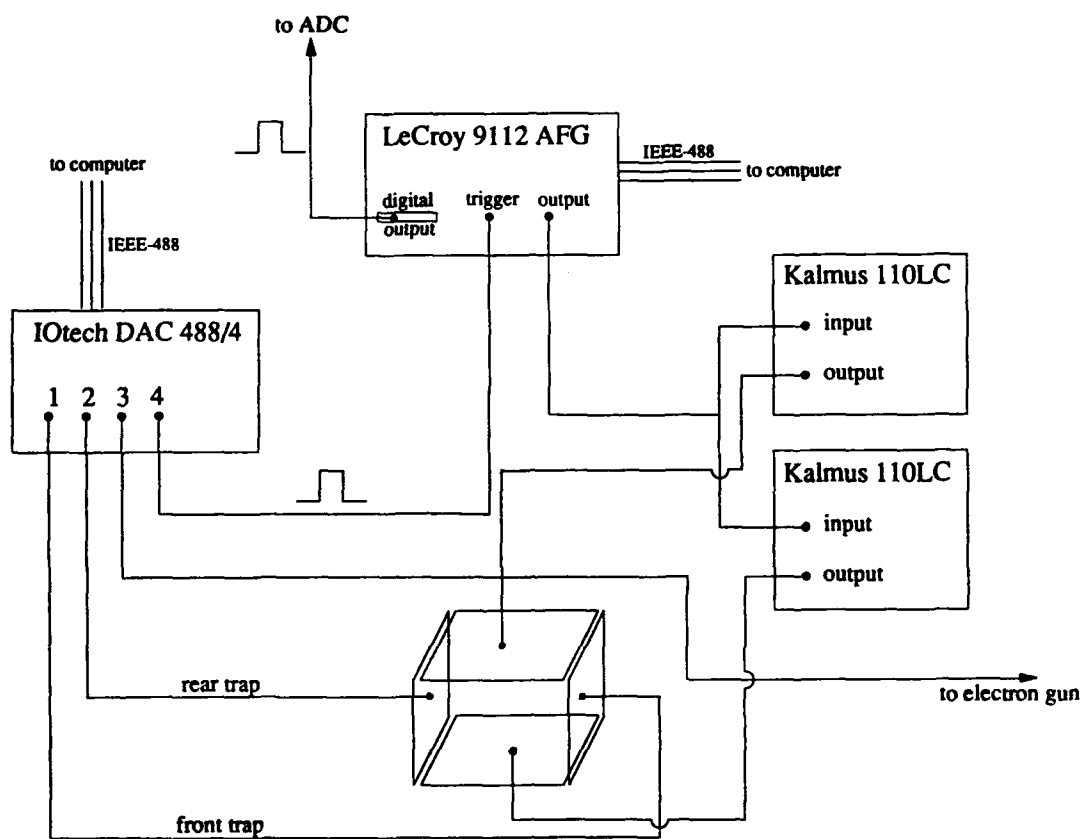


Figure 60. Schematic of Excitation Electronics. The DAC serves as the primary FTMS timing device. The Kalmus rf amplifiers are an inverted matched pair.

completion of excitation. The waveform amplitude may range from 100 μ V to 5 volts, although the latter drives the rf amplifiers to place over 10 kV/m across the ion trap. For most data reported herein, the AFG was run at 20 megasamples per second (10 MHz Nyquist frequency) with amplitudes of 1 mV to 1 V.

R.F. Amplifiers. The rf amplifiers are Kalmus Engineering model 110LC Wide-band R.F. Amplifiers [71]. Each amplifier is rated to have a power gain of 40 dB, with a gain flatness of ± 1.5 dB over the frequency range 10 kHz–100 MHz. The power output is rated for 10 watts (continuous wave) into a 50 Ω load. The 110LC is ideally suited for the wideband power sweeping commonly required by FTMS (such as SWIFT or chirp excitations).

The 110LC amplifiers are configured as an inverted matched pair to provide differential excitation. Since the amplifiers are rated into a 50 Ω load, additional calibration tests were performed to verify amplifier performance onto the nearly infinite impedance excite plates. Bandwidth exceeded the maximum source frequency available (25 MHz from the AFG). The high bandwidth has implications for ion excitation, which was discussed in Chapter 2. There was a minor mismatch in gain (up to 4%), as shown in Figure 61. The gain flatness was within specification, but was quantified as a function of frequency for the simulation work (see Chapter 2). Both the gain mismatch and gain flatness do not impede FTMS operation; their variation has been quantified and makes only a small contribution to the overall variance (*i.e.*, error bars) obtained in a typical experiment.

Digital-to-Analog Convertor. Model DAC488/4, manufactured by IOtech, is the digital-to-analog converter (DAC). This device is a multiple output DAC interface for the IEEE-488 bus. It has a 12-bit D/A convertor with three full-scale output ranges of ± 1 volt, ± 5 volts and ± 10 volts. Rated isolation from IEEE-488 common and other output ports is 500 volts, making the DAC a suitable trigger reference for the electron gun. The DAC has four analog ports and eight digital inputs and outputs. The maximum output rate is one kilosample per second (1 ms per time step) [62].

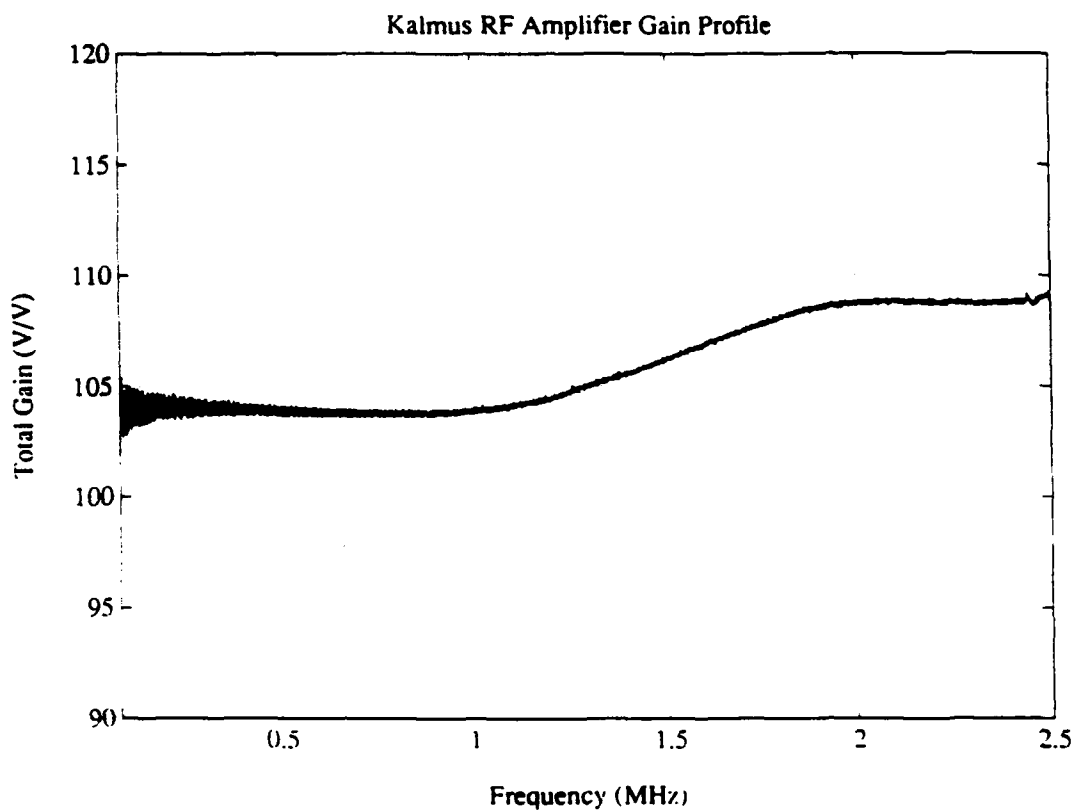


Figure 61. RF Amplifier Gain Profile. The rated bandwidth is 100 MHz; only the frequency range relevant to normal FTMS operation is displayed.

Within FTMS, the DAC is a multitask device (see Figure 60). Ports 1 and 2 drive the front and rear traps, port 3 pulses the electron gun (by adding 10 volts to the gun high voltage reference) and port 4 triggers the AFG (ion excitation). In this manner, the DAC becomes the FTMS timing device. The DAC also creates the potential well which, in conjunction with the strong magnetic field, traps the ions.

Ion Detection

FTMS would not exist if charged particles traveling near a conductor did not induce an image current on the conductor. This image current, induced differentially on the detect plates, is the primary observable. The image current is amplified and recorded.

Spectral peaks in the waveform's frequency domain represent system noise or ion cyclotron frequencies (or harmonics). Since the cyclotron frequency is unambiguously related to the ion mass ($\omega_c = \frac{qB}{m}$), the ion mass can be deduced from the power spectrum. Examples of time domain and frequency domain data acquisitions are shown in Figures 26 and 27. The detection hardware schematic is shown in Figure 62.

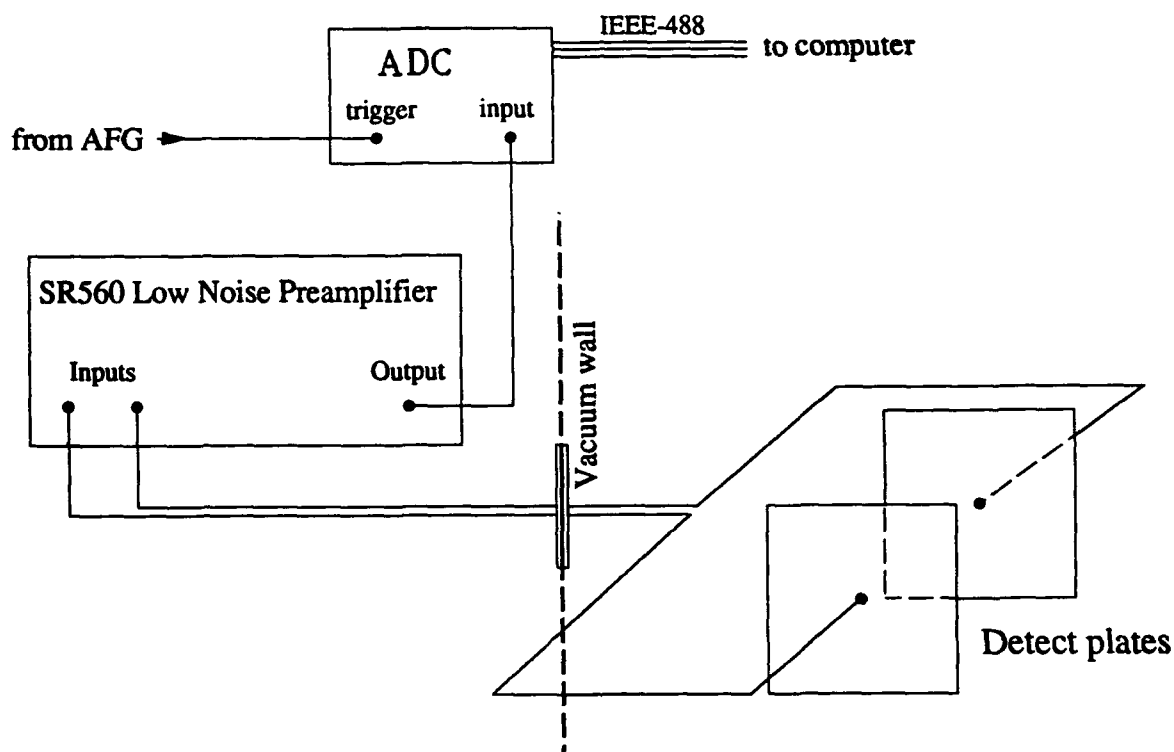


Figure 62. Detection Electronics Schematic

Differential Preamplifier. The preamplifier is model SR560, made by Stanford Research Systems. It provides AC or DC coupled low-noise amplification of single or true differential input signals. The gain may be set from 1 to 50000 V/V. Configurable RC filters provide selective conditioning in low-pass, mid-pass or high-pass modes from DC to 1 MHz [124].

The nominal input impedance is 100 M Ω in parallel with 25 pf. For all FTMS frequencies (*i.e.*, above 20 kHz) the preamplifier has a dominantly capacitive input impedance.

There are approximately 60 cm of coaxial cable connecting the detect plates to the preamplifier, with a measured capacitance of 76.8 ± 0.3 pf. The preamp inputs overload at 1 VDC, but are protected to 100 VDC (ICR signals are in the μV range, but detect plate pick-up of the rf excitation can be in the volt range).

An internal battery pack allows for elimination of noise from AC line power. The battery pack was generally not used. The preamplifier is rated for noise less than $4 \text{ nV/Hz}^{1/2}$ at 1 kHz. The bandwidth is rated to be at least 1 MHz [124], which is substantially lower than the original FTMS-1000 preamplifier (3 MHz).

For the data reported in this dissertation, the preamplifier was always configured with DC coupling, a gain of 5000 V/V, and a high pass filter at 10 KHz (12 dB/octave) Using SWIFT waveforms, a preamplifier gain calibration was performed. As shown in Figure 63, the bandwidth was close to 1.5 MHz. The calibration also showed that the bandwidth suffers with larger input signals, due to the slew rate limit of $5 \text{ V}/\mu\text{s}$ [4]. This provided additional motivation (along with space charge effects) to keep the number of ions well below 10^5 . The high pass filter is used to eliminate low frequency ringing, allowing ICR signals to be acquired as early as $50 \mu\text{s}$ after excitation (although $100 \mu\text{s}$ was typical).

Signal Acquisition. ICR signal acquisition of the preamplifier output was performed by several different analog-to-digital convertors (ADC's). The decision on which ADC to use was based on the resolution and sampling rate required.

The LeCroy model 6810 Waveform Recorder provided the highest resolution. This digitizer is a true 12-bit recorder with the capability to measure signals from DC to 2.5 MHz (five megasamples/second). It has four differential inputs (AC or DC coupled) with full scale ranges from 400 mV to 100 V. A 512 kilobyte memory (which could be expanded to 8 megabytes) permits 100 ms of continuous data to be recorded at a 2.5 MHz Nyquist frequency. Triggering may be performed externally, internally or over the bus [80].

The 6810 digitizer resides in a LeCroy model 8013A CAMAC crate. This IEEE-583 standard crate has room for 11 single-slot modules and one mainframe controller [81]. The mainframe controller is a model 6010 Magic Controller, by LeCroy. It is a general purpose

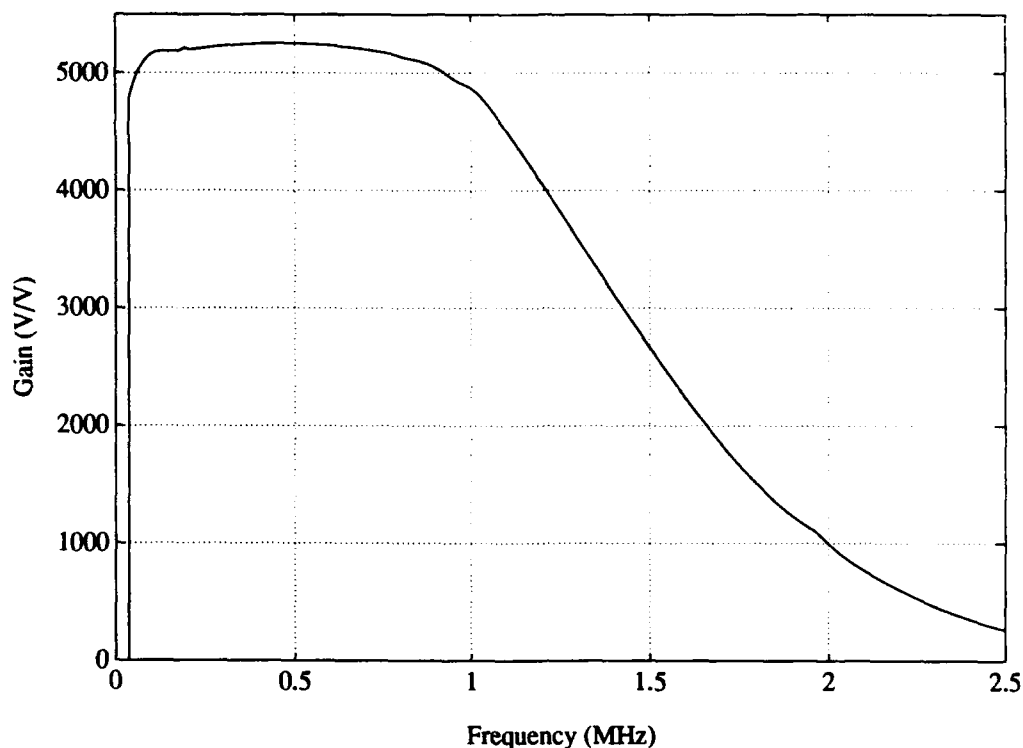


Figure 63. Preamplifier Gain Profile. The bandwidth is 1.5 MHz. The sharp cut-off at low frequency is associated with the plot and is not the actual response

GPB (IEEE-488) to CAMAC interface used to send standard CAMAC commands to the 6810 from the FTMS computer over a GPB bus [79].

The 6810 digitizer has several disadvantages for cross section measurements. The AFG provides an external trigger accurate to ± 4 ns, but because the 6810 5 MHz clock is not slaved to the AFG, there is acquisition trigger jitter of up to ± 100 ns. The 6810 controller has software which permits fast averaging of 8–8192 points of 6810 output, but longer waveforms must be averaged in the computer, which requires time consuming data transfers over the bus. The maximum sampling rate is only five megasamples/second, preventing oversampling of low mass ions. The sampling rate limitation coupled with the trigger jitter results in serious degradation of the low mass (high frequency) signals.

The LeCroy 9400 series oscilloscopes were used for higher sampling rates. Besides have bandwidths ranging from 100 MHz (models 9400 and 9410) to 350 MHz (models 9430 and 9450), which completely eliminated trigger jitter, the scopes could provide fast averaging on longer waveforms (10,000 long on the 9410 and 50,000 long on the 9430 and 9450).

The disadvantage of the scopes was the vertical resolution (8-bit A/D for the 9410 and 9540, 10-bit for the 9430) and the somewhat slow ASCII transfer of data over the bus. Binary transfers were avoided because they were model specific and required A/D gain corrections after the transfer.

Traditionally, FTMS has been applied to achieve ultra high mass resolution for molecular mass identification, which requires long acquisition times. Since this cross section and kinetics work involved well known reactants and products, mass identification was a cursory issue. For most experiments the sampling rate and trigger stability were the dominant concern, so the 9400 series scopes were generally used as the ADC instead of the 6810 digitizer.

Computer

The most significant improvement over the original FTMS-1000 system was replacement of the computer with a Sun Microsystems SPARCstation 1 workstation [125]. The SPARCstation is presently configured with 16 Mb of RAM and has a 300 Mb hard drive. There is long term flexibility for improved computing capability; the present configuration is transparent to upgrades to the more recent SPARC designs (such as the SPARCstation 2).

Bus Communication. The SPARCStation communicates with AFG, DAC and the ADC's via an IEEE-488 bus. Interfacing occurs within an IOtech model SB488 SBus card [63]. Data retrieval is specific to the ADC. A "read back" request retrieves binary data from the 6810, while an "inspect" query retrieves ASCII data from the 9400 series scopes. DAC files are loaded over the bus and executed by a "group execute" trigger, which fires all four ports at the same instant.

Data Processing. All data processing was performed using PRO-MATLAB, developed by The MathWorks. MATLAB ("matrix laboratory") is a high performance interactive software package for scientific and engineering numeric computation [90]. The MATLAB fast-fourier transform (FFT) algorithm performs a 16k complex FFT in about two seconds (real time); a 256k long transform takes about 18 seconds. This is drastically better performance than a recently described PC-equipped FTMS [46], which took 50 seconds to handle a 16k transform. Processing times are even shorter on the SPARCstation 2 workstations available at AFIT, where data processing was also performed.

Excitation Waveform Generation. Since its inception, many types of excitation waveforms have been used for FTMS ion excitation. Sinusoidal excitation is optimal for single mass-types because it has the minimum off-resonance excitation. Early experiments [25, 26] used a rapid rf sweep, or "chirp", excitation to simultaneously excite variety of mass types. Because chirp excitation has a nonuniform power spectrum, a tailored excitation labelled "stored waveform inverse Fourier transform", or SWIFT, was developed [21, 45, 47, 88, 137]. SWIFT is constructed by taking a flat power spectrum, applying a quadratic phase function and taking the inverse Fourier transform to determine the time domain rf excitation. Recently, "impulse" excitation was proposed as an alternative wideband excitation [93, 94]. Impulse excitation is a large rectangular pulse of several hundred volts for several hundred nanoseconds. Subsequent analysis [136] has shown impulse excitation has a limited range of uniformity—light ions are not excited as efficiently.

This work used sinusoidal rf excitation for single species excitation. Since SWIFT has been shown to be superior to chirp excitation [21, 56], SWIFT was used exclusively for wideband rf excitation. The SWIFT algorithm was written in MATLAB after the useful work by Guan [45, 47], and is included in Appendix B.

Once they are created within MATLAB, excitation waveforms are saved as ASCII formatted files. Post processing is performed to create a format acceptable to the AFG. Waveforms are loaded into the 512kbyte AFG memory via the IEEE-488 bus, from where they can easily be output.

Summary

A hardware summary of the present FTMS apparatus is provided in Tables 18 and 19. Users familiar with the FTMS-1000 capabilities will note an improvement in most performance specifications. Some typical operating parameters for resonant sinusoidal excitation are also noted.

Table 18. Hardware and Typical Parameters, Part 1

<i>Device</i>	<i>Characteristics</i>
Vacuum system	Oil-free, redundant system —Cryopump —Turbomolecular pump
DAC	Primary timing device —up to 1 kHz output rate Four isolated DAC outputs —trapping voltages of -10 to $+10$ V —electron gun trigger —AFG trigger (rf excitation) IEEE-488 interface
AFG	12-bit output 100 μ V–5 V output (full scale) —100 mV output (typical) 25 MHz Nyquist frequency (max) —10 MHz Nyquist (typical) Encoded digital trigger to ADC —accurate to ± 4 ns IEEE-488 interface
RF amps	Inverted matched pair 100 MHz bandwidth Total gain of 106 ± 3 V/V 500 V output (max) —10 V output (typical)
Electron Gun	10–1000 eV rated energy 1 nA – 3 μ A Mounted ~ 100 cm from ion trap Energy dispersion is small —0.2 eV plus space charge well

Table 19. Hardware and Typical Parameters, Part 2

<i>Device</i>	<i>Characteristics</i>
Preamplifier	Programmable gain, up to 5×10^4 V/V Programmable low and/or high pass filtering Low noise Differential or single-ended amplification mode Modest bandwidth (1.5 MHz)
ADC	Waveform recorder —12-bit —up to 256k data points —2.5 MHz Nyquist frequency —Internal CAMAC interface —IEEE-488 interface Oscilloscope —8-bit —up to 50,000 data points —up to 50 MHz Nyquist frequency —IEEE-488 interface
Computer	Sun SPARCstation 1 —16 Mb memory —300 Mb hard drive PRO-MATLAB software package IEEE-488 interface card

Appendix B. Software Algorithms

This chapter provides copies of the key algorithms written during this research relating to SWIFT excitation and the ion trajectory and image current simulations. All software was written to operate within MATLAB [90], but could easily be converted to FORTRAN.

SWIFT Excitation Algorithm

The algorithm for creating a SWIFT excitation is actually a two step process. First the requested power spectrum, in the frequency domain, is established by running function MAG. The output from MAG then becomes the input for function SWIFT1.

MAG.M:

```
function pk=mag(fi,ff,nchan,scale)
%mag(fi,ff,nchan,scale) creates a square wave pulse in frequency
% domain over an input (MHz) range in 'nchan' channels
% fi = the lower frequency (Hz)
% ff = the upper frequency (Hz)
% nchan = number of channels
% (must be even number; mod(2) preferred)
% scale = the amplitude of the pulse (V/Hz)
freq=input('What is the Nyquist frequency in MHz?');
freq=freq*2e6;
% ('freq' and 'num' are the total freq range and
% number of channels)
f=zeros(nchan,1);
delta=freq/nchan
% Treat the left half plane as positive frequencies and
% the right half plane as negative frequencies so that the
% Nyquist frequency is 'freq/2' and it falls in
% channel '(nchan/2)+1'.
il=round(fi/delta)
ih=round(ff/delta)
f(il:ih)=ones(ih-il+1,1);
% Calculate the x-axis units in MHz.
xf=(1:nchan/2)*freq/(1e6*2*(0.5*nchan+1));
plot(xf,f(1:nchan/2)*scale)
title('Magnitude spectrum, F(v)')
xlabel('Frequency (MHz)')
```

```

ylabel('Magnitude (V-sec)')
grid
pk=f*scale;

```

SWIFT1.M:

```

function ft = swift(f,num,fl,fh)
%swift(f,num,fl,fh) computes the time domain excitation signal
%   for an input magnitude spectrum 'f'
%   f = magnitude spectrum vector (V/Hz) [input from MAG]
%   num = # of elements in vector 'f' (i.e., # of channels)
%   fl = lowest non-zero frequency in 'f'
%   fh = highest non-zero frequency in 'f'
%
%   ft = time domain signal created in this Function
%   From Guan and McIver, J.Chem.Phys., 92:5841, 1990.
start=1
% 'freq' is the Nyquist frequency.
freq=input('What is the Nyquist frequency in MHz?');
freq=freq*1e6;
% 'num' is the no. of elements in vector 'f'
% For the organization (frequency tagging) of vector 'f',
% see notes in function MAG.
%
% 'delta' is the frequency (Hz) per bin
delta=freq/(0.5*num+1)
% Calculate the x-axis in units of MHz
xf=(1:num/2)*freq/(1e6*(0.5*num+1));
plot(xf,f(1:num/2))
title('Input magnitude spectrum')
xlabel('Frequency (MHz)')
ylabel('Magnitude spectrum (V-sec)')
grid
% 'ichanl' and 'ichanh' track the lowest and highest non-zero
% bins in the frequency domain.
ichanl=round(fl/delta)
ichanh=round(fh/delta)
% compute dynamic range, no modulation
drno=delta*(sum(f)-0.5*(f(1)+f(num)))
% 'drreq'=dynamic range, required (volts)
drreq=input('Enter the dynamic range available (volts)');
rat=drno/drreq
% compute minimum time for time domain pulse
t=(1.17*rat)^2/(fh-fl)
t=input('Enter desired min time');
start=2

```

```

%---perform filtering on data-----
% specify the number of filters
m=input('Enter desired number of filters');
% specify the filtering bandwidth (Hz)
deltaw=input('Enter desired filter bandwidth (Hz)');
if deltaw > freq
    m=0
end
k=round(0.5*deltaw/delta)
plot(f(ichanl-k:ichanh+k))
if m > 0
    for j=1:m
        il1=ichanl-j*k-1
        if il1 < 1
            il1=1;
        end
        ih1=ichanh+j*k+1
        if ih1 > num/2
            ih1=num/2;
        end
% Test to ensure filtering doesn't exceed array dimensions
        for i=il1:ih1
            ik1=i-k;
            ik2=i+k;
            if ik1 < 1
                ik1=1;
            end
            if ik2 > num/2
                ik2=num/2;
            end
            ff(i)=(sum(f(ik1:ik2))-0.5*(f(ik1)+f(ik2)))/(2*k);
        end
        plot(ff(il1:ih1))
        f(il1:ih1)=ff(il1:ih1);
    end
end
f=f';
plot(xf,f(1:num/2))
title('Filtered Magnitude Spectrum')
xlabel('Frequency (MHz)')
ylabel('Magnitude spectrum (V-sec)')
% specify truncation point: 'eta' times below max(f)
eta=2047;
%expanded window size (reduces power leakage)
t1=t+2*(eta*t^0.5/(1.17*2*pi*sqrt(fh-fl)*(deltaw*pi)^m))^(1/(m+1))

```

```

t1=input('Enter desired time window')
t0=(t1-t)/2
start=3
%---begin phase function calculation---
g=f.^2;
plot(xf,g(1:num/2))
title('Power Distribution')
xlabel('Frequency (MHz)')
ylabel('Magnitude (V^2-sec^2)')
gsum=0;
gxsum=0;
denom=delta*(sum(g(1:ichanh+m*k+1))-0.5*(g(1)+g(ichanh+m*k+1)));
for i=1:num
    if i < ichanh+m*k+1
        gsum=gsum+g(i);
        gx(i)=delta*(gsum-0.5*(g(1)+g(i)));
        gxsum=gxsum+gx(i);
        gy=delta*(gxsum-0.5*(gx(1)+gx(i)));
    end
    shift=2*pi*i*delta*t0;
    % Assume the initial phase (P0) is zero
    p(i)=shift+gy*(t1-t0)/denom;
end
start=4
plot(p)
title('Phase Function');
xlabel('Channel number');
% Perform inverse fourier transform
j=sqrt(-1);
omeg=f.*exp(p*j);
ftemp=ifft(omeg);
% calculate the time step
del=1/(2*freq)
% Perform the normalization.
% the sqrt of 2 must be included to account for the "positive"
% and "negative" frequencies.
ftemp=ftemp*sqrt(2)/del;
xt=(0:num-1)*del;
plot(xt,abs(ftemp))
title('Magnitude in time domain')
xlabel('Time (sec)')
ylabel('Amplitude (volts)')
%ftemp=real(ftemp);
plot(xt,real(ftemp))
title('Time domain signal')

```

```

xlabel('Time (sec)')
ylabel('Amplitude (volts)')
grid
% Compute the peak voltage required
peakv=max(abs(real(ftemp)))
ft(:)=ftemp;

```

Ion Trajectory Simulation

The following algorithms were used to compute ion trajectories in a cubic ion cell. The main routine is called TRAJ5; it calls functions VEXCTIME and EFIELD.

TRAJ5.M:

```

function [x,y,z,vx,vy,vz,rperp,en,tej]=traj5(x0,v0,vtrap,vtim,ddt)
% [x,y,z,vx,vy,vz,rperp,en,tej]=traj5(x0,v0,vtrap,vtim,ddt)
% performs a trajectory calculation using a 4th order
% Runge-Kutta method for an ion with an initial position
% vector x0 and velocity vector v0 and returns the position,
% the radius perpendicular to the magnetic field and the
% kinetic energy for each time step, along with the
% time of ejection (if applicable).
%
% x0=initial position [x(0),y(0),z(0)]
% --each value between 0 and 1 (normalized to trap length)
% v0=initial velocity [vx(0),vy(0),vz(0)] in m/sec
% vtrap=voltage on trapping plates in volts
% vtim=voltage on excitation plates in volts
% ddt=delta time step in excitation file (vtim)
i=1;
tej=-1;
% Written by Capt Kevin Riehl, Air Force Institute of Technology.
% Edited by Kevin Riehl, Lior Pachter.
% Last Edit: 3 Apr 92, by K.R.
x0
% "b" is the magnetic field (in tesla)
% The most recently computed experimental value is ...
b=1.98024;
% "q" is the ion charge (in coulombs)
zz=input('What is the ion charge state (+1, +2, etc)?')
q=zz*1.6022e-19;
% "m" is the ion mass (in kg)
m=input('What is the ion mass (in amu)?')
m=m*1.66043e-27;

```



```

% "wc" is the cyclotron frequency
wc=q*b/m
deltat=input('What time step size do you want (in sec)?')
po=ddt*(length(vtim)/deltat);
% "wct" is the characteristic numerical rotation
wct=wc*deltat
% "deltaa" is the gap between the length of the cell and
% the edge of the plate.
deltaa=input('What is the gap between plates (in cm)?');
deltaa=deltaa/sqrt(2)
% Dimension variables to vectorize
po=ddt*(length(vtim)/deltat);
po=round(po);
time=zeros(po,1);
x=zeros(po,1);
y=zeros(po,1);
z=zeros(po,1);
vx=zeros(po,1);
vy=zeros(po,1);
vz=zeros(po,1);
x(i)=x0(1);
y(i)=x0(2);
y(i)=x0(2);
z(i)=x0(3);
vx(i)=v0(1);
vy(i)=v0(2);
vz(i)=v0(3);
time(i)=0;
% Make sure the time domain excitation file, "vtim", is
% formatted as a nx1 matrix
dim=length(vtim);
tend=(dim-round(deltat/ddt+1))*ddt
% BEGIN INTEGRATION
while time(i)<tend
    i=i+1
    if i==10000
        save trajouttmp
    end
    vtime=feval('vexctime',time(i-1),vtim,ddt);
    [ex,ey,ez]=feval('efield',x(i-1),y(i-1),z(i-1),vtrap,vtime,deltaa);
    k11=vx(i-1)*deltat;
    k12=vy(i-1)*deltat;
    k13=vz(i-1)*deltat;
    k14=wc*(ex/b+vy(i-1))*deltat;
    k15=wc*(ey/b-vx(i-1))*deltat;

```

```

k16=wc*(ez/b)*deltat;
%
tdum=time(i-1)+deltat/2;
vtime=feval('vexctime',tdum,vtim,ddt);
xdum=x(i-1)+k11/(2*0.05);
ydum=y(i-1)+k12/(2*0.05);
zdum=z(i-1)+k13/(2*0.05);
[ex,ey,ez]=feval('efield',xdum,ydum,zdum,vtrap,vtime,deltaa);
k21=(vx(i-1)+k14/2)*deltat;
k22=(vy(i-1)+k15/2)*deltat;
k23=(vz(i-1)+k16/2)*deltat;
k24=wct*(ex/b+vy(i-1)+k15/2);
k25=wct*(ey/b-vx(i-1)-k14/2);
k26=wct*(ez/b);
%
xdum=x(i-1)+k21/(2*0.05);
ydum=y(i-1)+k22/(2*0.05);
zdum=z(i-1)+k23/(2*0.05);
[ex,ey,ez]=feval('efield',xdum,ydum,zdum,vtrap,vtime,deltaa);
k31=(vx(i-1)+k24/2)*deltat;
k32=(vy(i-1)+k25/2)*deltat;
k33=(vz(i-1)+k26/2)*deltat;
k34=wct*(ex/b+vy(i-1)+k25/2);
k35=wct*(ey/b-vx(i-1)-k24/2);
k36=wct*(ez/b);
%
time(i)=time(i-1)+deltat;
vtime=feval('vexctime',time(i),vtim,ddt);
xdum=x(i-1)+k31/0.05;
ydum=y(i-1)+k32/0.05;
zdum=z(i-1)+k33/0.05;
[ex,ey,ez]=feval('efield',xdum,ydum,zdum,vtrap,vtime,deltaa);
k41=(vx(i-1)+k34)*deltat;
k42=(vy(i-1)+k35)*deltat;
k43=(vz(i-1)+k36)*deltat;
k44=wct*(ex/b+vy(i-1)+k35);
k45=wct*(ey/b-vx(i-1)-k34);
k46=wct*(ez/b);
% calculate the new velocity
vx(i)=vx(i-1)+(k14+2*k24+2*k34+k44)/6;
vy(i)=vy(i-1)+(k15+2*k25+2*k35+k45)/6;
vz(i)=vz(i-1)+(k16+2*k26+2*k36+k46)/6;
% calculate change in position in S.I. units
deltax=(k11+2*k21+2*k31+k41)/6;
deltay=(k12+2*k22+2*k32+k42)/6;

```

```

    deltaz=(k13+2*k23+2*k33+k43)/6;
% calculate the new position in scaled units
    x(i)=x(i-1)+deltax/0.05;
    y(i)=y(i-1)+deltay/0.05;
    z(i)=z(i-1)+deltaz/0.05;
% test for ejection
    if abs(round(x(i)-0.5)) > 0
        tej=time(i)
        time(i)=tend;
    end
    if abs(round(y(i)-0.5)) > 0
        tej=time(i)
        time(i)=tend;
    end
    if abs(round(z(i)-0.5)) > 0
        tej=time(i)
        time(i)=tend;
    end
end
% perform change of coordinate so the center of the cubic
% trap is at (0,0,0) and x,y,z are in cm
x=(x-0.5)*5;
y=(y-0.5)*5;
z=(z-0.5)*5;
% Compute to radial distance to the origin (0,0,0) perpendicular
% to the magnetic field.
rperp=sqrt((x-x(1)).^2+(y-y(1)).^2);
% Compute the kinetic energy (in eV).
en=0.5*m*(vx.^2+vy.^2+vz.^2)/1.6022e-19;

```

VEXCTIME.M:

```

function vtime=vexctime(t,vtim,dt)
% vexctime(t,vtime,dt) looks up the instantaneous
% excitation voltage.
index=round(t/dt-0.5)+1;
if t/dt <= 0
    index=1
end
vtime=vtim(index);

```

EFIELD.M:

```

function [ex,ey,ez]=efield(x,y,z,vtrap,vtime,deltaa)
% [ex,ey,ez]=efield(x,y,z,vtrap,vtime,deltaa) computes
% the components of the electric field at a

```

```

%    given position for given boundary conditions
%    in a cubic trap.
%
%    (x,y,z)=instantaneous position
%    vtrap=trapping voltage
%    vtime=instantaneous excitation voltage
%    deltaa=gap between length of trap side and plate
ex=0;
ey=0;
ez=0;
side=0.05;
% test for location so as to model the electric
% field to four significant figure accuracy.
cox=[4.316e4 -1.7793e5 3.184e5 -3.2124e5 1.9871e5 -7.6813e4 ...
      1.8225e4 -2.5089e3 1.7503e2];
xm=polyval(cox,y);
xmn=2*round(xm/2)+3;
if xmn < 5
    xmn=5
end
if xmn > 151
    xmn=151
end
%
coy=[1.3973e5 -5.5808e5 9.3601e5 -8.5653e5 4.652e5 -1.5279e5 ...
      2.9651e4 -3.188e3 1.6861e2];
ym=polyval(coy,y);
ymn=2*round(ym/2)+3;
if ymn < 5
    ymn=5
end
if ymn > 151
    ymn=151
end
%
coz=[1.3973e5 -5.5808e5 9.3601e5 -8.5653e5 4.652e5 -1.5279e5 ...
      2.9651e4 -3.188e3 1.6861e2];
zm=polyval(coz,z);
zmn=2*round(zm/2)+3;
if zmn < 5
    zmn=5
end
if zmn > 151
    zmn=151
end
end

```

```

% test to see which direction requires the most terms
if zmn > ymn
    iup=zmn;
else
    iup=ymn;
end
if xmn > iup
    iup=xmn;
end
% Initialize arrays
alp=zeros(iup,1);
bet=zeros(iup,1);
gam=zeros(iup,iup);
a=zeros(iup,iup);
exmn=zeros(xmn,xmn);
eymn=zeros(ymn,ymn);
ezmn=zeros(zmn,zmn);
%
for m=1:2:iup,
    for n=1:2:iup,
        alp(n)=n*pi;
        bet(m)=m*pi;
        gam(m,n)=pi*sqrt(n^2+m^2);
        a(m,n)=4*vtrap*(1-cos(alp(n)))*(1-cos(bet(m)))*cos(alp(n)*...
            deltaa/5)*cos(bet(m)*deltaa/5)/(m*n*pi^2*sinh(gam(m,n)));
    end
end
for m=1:2:xmn,
    for n=1:2:xmn,
        etrapx=sin(bet(m)*y)*(sinh(gam(m,n)*z)+sinh(gam(m,n)*(1-z)));
        eexcx=vtime*sin(bet(m)*z)*(sinh(gam(m,n)*y)-sinh(gam(m,n)*...
            (1-y)))/vtrap;
        exmn(m,n)=-a(m,n)*alp(n)*cos(alp(n)*x)*(etrapx+eexcx)/side;
        ex=ex+exmn(m,n);
    end
end
for m=1:2:ymn,
    for n=1:2:ymn,
        etrapy=bet(m)*cos(bet(m)*y)*(sinh(gam(m,n)*z)+sinh(gam(m,n)*...
            (1-z)))/side;
        eexcyc=vtime*sin(bet(m)*z)*gam(m,n)*(cosh(gam(m,n)*y)+...
            cosh(gam(m,n)*(1-y)))/(side*vtrap);
        eymn(m,n)=-a(m,n)*sin(alp(n)*x)*(etrapy+eexcyc);
        ey=ey+eymn(m,n);
    end
end

```

```

end
for m=1:2:zmn,
    for n=1:2:zmn,
        etrapz=sin(bet(m)*y)*gam(m,n)*(cosh(gam(m,n)*z)-...
            cosh(gam(m,n)*(1-z)))/side;
        eexcZ=vtime*bet(m)*cos(bet(m)*z)*(sinh(gam(m,n)*y)-...
            sinh(gam(m,n)*(1-y)))/(side*vtrap);
        ezmn(m,n)=-a(m,n)*sin(alp(n)*x)*(etrapz+eexcZ);
        ez=ez+ezmn(m,n);
    end
end
end

```

Image Current Simulation

The following algorithms compute the image current. The ion trajectory which was output from TRAJ5 serves as the input to the main routine IMAGE; EFIELDDIMAGE is called as a function.

IMAGE.M:

```

function [i1,i2,itot]=image(x,y,z,vx,vy,vz,da,ch);
% function [i1,i2,itot]=image(x(t),y(t),z(t),vx(t),vy(t),vz(t),da,ch)
% returns the current i(t) in amps induced on plates 1 and 2 and
% the total image current (=i1-i2).
%
% i1 ---> image current on plate 1
% i2 ---> image current on plate 2
% itot ---> total image current (i1-i2)
% (x,y,z) ---> co-ordinates as a function of time (-2.5 to 2.5 cm)
% (vx,vy,vz) ---> velocities as a function of time in m/s
% da ---> end plate gap (in cm)
% ch ---> charge/ion (+1,+2...)
%
% Calls EFIELDDIMAGE.M as subroutine
len=length(x);
% Written by Lior Pachter, SOCHE
% Edited by Lior Pachter, Kevin Riehl
% Last Edit: 1 Nov 91, by K.R.
i1=zeros(len,1);
i2=zeros(len,1);
itot=zeros(len,1);
% Normalize x,y,z from (0 --- 1)
x=x/5+0.5;
y=y/5+0.5;

```

```

z=z/5+0.5;
% Calculation of current begins here
for t=1:len
    [ex,ey,ez]=feval('efieldimage',x(t),y(t),z(t),da,1);
    i1(t)=ch*1.6022e-19.*(ex*vx(t)+ey*vy(t)+ez*vz(t));
    [ex,ey,ez]=feval('efieldimage',x(t),y(t),z(t),da,2);
    i2(t)=ch*1.6022e-19.*(ex*vx(t)+ey*vy(t)+ez*vz(t));
end
itot=i1-i2;

```

EFIELDIMAGE.M:

```

function [ex,ey,ez]=efieldimage(x,y,z,da,plate)
% [ex,ey,ez]=efieldimage(x,y,z,da,plate) computes the normalized
% (with respect to arbitrary applied potential V) electric
% field components for computation of the induced image
% current on the given plate.
%
% (x,y,z) should be normalized from 0-1 (trap ctr: 0.5,0.5,0.5)
% da ---> end plate gap (in cm)
% plate=1 ---> detect plate at (1,Y,Z)
% plate=2 ---> detect plate at (0,Y,Z)
a=5;
ex=0;
ey=0;
ez=0;
% Written by Capt Kevin Riehl, Air Force Institute of Technology
% Edited by Kevin Riehl
% Last Edit: 19 May 92, by K.R.
side=0.05;
% Specify the number of terms to sum over
pos=y;
co=[1.3973e5 -5.5808e5 9.3601e5 -8.5653e5 4.652e5 -1.5279e5 ...
    2.9651e4 -3.188e3 1.6861e2];
term=polyval(co,pos);
term=2*round(term/2)+3;
if term < 13
    term=13;
end
if term > 151
    term=151;
end
a=zeros(term,term);
alp=zeros(term,1);
bet=zeros(term,1);
gam=zeros(term,term);

```

```

for m=1:2:term,
    for n=1:2:term,
        alp(n)=n*pi;
        bet(m)=m*pi;
        gam(m,n)=sqrt(alp(n)^2+bet(m)^2);
        a(m,n)=4*(1-cos(bet(m)))*(1-cos(alp(n)))*cos(alp(n)*da/(side*100))*...
            cos(bet(m)*da/(side*100))/(n*m*pi^2*sinh(gam(m,n)));
    end
end
if plate==1
    for m=1:2:term,
        for n=1:2:term
            eexcx=sin(bet(m)*y)*sin(alp(n)*z)*gam(m,n)*cosh(gam(m,n)*x)/side;
            ex=ex-a(m,n)*eexcx;
            eexcy=cos(bet(m)*y)*sin(alp(n)*z)*bet(m)*sinh(gam(m,n)*x)/side;
            ey=ey-a(m,n)*eexcy;
            eexcZ=sin(bet(m)*y)*cos(alp(n)*z)*alp(n)*sinh(gam(m,n)*x)/side;
            ez=ez-a(m,n)*eexcZ;
        end
    end
end
end

```


Bibliography

1. Alajajian, S.H., et al. "Electron Attachment Line Shapes, Cross Sections, and Rate Constants at Ultralow Energies in CF_3SO_3H , $(CF_3SO_2)_2O$, and CF_3I ," *Journal of Chemical Physics*, 94:3629-3632 (March 1978).
2. Alcatel Vacuum Products, Hingham, Massachusetts. *Molecular Drag Pump MDP 5010*, 1988.
3. Alcatel Vacuum Products, Hingham, Massachusetts. *Turbomolecular Pumps and Turbopak Type 5150-5150CP with CFF 450 Turbo*, 1988.
4. Ames, Dave. Stanford Research Systems, Inc, March 1992. Private communication.
5. Bell, K.L., et al. "Ionisation of H^- by Electron Impact," *Journal of Physics B*, 11:2547-2553 (July 1978).
6. Beller, Denis. Air Force Institute of Technology, 1992. Private Communication.
7. Bely, O. and S.B. Schwartz. "Electron Detachment from H^- by Electron Impact," *Journal of Physics B*, 2:159-161 (February 1969).
8. Bensimon, Mike, et al. "A Method to Generate Phase Continuity in Two-Dimensional Fourier Transform Ion Cyclotron Resonance Mass Spectrometry," *Chemical Physics Letters*, 157:97-100 (April 1989).
9. Berman, D. Wayne, et al. "Ion Cyclotron Resonance and Photoionization Investigations of the Thermochemistry and Reactions of Ion Derived from CF_3I ," *International Journal of Mass Spectrometry and Ion Physics*, 39:47-54 (??? 1981).
10. Bevington, Philip R. and D. Keith Robinson. *Data Reduction and Error Analysis for the Physical Sciences* (2nd Edition). New York: McGraw-Hill, Inc, 1992.
11. Bieniek, Robert J. and A. Dalgarno. "Associative Detachment in Collisions of H and H^- ," *The Astrophysical Journal*, 228:635-639 (March 1979).
12. Boschi, Roberto Angelo Antonio and Dennis Russell Salahub. "The High Resolution Photoelectron Spectra of some Iodoalkanes, Iodocycloalkanes, Iodoalkenes, and Fluoroiodohydrocarbons," *Canadian Journal of Chemistry*, 52:1217-1228 (April 1974).
13. Brooks, Philip R. "Scattering of K Atoms from Oriented CF_3I ," *Faraday Discussions of the Chemical Society*, 55:299-306 (April 1973).
14. Bruce, M.R., et al. "Positive Ion Pair Production by Electron Impact Dissociative Ionization of CF_4 ," *Chemical Physics Letters*, 190:285-290 (March 1992).
15. Buchanan, Michelle V., editor. *Fourier Transform Mass Spectrometry*. Washington, D.C.: American Chemical Society, 1987.
16. Burden, Richard L. and J. Douglas Faires. *Numerical Analysis* (3rd Edition). Boston: Prindle, Weber and Schmidt, 1981.
17. Buss, R.J., et al. "Reactive Scattering of $O(^3P) + CF_3I$," *Journal of Physical Chemistry*, 87:4840-4843 (November 1983).

18. Bydin, I.F. and V.M. Dukelskii. "Electron Detachment from Negative Halogen Ions in Collisions with Inert-Gas Atoms and Hydrogen Molecules," *Soviet Physics JETP*, 4:474-481 (May 1957).
19. Champion, R.L. and L.D. Doverspike. "Collisional Detachment in Collisions of Cl^- With the Rare Gases," *Physical Review A*, 13:609-616 (February 1976).
20. Champion, R.L., et al. "Electron Detachment from Negative Ions: The Effects of Isotopic Substitution," *Physical Review A*, 13:617-621 (February 1976).
21. Chen, Ling, et al. "Phase-Modulated Stored Waveform Inverse Fourier Transform Excitation for Trapped Ion Mass Spectrometry," *Analytical Chemistry*, 59:449-454 (February 1987).
22. Chiarelli, M.P. and M.L. Gross. "Fourier Transform Mass Spectrometry for Chemical Analysis: A Brief Status Report." *Analytical Applications of Spectroscopy*, edited by C.S. Creaser and A.M.C. Davies. London: Royal Society of Chemistry, 1988.
23. Comisarow, Melvin B. "Signal Modelling for Ion Cyclotron Resonance," *Journal of Chemical Physics*, 69:4097-4104 (November 1978).
24. Comisarow, Melvin B. "Cubic Trapped-Ion Cell for Ion Cyclotron Resonance," *International Journal of Mass Spectrometry and Ion Physics*, 37:251-257 (February 1981).
25. Comisarow, Melvin B. and Alan G. Marshall. "Fourier Transform Ion Cyclotron Resonance Spectroscopy," *Chemical Physics Letters*, 25:282-283 (March 1974).
26. Comisarow, Melvin B. and Alan G. Marshall. "Frequency-Sweep Fourier Transform Ion Cyclotron Resonance Spectroscopy," *Chemical Physics Letters*, 26:489-490 (June 1974).
27. Compton, R.N., et al. "Collisional Ionization Between Alkali Atoms and Some Methane Derivatives: Electron Affinities for CH_3NO_2 , CF_3I , and CF_3Br ," *Journal of Chemical Physics*, 68:4360-4367 (May 1978).
28. CTI-Cryogenics. *Cryo-Torr High-Vacuum Pumps and Cryodyne Refrigeration Systems Powered by Model 8003 (with 8300 Compressor)*. Helix Technology Corporation, Waltham, Massachusetts, 1988.
29. Dalgarno, A., et al. "The Mobilities of Ions in Unlike Gases," *Philosophical Transactions of the Royal Society of London*, A250:411-425 (April 1958).
30. Dance, D.F., et al. "A Measurement of the Cross-Section for Detachment of Electrons from H^- by Electron Impact," *Proceedings of the Royal Society of London*, A299:525-537 (July 1967).
31. De Vreugd, C., et al. "Electron-Detachment in Differential $I^- + Ne$ Cross Section Measurements," *Chemical Physics Letters*, 64:175-177 (June 1979).
32. Demkov, Y.N. "Detachment of Electrons in Slow Collisions Between Negative Ions and Atoms," *Soviet Physics JETP*, 19:762-768 (September 1964).
33. Dotan, I. and D.L. Albritton. "Mobilities of F^- , Cl^- , Br^- , and I^- Ions in Argon," *Journal of Chemical Physics*, 66:5238-5240 (June 1977).

34. Dotan, I., et al. "Mobilities of F^- , Cl^- , Br^- , and I^- Ions in He ," *Journal of Chemical Physics*, 66:2232-2233 (March 1977).
35. Doucet, J., et al. "Vacuum Ultraviolet and Photoelectron Spectra of Fluoro-chloro Derivatives of Methane," *Journal of Chemical Physics*, 58:3708-3716 (May 1973).
36. Dunbar, Robert C. "The Effect of Ion Position on ICR Signal Strength," *International Journal of Mass Spectrometry and Ion Processes*, 56:1-9 (February 1984).
37. Gauyacq, Jean Pierre. *Dynamics of Negative Ions*. Singapore: World Scientific, 1987.
38. Geltman, S. "Electron Detachment from the Negative Hydrogen Ion by Electron Impact," *Proceedings of the Physical Society*, 75:67-76 (January 1960).
39. Gerck, Edgardo. "Quantum Yields of $I(^2P_{1/2})$ for CF_3I , C_2F_5I , $i-C_3F_7I$, $n-C_3F_7I$, $n-C_6F_{13}I$, and 1,2- $C_2F_4I_2$ at 308 and 248 nm," *Journal of Chemical Physics*, 79:311-315 (July 1983).
40. Goy, C.A., et al. "Kinetics and Thermodynamics of the Reaction between Iodine and Fluoroform and the Heat of Formation of Trifluoromethyl Iodide," *Journal of Physical Chemistry*, 71:1086-1089 (March 1967).
41. Granville-Phillips Company, Boulder, Colorado. *Instruction Manual 270013 000 for Series 270 Ionization Gauge Controllers*, 1980.
42. Gross, Michael L. and Don L. Rempel. "Fourier Transform Mass Spectrometry," *Science*, 226:261-268 (October 1984).
43. Grosshans, Peter B. and Alan G. Marshall. "Theory of Ion Cyclotron Resonance Mass Spectrometry: Resonant Excitation and Radial Ejection in Orthorhombic and Cylindrical Ion Traps," *International Journal of Mass Spectrometry and Ion Processes*, 100:347-379 (October 1990).
44. Grosshans, Peter B., et al. "Simple and Accurate Determination of Ion Translational Energy in Ion Cyclotron Resonance Mass Spectrometry," *Journal of the American Chemical Society*, 112:1275-1277 (January 1990).
45. Guan, Shenheng. "General Phase Modulation Method for Stored Waveform Inverse Fourier Transform Ion Cyclotron Resonance Mass Spectrometry," *Journal of Chemical Physics*, 91:775-777 (July 1989).
46. Guan, Shenheng and Patrick R. Jones. "Personal Computer Based Fourier Transform Ion Cyclotron Resonance Mass Spectrometer," *Reviews of Scientific Instruments*, 59:2573-2576 (December 1988).
47. Guan, Shenheng and Jr Robert T. McIver. "Optimal Phase Modulation in Stored Wave Form Inverse Fourier Transform Excitation for Fourier Transform Mass Spectrometry. I. Basic Algorithm," *Journal of Chemical Physics*, 92:5481-5846 (May 1990).
48. Haaland, Peter Donald. *Ion Kinetics in Silane Plasmas*. PhD dissertation, Harvard University, 1988.

49. Hanson, Curtiss D., et al. "Phase Synchronization of an Ion Ensemble by frequency Sweep Excitation in Fourier Transform Ion Cyclotron Resonance," *Analytical Chemistry*, 61:2130-2136 (October 1989).
50. Hanson, Curtiss D., et al. "Ion Detection by Fourier Transform Ion Cyclotron Resonance: The Effect of Initial Radial Velocity on the Coherent Ion Packet," *Analytical Chemistry*, 61:2040-2046 (September 1989).
51. Harland, Peter W., et al. "Electron Transfer to Oriented Molecules: $K + CF_3I$ and $K + CH_3I$," *Journal of Chemical Physics*, 93:1089-1097 (July 1990).
52. Hasegawa, Akinori and Ffrancon Williams. "ESR Spectra and Structure of the CF_3Cl^- , CF_3Br^- , and CF_3I^- Radical Anions," *Chemical Physics Letters*, 46:66-68 (February 1977).
53. Hasse, H.R. "Langevin's Theory of Ionic Mobility," *Philosophical Magazine and Journal of Science*, 1 (7th Series):139-160 (January 1926).
54. Hasted, J.B. "Inelastic Collisions Between Ions and Atoms," *Proceedings of the Royal Society of London*, A212:235-248 (April 1952).
55. Haywood, S.E., et al. "Electron Detachment in I^- -Rare-Gas Collisions," *Journal of Physics B*, 14:261-266 (January 1981).
56. Hearn, B.A., et al. "An Ion Trajectory Model for Fourier Transform Ion Cyclotron Resonance Mass Spectrometry," *International Journal of Mass Spectrometry and Ion Processes*, 95:299-316 (January 1990).
57. Heni, Martin and Eugen Illenberger. "Dissociative Electron Attachment to CF_3I : An Example of a Completely Unbalanced Excess Energy Distribution," *Chemical Physics Letters*, 131:314-318 (November 1986).
58. Holt, E.H. and R.E. Haskill. *Foundations of Plasma Dynamics*. New York: The Macmillan Company, 1965.
59. Hsieh, Tacheng, et al. "Ion-Molecule Reactions in Trifluoromethyl Iodide and Pentafluoroethyl Iodide," *International Journal of Mass Spectrometry and Ion Physics*, 28:113-128 (October 1978).
60. Illenberger, E. "Measurement of the Translational Excess Energy in Dissociative Electron Attachment Processes," *Chemical Physics Letters*, 80:153-157 (May 1981).
61. Inokuti, Mitio and Yong-Ki Kim. "Total Cross Sections for Inelastic Scattering of Charged Particles by Atoms and Molecules. II. Negative Hydrogen Ion," *Physical Review*, 173:154-160 (September 1968).
62. IOTech, Inc, Cleveland, Ohio. *DAC488 Instruction Manual*, 1989.
63. IOTech, Inc, Cleveland, Ohio. *SCSI488/S Instruction Manual*, 1989.
64. Jackson, J.D. *Classical Electrodynamics* (2nd Edition). New York: John Wiley and Sons, 1975.
65. Jarrold, Martin F., et al. "Photodissociation of Vibrationally Excited CF_3I^+ and CF_3Br^+ by a Single Infrared Photon," *Journal of Physical Chemistry*, 87:2213-2221 (June 1983).

66. Jeffries, J.B., et al. "Theory of Space-Charge Shift of Ion Cyclotron Resonance Frequencies," *International Journal of Mass Spectrometry and Ion Processes*, 54:169-187 (October 1983).
67. John, T.L. and B. Williams. "Coulomb Effects on Electron Negative Ion Detachment," *Journal of Physics B*, 6:L381-L383 (December 1973).
68. Johnston, Mark. "Fourier Transform—Mass Spectrometry, Part 1," *Spectroscopy*, 2(2):14-20 (February 1987).
69. Johnston, Mark. "Fourier Transform—Mass Spectrometry, Part 2," *Spectroscopy*, 2(3):14-20 (March 1987).
70. J.P.Gauyacq. "Theoretical Study of the Detachment Process in the Zero-Range Potential Approximation. H^- -He Collisions," *Journal of Physics B*, 13:4417-4439 (November 1980).
71. Kalmus Engineering International, Ltd, Woodinville, Washington. *Model 110LC Instruction Manual*, 1990.
72. Kapetanakos, C.A. and A. W. Trivelpiece. "Diagnostics of Non-Neutral Plasmas Using an Induced-Current Electrostatic Probe," *Journal of Applied Physics*, 42:4841-4847 (November 1971).
73. Kern, Jim. EXTREL FTMS, Inc, April 1992. Private communication.
74. Kimball Physics, Inc, Wilton, New Hampshire. *ELG-2A Electron Gun Instruction Manual*, 1986.
75. KNF Neuberger, Inc, Princeton, New Jersey. *100% Oil-Less Diaphragm Vacuum Pumps and Compressors for Continuous Industrial Duty*. Undated.
76. Lam, S.K., et al. "Electron Detachment in Low-Energy Collisions of H^- and D^- with He," *Physical Review A*, 9:1828-1839 (May 1974).
77. Lasertechnics, Inc, Albuquerque, New Mexico. *Lasertechnics Model 203B Pulsed Valve Driver Manual*. Undated.
78. Lawrence, Ernest O. and M. Stanley Livingston. "The Production of High Speed Light Ions Without the Use of High Voltages," *Physical Review*, 40:19-35 (April 1932).
79. LeCroy Corporation, Chestnut Ridge, New York. *Model 6010/6010A GPIB (IEEE-488) to CAMAC*, 1988.
80. LeCroy Corporation, Chestnut Ridge, New York. *Model 6810 Waveform Recorder*, 1988.
81. LeCroy Corporation, Chestnut Ridge, New York. *LeCroy CAMAC Instrument Mainframes: Models 8013A, 1434A, and 8025*, 1989.
82. LeCroy Corporation, Chestnut Ridge, New York. *Model 9112 Operator's Manual*, 1989.
83. Ledford, Edward B., et al. "Space Charge Effects in Fourier Transform Mass Spectrometry. Mass Calibration," *Analytical Chemistry*, 56:2744-2748 (December 1984).

84. Lifshitz, Chava and William A. Chupka. "Photoionization of the CF_3 Free Radical," *Journal of Chemical Physics*, 47:3439-3443 (November 1967).
85. Loesch, H.J. and A. Remscheid. "Brute Force in Molecular Dynamics: A Novel Technique for Measuring Steric Effects," *Journal of Chemical Physics*, 93:4779-4790 (October 1990).
86. Ma, Ce, et al. "Absolute Partial and Total Electron-Impact-Ionization Cross Sections for CF_4 from Threshold Up to 500 eV," *Physical Review A*, 44:2921-2934 (September 1991).
87. Marshall, Alan G. and Peter B. Grosshans. "Fourier Transform Ion Cyclotron Resonance Mass Spectrometry: The Teen Years," *Analytical Chemistry*, 63:215A-229A (February 1991).
88. Marshall, Alan G., et al. "Tailored Excitation for Fourier Transform Ion Cyclotron Resonance Mass Spectrometry," *Journal of the American Chemical Society*, 107:7893-7897 (December 1985).
89. Mason, Edward A. and Joseph T. Vanderslice. "Interaction Energy and Scattering Cross Sections of H^- Ions in Helium," *Journal of Chemical Physics*, 28:253-257 (February 1958).
90. The MathWorks, Inc, South Natick, Massachusetts. *PRO-MATLAB Users's Guide*, 1990.
91. McDowell, M.R.C. and J.H. Williamson. "Electron Detachment from H^- by Electrons," *Physics Letters*, 4:159-160 (April 1963).
92. McFarland, M., et al. "Flow-Drift Technique for Ion Mobility and Ion-Molecule Reaction Rate Constant Measurements. I. Apparatus and Mobility Measurements," *Journal of Chemical Physics*, 59:6610-6619 (December 1973).
93. McIver, Robert T., Jr, et al. "Theory of Impulse Excitation for Fourier Transform Mass Spectrometry," *International Journal of Mass Spectrometry and Ion Processes*, 89:343-358 (May 1989).
94. McIver, Robert T., Jr, et al. "Impulse Excitation for Fourier Transform Mass Spectrometry," *Analytical Chemistry*, 61:489-491 (March 1989).
95. McNamee, P.E., et al. "General Discussion," *Faraday Discussions of the Chemical Society*, 55:318 (April 1973).
96. MKS Instruments, Inc, Burlington, Massachusetts. *Instruction Manual for SRG-2 Spinning Rotor Gas Friction Vacuum Gauge*, 1985.
97. Morris, Robert. Geophysics Directorate, Phillips Laboratory, 1992. Private Communication; work accepted for publication.
98. Morris, Robert A., et al. "Reactions of Ar^+ with Halocarbons and of I^+ with CF_3I ," *Journal of Chemical Physics*, 97:173-179 (July 1992).
99. Morris, Robert A., et al. "Chemistry of CF_n^+ ($n=1-3$) Ions with Halocarbons," *Journal of Physical Chemistry*, 96:2597-2603 (March 1992).

100. Murray, Kermit K., et al. "Photoelectron Spectroscopy of the Halocarbene Anions HCF^- , $HCCl^-$, HCB^- , HCl^- , CF_2^- , and CCl_2^- ," *Journal of Chemical Physics*, 89:5442-5451 (November 1988).
101. Narain, Udit and N.K. Jain. "Electron Detachment Cross Sections of H^- ," *Journal of Physics B*, 9:917-921 (April 1976).
102. Noutary, Clemente Juan. "Mass Spectrometric Study of the Photoionization of Some Fluorocarbons and Trifluoromethyl Halides," *Journal of Research of the National Bureau of Standards*, 72A:479-485 (September 1968).
103. Okafo, Ernest N. and Eric Whittle. "The Kinetics of the Thermal Bromination of CF_3I . Determination of the Bond Dissociation Energy $D(CF_3I)$," *International Journal of Chemical Kinetics*, 7:273-285 (March 1975).
104. O'Malley, T.F. "Theory of Dissociative Attachment," *Physical Review*, 150:14-29 (October 1966).
105. Osborne, M.R., et al. "Electron Liberation from Negative Ions as a Means of Laser Preionization," *Journal of Applied Physics*, 65:5242-5245 (June 1989).
106. Pagnamenta, Antonio, et al. "Electron Degradation and Yields of Initial Products. III. Dissociative Attachment in Carbon Dioxide," *Journal of Chemical Physics*, 89:6220-6225 (November 1988).
107. Paulson, John. Geophysics Directorate, Phillips Laboratory, 1991. Private communication.
108. Peart, B., et al. "Measurements of Cross Sections for Detachment of Electrons from C^- and O^- Ions by Electron Impact," *Journal of Physics B*, 12:847-853 (March 1979).
109. Peart, B., et al. "Measurements of Detachment from F^- by Electron Impact and Tests of Classical Scaling for Electron Impact Detachment Cross Sections," *Journal of Physics B*, 12:L115-L118 (February 1979).
110. Peart, B., et al. "Electron Detachment from H^- Ions by Electron Impact," *Journal of Physics B*, 3:1346-1356 (October 1970).
111. Pleasance, L.D. and L.A. Weaver. "Laser Emission at $1.32 \mu m$ from Atomic Iodine Produced by Electrical Dissociation of CF_3I ," *Applied Physics Letters*, 27:407-409 (October 1975).
112. Powis, Ivan, et al. "Photoion Anisotropy in Dissociative Photoionization of CF_3I ," *Journal of Chemical Physics*, 92:1643-1652 (February 1990).
113. Press, William H., et al. *Numerical Recipes*. Cambridge: Cambridge University Press, 1986.
114. Prochaska, Frank T. and Lester Andrews. "Matrix Photoionization Studies of Trifluoromethyl Halide Systems. Infrared Spectra of the CF_3^+ , CF_2X^+ , and CF_3X^+ Cations in Solid Argon," *Journal of the American Chemical Society*, 100:2102-2108 (March 1978).

115. Ramo, Simon. "Currents Induced by Electron Motion," *Proceedings of the I.R.E.*, 27:584-585 (September 1939).
116. Rempel, D.L., et al. "Relationship of Signal Sensitivity and Ion z-Motion in Cubic Cells. Theory and Implications for Ion Kinetic Studies," *International Journal of Mass Spectrometry and Ion Processes*, 70:163-184 (June 1986).
117. Risley, J.S. and R. Geballe. "Absolute H^- Detachment Cross Sections," *Physical Review A*, 9:2485-2495 (June 1974).
118. Rothe, Erhard W., et al. "Anion Production from $Cs + CF_3X$: Evidence for Stripping," *Chemical Physics Letters*, 26:434-436 (June 1974).
119. Shockley, W. "Currents to Conductors Induced by a Moving Point Charge," *Journal of Applied Physics*, 9:635-636 (October 1938).
120. Smirnov, B.M. *Physics of Weakly Ionized Gases*. Moscow: Mir Publishers, 1981.
121. Smirnov, B.M. *Negative Ions*. New York: McGraw-Hill, Inc, 1982. H.S.W. Massey, Editor.
122. Smirnov, B.M. and M.I. Chibisov. "The Breaking Up of Atomic Particles by an Electric Field and by Electron Collisions," *Soviet Physics JETP*, 22:585-592 (March 1966).
123. Solovev, E.A. "Classical Approximation for the Ionization of a Negative Ion by Electron Impact Near the Threshold," *Soviet Physics JETP*, 45:1089-1092 (June 1977).
124. Stanford Research Systems, Inc, Sunnyvale, California. *Model SR560 Low-Noise Preamplifier*, 1990.
125. Sun Microsystems, Inc, Mountain View, California. *Sun System User's Guide*, 1989.
126. Tang, S.Y., et al. "Negative Ion Formation in Halocarbons by Charge Exchange with Cesium," *Journal of Chemical Physics*, 64:1270-1275 (February 1976).
127. Thorne, L.R. and J.L. Beauchamp. "Efficient Multiphoton Dissociation of CF_3I^+ in the Metastable $X^2E_{1/2}$ Excited State Using CW Infrared Laser Radiation," *Journal of Chemical Physics*, 74:5100-5105 (May 1981).
128. Tisone, G. and L.M. Branscomb. "Detachment of Electrons from H^- by Electron Impact," *Physical Review Letters*, 17:236-238 (August 1966).
129. Tisone, G.C. and L.M. Branscomb. "Detachment of Electrons from H^- and O^- Negative Ions by Electron Impact," *Physical Review*, 170:169-183 (June 1968).
130. Van de Guchte, W.J. and W.J. Van Der Hart. "Excitation of the z-Motion of Ions in Cubic and Elongated Ion Cyclotron Resonance Cells," *International Journal of Mass Spectrometry and Ion Processes*, 95:317-326 (January 1990).
131. Van Der Hart, W.J. and W.J. Van de Guchte. "Excitation of the z-Motion of Ions in a Cubic ICR Cell," *International Journal of Mass Spectrometry and Ion Processes*, 82:17-31 (January 1988).
132. Varian, Vacuum Division, Palo Alto, California. *Variable Leak Valve Model Nos. 951-5100 & 951-5106 Operating Instructions*, 1980.

133. Walter, T.A., et al. "Mass-Spectrometric Study of the Photoionization of C_2F_4 and CF_4 ," *Journal of Chemical Physics*, 51:3531-3536 (October 1969).
134. Walton, D.S., et al. "Structure Observed During Detailed Measurements of Detachment from H^- by Electron Impact," *Journal of Physics B*, 3:L148-L150 (December 1970).
135. Walton, D.S., et al. "A Measurement of Cross Sections for Detachment from H^- by a Method Employing Inclined Ion and Electron Beams," *Journal of Physics B*, 4:1343-1348 (October 1971).
136. Wang, Mingda and Alan G. Marshall. "Laboratory-Frame and Rotating Frame Ion Trajectories in Ion Cyclotron Resonance Mass Spectrometry," *International Journal of Mass Spectrometry and Ion Processes*, 100:323-346 (October 1990).
137. Wang, Tao-Chin Lin and Tom L. Ricca ;and Alan G. Marshall. "Extension of Dynamic Range in Fourier Transform Ion Cyclotron Resonance Mass Spectrometry via Stored Waveform Inverse Fourier Transform Excitation," *Analytical Chemistry*, 58:2935-2938 (December 1986).
138. Wang, Yicheng, et al. "Collisional Electron Detachment and Decomposition Cross Sections for SF_6^- , SF_5^- and F^- on SF_6 and Rare Gas Targets," *Journal of Chemical Physics*, 91:2254-2260 (August 1989).
139. Webster, Christopher R., et al. "Laser Optogalvanic Photodetachment Spectroscopy: A New Technique for Studying Photodetachment Thresholds with Applications to I^- ," *Journal of Chemical Physics*, 78:646-652 (January 1983).
140. Wetzel, Robert C., et al. "Absolute Cross Sections for Electron-Impact Ionization of the Rare-Gas Atoms by the Fast-Neutral-Beam Method," *Physical Review A*, 35:559-577 (January 1987).
141. Wilson, S. *Electron Correlation in Molecules*. Oxford: Clarendon Press, 1984.
142. Wolfram, Steven. *Mathematica Version 1.2 System Guide Upgrades*. Champaign, Illinois: Wolfram Research, Inc, 1990.
143. Zener, Clarence. "Non-Adiabatic Crossing of Energy Levels," *Proceedings of the Royal Society of London*, A137:696-702 (September 1932).

Vita

Captain Kevin B. Riehl was born on 7 July 1958 in Detroit, Michigan. He graduated from Franklin High School in Livonia, Michigan in 1976 and subsequently attended the Massachusetts Institute of Technology on an Air Force Reserve Officer Training Corps scholarship. In June, 1980, he graduated with a Bachelor of Science in Physics and was commissioned into the Air Force. His first assignment was to the Space Physics Division, Air Force Geophysics Laboratory, Hanscom AFB, Massachusetts. There he analyzed data from electron sensors flown on the Defense Meteorological Satellite Program (DMSP) and was the principal investigator for the Proton Telescope, a 1-100 MeV proton sensor now flying on the Combined Release/Radiation Effects Satellite (CRRES). In 1984, he was selected for promotion to Captain and awarded a regular commission. In May, 1985, Capt Riehl attended the School of Engineering, Air Force Institute of Technology (AFIT), Wright-Patterson AFB, Ohio where he was awarded a Master of Science in Engineering Physics in December, 1986. Upon graduation, he was assigned to the Advanced Systems Directorate, HQ Air Force Technical Applications Center, Patrick AFB, Florida. Among other tasks, Capt Riehl was principal investigator or flight sponsor for three experiments flown on the Space Shuttle (flights STS-27, -28, -33). He entered the PhD program at AFIT, Wright-Patterson AFB, Ohio in June, 1989.

Captain Riehl is married to the former Dianne L. Segien, of Waltham, Massachusetts. They have two children, Brian and Jessica, and reside in Beavercreek, Ohio. His follow-on assignment is as Chief, Applied Electromagnetics Section, Aerospace Power Division, Aero Propulsion and Power Directorate, Wright Laboratory, Wright-Patterson AFB, Ohio.

Permanent address: 8307 Donna Road
Westland, Michigan 48185

REPORT DOCUMENTATION PAGE			Form Approved OMB No. 0704-0188	
Public reporting burden for this collection of information is estimated to average 1 hour per response, including the time for reviewing instructions, searching existing data sources, gathering and maintaining the data needed, and completing and reviewing the collection of information. Send comments regarding this burden estimate or any other aspect of this collection of information, including suggestions for reducing this burden, to Washington Headquarters Services, Directorate for Information Operations and Reports, 1215 Jefferson Davis Highway, Suite 1204, Arlington, VA 22202-4302, and to the Office of Management and Budget, Paperwork Reduction Project (0704-0188), Washington, DC 20503.				
1. AGENCY USE ONLY (Leave blank)	2. REPORT DATE December 1992	3. REPORT TYPE AND DATES COVERED Doctoral Dissertation		
4. TITLE AND SUBTITLE Collisional Detachment of Anions Using Fourier Transform Mass Spectrometry		5. FUNDING NUMBERS		
6. AUTHOR(S) Kevin B. Riehl, Captain, USAF				
7. PERFORMING ORGANIZATION NAME(S) AND ADDRESS(ES) Air Force Institute of Technology, WPAFB OH 45433-6583		8. PERFORMING ORGANIZATION REPORT NUMBER AFIT/DS/ENP/92-3		
9. SPONSORING / MONITORING AGENCY NAME(S) AND ADDRESS(ES)		10. SPONSORING / MONITORING AGENCY REPORT NUMBER		
11. SUPPLEMENTARY NOTES				
12a. DISTRIBUTION / AVAILABILITY STATEMENT Approved for public release; distribution unlimited		12b. DISTRIBUTION CODE		
13. ABSTRACT (Maximum 200 words) Fourier Transform Mass Spectrometry (FTMS) is used to make energy resolved ion-neutral reaction measurements at high translational energies (up to several hundred eV). The technique is demonstrated for collisional detachment of anions, and should be easily applied to other inelastic reactions. Collisional detachment cross sections of iodine anions onto gas phase targets of neon, xenon, and trifluoromethyl iodide are measured for 1-300 eV (lab frame). Peak detachment cross sections are roughly 2, 8.5, and 7 square angstroms, respectively. Ion kinetic measurements show the iodine anion is unreactive in trifluoromethyl iodide at thermal energies. Positive ion chemistry is consistent with previous results from well established techniques. However, the influence of internal energy is quantified for the first time by varying the electron energy of ion formation. Changes in the observed reactions of iodine cations and trifluoromethyl iodide cations are attributed to ion formation in excited states. Ionization and attachment cross sections for electron impact on trifluoromethyl iodide are reported for the first time over the energy range 10-50 eV. The ion motion in the FTMS ion trap is modelled and the relationship between the ion trajectory and the ion image current is quantified.				
14. SUBJECT TERMS Trifluoromethyl Iodide (CF ₃ I), Negative ions, Collisional detachment, Attachment, Fourier Transform Mass Spectrometry (FTMS)		15. NUMBER OF PAGES 162		
		16. PRICE CODE		
17. SECURITY CLASSIFICATION OF REPORT Unclassified	18. SECURITY CLASSIFICATION OF THIS PAGE Unclassified	19. SECURITY CLASSIFICATION OF ABSTRACT Unclassified	20. LIMITATION OF ABSTRACT UL	